DESIGN AND FABRICATION OF POLARIZED INGAN LIGHT-EMITTING DIODES AND THZ POLARIZER BASED ON SUBWAVELENGTH METALLIC NANOGRATINGS

ZHANG LIANG
(M.Sc in Physics, Wuhan University)

A THESIS SUBMITTED

FOR THE DEGREE OF DOCTOR OF PHILOSOPHY

IN ADVANCED MATERIALS FOR MICRO-AND NANO-SYSTEMS (AMM&NS)

SINGAPORE-MIT ALLIANCE

NATIONAL UNIVERSITY OF SINGAPORE

2011

ACKNOWLEGMENTS

First of all, I would like to express my sincere appreciation to my supervisors. Prof. Chua Soo Jin and Prof. Eugene A Fitzgerald for their continuous supports, invaluable guidance, and encouragement throughout this research work. They have offered me insightful ideas and suggestions and have led me the scientific way to do research with their profound knowledge and rich research experience. Without their help, I would not be able to achieve this research goal.

I am also extremely grateful to Dr. Teng Jinghua and his team members from Institute of Materials Research and Engineering (IMRE). Dr. Teng is a very accomplished research scientist with experience of many years in the field of solid-state lighting, and I did most of the experiments in IMRE under his supervision.

I am greatly indebted to my senior Dr. Chen Ao, who shared with me his valuable experience in electron beam lithography. He has also given me a lot of helpful suggestions and encouragements during my hard period. I am also grateful to Dr. Tan Chuan Beng, who shared with me his valuable knowledge in photoluminance, p-n junction device physics and hydrothermal growth. I am greatly thankful to my junior Mr. Deng Li Yuan, who has worked with me and provided a lot of assistance to this work.

Finally, I wish to express my sincere appreciations to Prof. C.A. Ross, Prof. C.C. Wong, Prof. C.V. Thompson and Prof. W.K. Choi for sharing their insightful opinions and suggestions with me throughout my PhD life. I am also thankful to the scholarship provided by SMA and to all administrative staffs.

Table of Contents

Summary

Design and fabrication of polarized InGaN light-emitting diodes and THz polarizer based on subwavelength metallic nanogratings

InGaN light emitting diodes are poised to replace conventional light sources for general illumination application due to their higher luminous efficiency and long lifetime. For other applications such as in imaging, liquid crystal backlighting and 3D display, polarized light sources would be highly desirable.

In this work, we designed polarized InGaN LED by integrating sub-wavelength metallic nano-grating (SMNG) fabricated on the emitting surface. The choice of material for visible-wavelength SMNG is discussed, and the physical parameters for SMNG are optimized. The distribution of the electromagnetic field around the grating when light is passing through it was investigated. These studies show a promising design of polarized InGaN LED by using SMNG.

We have developed the process flow to make polarized InGaN LED by integrating SMNG on the emitting surface of InGaN LED. Both device structures and fabrication methods are compatible to conventional InGaN/GaN LED fabrication. The process parameters for photolithography, e-beam lithography, nanoimprint lithography, e-beam evaporation, plasma etching and ion milling are studied and optimized.

Based on above structure design and process development, a linearly polarized surface emitting InGaN/GaN LED on sapphire substrate was demonstrated, with a polarization ratio of 7:1 (~88% polarization of light) for electroluminescence emission from the device under electrical pumping. This value is the highest ever reported among those achieved by other methods such as from LEDs grown on non-polar/semi-polar surface, LEDs with backside reflector or those incorporating photonic crystal.

Our finding suggests an effective way to make polarized light emitting devices, without using special oriented substrate, complex design, fabrication and packaging process. We also investigated the extension of this technology to THz range. The performances of these subwavelength gratings in THz ranges are characterized by THz-TDS and FTIR.

List of Figures

Chapter 1: Introduction

1.1 Background of the project

1.1.1 Historical and state-of-the art light-emitting diode

Perhaps one of the most widely used technologies is the light emitting diode (LED), which is applied in an extremely broad range of markets and applications. LEDs with low output powers are used for indicator lighting on computers, laptops or televisions and also for bright outdoor displays. LEDs with high output powers are used in traffic signals and automotive headlights, projection display and indoor and outdoor illumination. LEDs are also used to backlit buttons or keypads on cellular telephones, and liquid crystal display (LCD) screens. These applications have lead to major growth of LED market in recent years.

LED is basically an electrical diode consisting of an n-type semiconductor and a p-type semiconductor forming a junction. Due to the difference in electron and hole concentration on the two sides of the junction, the diffusion of electrons and holes results in regions with net charge, across which there is an electric field. This electric field induces a drift current of electrons and holes, which exactly offsets diffusion currents at equilibrium, and there is no net current flowing through the diode. When a positive voltage is applied to the p-type side, the electric field and the drift current are reduced, thus the diffusion current overwhelms drift current, making electrons and holes injected into the other side and recombined with each other. Being direct bandgap, the distinguishing feature of an LED is that the recombination is radiative and releases energy in the form of light, usually as one particular color.

LEDs were discovered by accident early in the last century and the first LED results were published in 1907. LEDs became forgotten and only to be re-discovered later in the 1920s and again in the 1950s. In the 1960s, several groups pursued the demonstration of semiconductor lasers. The first applicable LEDs were by-products in this pursuit. During the last 40 years, progress in the field of LEDs has been breathtaking.

The InGaN material system was developed in the early 1990s and has become commercially available in the late 1990s. A name that is closely associated with GaN LEDs and lasers is the Nichia Chemical Industries Corporation, Japan. A team of researchers that included Shuji Nakamura has made lots of contributions to the development of GaN LEDs [1-7].

The bandgap energy versus the lattice constant in the nitride material family is shown in Figure 1. Inspection of the figure indicates that InGaN is suitable for covering the entire visible spectrum. To date InGaN is the primary material system for high-brightness ultraviolet (UV), blue, green and white LEDs.

State-of-the art LEDs are bright, efficient, small, and reliable. In contrast to many other light sources, LEDs have the potential of converting electricity to light with near-unity efficiency. Besides high efficiency and power, a key benefit provided by LEDs is the ability to tune properties such as wavelength or color temperature of emission to meet the needs of specific applications. This flexibility allows the LED to service a wider variety of markets than any other light source. Indeed, they are already widely used in computers, television sets and other consumer electronics, and are becoming a market leader for outdoor applications such as traffic lights and indicator lights on cars. The story of LEDs is still in progress. Great technological advances will surely continue to be made. Philips and other big companies are investing heavily to help LED technology to evolve rapidly. As a result, it is expected that LEDs will play an increasingly important role as light sources and will become the dominant light source in the future.

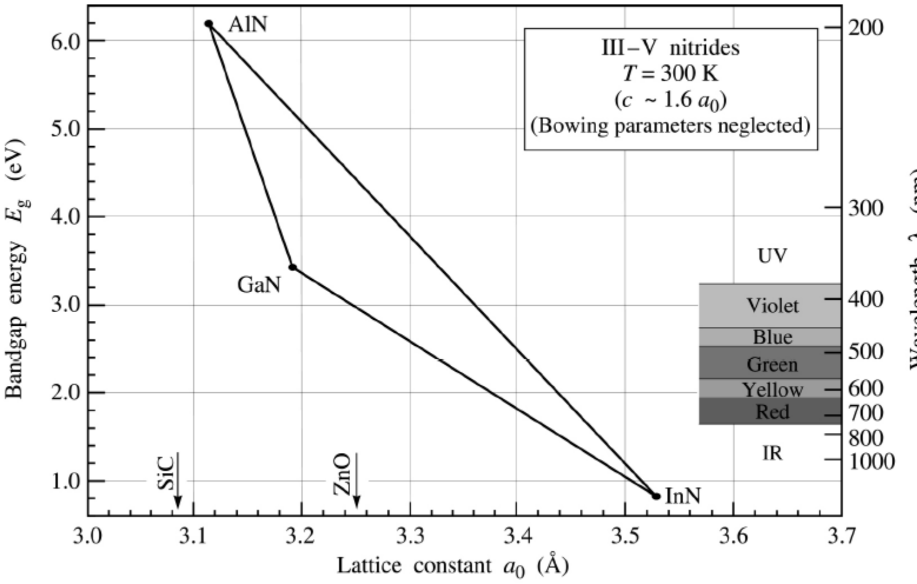

Figure 1-1 Bandgap energy versus lattice constant of III-V nitride semiconductors at room temperature (adopted from [8])

1.1.2 Polarization of light

Polarization is a property which describes the orientation of oscillations for certain types of waves. Electromagnetic waves such as light, exhibits polarization, while acoustic waves in a gas or liquid do not have polarization, since the direction of vibration is same as the direction of propagation.

By convention, the polarization of light is described as the orientation of the wave's electric field. When light is traveling in free space, in most cases it propagates as a transverse wave, where the polarization is perpendicular to the wave's direction of travel. In this case, the electric field may be oriented in a single direction, so called linear polarization; or it may rotate during travelling, so called circular or elliptical polarization. The description of the wave's polarization can be complex for instance in a waveguide or the radically polarized beams in free space, as the fields can have longitudinal as well as transverse components [9].

The polarization state of light is one important property. Natural processes including magnetic fields, mechanical stresses, and chemical reactions can affected the polarization of light. Measuring the change of polarization can give valuable information about these processes. Polarized light can have many commercial applications, ranging from simple devices such as polarized sunglasses to complicated liquid-crystal displays (LCDs). It can also be used in theaters to project 3-D movies.

1.1.3 Polarization elements

Natural light is unpolarized by having its electric field symmetrically orientated. All polarization elements work because of certain form of asymmetry. This asymmetry gives rise to the different polarized waves. Different processes can be used to polarize light, including dichroism, reflection, birefringence, and scattering. Dichroism refers to the selective absorption of one polarizations. Light reflected at the Brewster's angle is completely polarized parallel to the plane of surface. Brewster's angle θ_B is defined by $\tan\theta_B = n_t / n_i$, where n_t is the index of the transmitted medium and n_i is the index of the incident medium. Birefringence is a property of certain crystalline materials, such as calcite, where different polarizations see different indices of refraction in the material. This will cause the two polarizations to travel different paths through the material, e.g. Wollaston polarizing prisms. Finally, scattering from a molecule can also polarize light because of the dipole field created by the excited molecule.

One type of birefringent polarizer is the wire-grid polarizer [9] where the asymmetry is due to the wires. The earliest documented wire-gird polarizer was produced by Heinrich Hertz in 1888 when he used it to test the properties of the newly discovered radio wave. Since then, the grating period of wire-grid polarizer has been scaled down, and successfully applied to the microwave and infrared regions, and more recently used as polarized beam splitter in optical communication.

1.1.4 Polarization of various light sources

Most of the electromagnetic radiation sources contain a large number of atoms or molecules that emit light. The orientation of the electric fields produced by these emitters may not be correlated, thus light is unpolarized.

In many cases, the output of a laser is polarized, where the electric field oscillates in a certain direction perpendicular to the propagation direction of the laser beam. Gas lasers typically use a window tilted at Brewster's angle to allow the beam to leave the laser tube. Since the window reflects some *s*-polarized light but no *p*-polarized light, the gain for the *s*-polarization is reduced but that for the *p*-polarization is not affected. This causes the laser's output to be *p*-polarized [9]. Some laser light is more polarized than gas lasers, e.g. Nd:YAGs are highly linearly polarized. Diode lasers are much less and may even be elliptically polarized. VCSELs can have very non-classical states, like radial and tangential polarization.

As a part of the development of solid-state lighting technology, the polarization of light emitted from LED has also been studied for long a time. Nonpolar m-plane $(10\underline{1}0)$ GaN film growth was demonstrated on m-plane SiC substrates in 1996 by Horino et al [10–12]. Although the predominant aim of this study was wafer cleaving for laser cavity fabrication since the conventional c-plane sapphire wafers do not cleave, in-plane anisotropic photoluminescence (PL) was demonstrated. At about the same time, from the theoretical aspect, the electronic band structure of GaN was studied. The effective-mass Hamiltonian for wurtzite semiconductors was derived, including the strain effects, which provides a theoretical groundwork for calculating the electronic band structures and optical constants of bulk and quantum-well wurtzite semiconductors [13]. The effect of uniaxial stress on photoluminescence in GaN and stimulated emission in InGaN/GaN multiple quantum wells was also studied [14]. Furthermore, optical gains in wurtzite–GaN strained quantum-well (QW) lasers were theoretically estimated for various crystallographic directions [15, 16]. For the experimental aspects, the optical anisotropy of excitons in strained GaN epilayers grown along the <1010> direction [17] and polarized photoluminescence study of free and bound excitons in free-standing GaN [18] were investigated. In 2000, the advantage of the nonpolar planes was shown by the quantum well structure [19], which demonstrated that the epitaxial growth of GaN/(Al,Ga)N in a non-polar direction allows the fabrication of structures free of electrostatic fields, resulting in an improved quantum efficiency. Later, optical polarization characteristics were studied on such quantum wells via photoluminescence [20-22], which showed a strong in-plane optical anisotropy. Several reports on hetero-epitaxially grown nonpolar LEDs appeared in the year 2003 to 2004 [23–25]. In 2005, Gardner et al. reported electroluminescence (EL) anisotropy on their m-plane LEDs fabricated on m-plane SiC substrates [26]. UCSB nitride group followed by reporting on semipolar LEDs [27–29]. Despite this interesting polarized light emission property, research stagnated because of inferior material quality and low optical output power. Moreover, even though GaN-based LEDs grown on non-polar or semi-polar crystal planes emit some polarized light, growth in these directions is challenging, and very high quality bulk GaN substrates have to be used to achieve acceptable light output intensity. These substrates are typically very small and expensive, which makes the commercial application of non-polar or semi-polar growth currently unfeasible. Instead, commercial efforts are focused on conventional polar c-plane LEDs, which have generally been assumed to be unpolarized.

1.2 Motivation and objectives

Since early this year, the movie “Avatar” has attracted a lot of interest on 3D movie and 3D display. Creating the illusion of 3 dimensions relies entirely on the fact that we have two eyes separated by a particular distance. If each eye is shown the same image shot from slightly different angles then when our brain combines the images, the resulting image will appear 3D. This is the principle that all 3D effects use. In 3D movies and pictures, there are two images, one for each eye. The positions of objects in the images are more or slightly different depending on how deep they are in the picture. These difference forces the eyes to change their angle to merge the two images. In most 3D movie theaters, the two images are projected onto the screen by light waves whose polarizations are altered by a polarized filter. The glasses the viewer wears have differently polarized lenses, which allow incoming light to pass if light polarized in same direction as the lens, and filter it completely if it is polarized with a 90 degree angle difference. This allows only the correct image to be seen by each eye of the viewer. While it works fine in 3D theater, is it possible that we watch 3D movie at home simply with our laptop? Since there is no way to similarly create two polarized images by projecting through polarized filter, we need the light source which powers laptop screen to be polarized, namely a polarized visible LED.

In addition to this simple example, polarized light emission attracts attention for general display applications as well [30-34]. It is considered to be a great advantage in using LEDs as liquid crystal display (LCD) backlighting in computer monitors and mobile phone screens, since the operation principle of LCDs inherently relies on linearly polarized light. Besides to be extremely useful for LCD backlighting, LEDs that emit polarized light would be highly desirable for many applications, including sensing, imaging [35,36], and communication [37] based on optical polarization-multiplexing.

Thus, the non-polar or semi-polar InGaN growth has been aggressively pursued since such growth for LED structures leads to partially polarized output. Comparatively little attention has been paid to the emission characteristics by state-of-the-art LEDs grown on polar substrates, which is actually the most commonly used in the market due to their high efficiency, power and long lifetime. It has been reported that light emitted in certain directions shows some degree of polarization [38]. Although valence band intermixing can result a dominant polarization along quantum well plane, it only emits from the edge of unpackaged LED chips [39], and hence with limited application. Moreover, this inherent polarization effect is eliminated by rotationally symmetric structures of LED packaging because their act to average the light rays emitted in different directions. More recently, the viability of the polarized light source concept based on conventional c-plane GaN-based LEDs has been proven following the demonstration of polarized light emission by c-plane LEDs and the polarization enhancing reflector and encapsulation concept [40-42]. The basic idea of this design takes advantage of the low reflection coefficient for transverse magnetic polarized light near Brewster's angle, so as to enhance extraction of a particular desired linear polarization from an unpolarized source. However, it is clear that when the concept behind the polarization-enhancing encapsulation is applied to real-world sources such as LEDs – which may have different emission patterns –the optimum shape may be different. The largest enhancement of polarization is achieved only when the encapsulation shape is matched specifically to the emission pattern of the encapsulated light source. As a result, complex design, fabrication and packaging process are involved, and the resulting polarization ratio is only up to 3.5 : 1. High polarization ratios light emitting sources will be a requirement if replacement of the polarizing films in conventional LCDs is to be achieved. Moreover, the space occupied by the reflector as designed in [40] also adds additional limit on the application of such polarized light emitter. Miniaturization and refinement to make this device that is similar in size to currently commercial LED is a major challenge of this technology.

Despite these problems, companies still expressed great interest for the polarized LEDs, which gives great motivation to continue this research. Faced with the difficulty of a bottom reflector approach, we are forced to work on the surface. The easiest approach is to directly place conventional polarization elements onto the LED. Unfortunately, conventional high quality polarizer such as birefringent crystal has similar problem as the above-mentioned reflector due to its large dimension, e.g the Wollaston polarizing prisms. It is hardly possible to place a thin film of birefringent crystal on the LED surface with a size to matching to the die while leaving two electrodes uncovered for external connection.

Another idea is the integration of a wire-grid polarizer on the LED surface. Since the key element of wire-grid polarizer is the metallic grating whose dimension is scalable, the concept is theoretically applicable to LED in the visible regime. Moreover, compared with the other polarization elements, a noticeable advantage of wire-grid polarizers is that their fabrication process is compatible with that of solid-state diodes, which makes it possible to integrate them for solid-state lighting. Finally, the polarization properties can be tailored for specific applications by changing the physical parameters of the gratings, which is a feature not available with other types of polarization elements. And it is thought that this tight integration may give rise to high polarization ratios. Hence, we are motivated to investigate the development of metallic grating integrated on InGaN LED for polarized emission

1.3 Organization of thesis

The subject of this thesis is to develop polarized LED by integrating subwavelength metallic nanograting to InGaN LED. Meanwhile, the polarization response of the subwavelength metallic grating extended to the terahertz wave is also studied.

In Chapter 2, the theory and basic optical properties of subwavelength metallic grating will be presented. Numerical schemes for the simulation used in this thesis will be briefly introduced.

In Chapter 3, the main experimental tools used in this project will be introduced, including photolithography, e-beam lithography, nanoimprint lithography, plasma etching, atomic force microscopy, Fourier transform infrared spectroscopy and terahertz time-domain spectroscopy.

In Chapter 4, simulations are performed to model the performance of subwavelength grating. The choice of grating material for application in the visible-wavelength range and how the changes in the physical parameters of the grating affect its polarization properties are studied in details.

In Chapter 5, the process flow for fabricating the polarized LED is discussed in details. The fabricated device is electrically pumped and characterized, where the EL emission shows a high degree of polarization.

In Chapter 6, the polarization response of the subwavelength metallic grating extended to the terahertz wave is studied by simulation. The fabrication and characterization of the gratings are presented. Results show that subwavelength gratings are also applicable for polarizing THz waves.

The whole thesis will be summarized in Chapter 7.

Chapter 2: Theory and Modeling Method

2.1 Introduction

The propagation of light within a bulk material is characterized by its refractive index that averages over the atomic structure of the medium. When an object has its structure comparable or larger than the wavelength of light, its influence on the light propagation is described by the laws of reflection, refraction and diffraction. Between these two extremes there is a region where the structure is too fine to give diffraction but is too coarse for the medium to be considered as homogeneous. Such a structure is called a subwavelength structure, which is the key element of this thesis. In this chapter we will first briefly introduce subwavelength structure and the effective medium theory (EMT), on which theory the principle of subwavelength grating will be based. Due to the nature of a subwavelength structure, a full description can only be achieved through a rigorous solution of Maxwell's electromagnetic equations. We will briefly describe two rigorous numerical methods used for simulations performed in this thesis, namely for the frequency domain method: Rigorous Coupled-Cave Analysis (RCWA), and for the time domain method: Finite Difference Time-Domain (FDTD) analysis.

2.2 Subwavelength structure

The physics of reflection, refraction and diffraction and basic principles of optical design have been well understood for a long time， which has enabled the successful development of optical science and technology. However, the optical technology has been limited by a very reasonable constraint that optical systems could only be designed with materials that are actually available. Consider a simple task of designing an anti-reflection coating to work at one single wavelength at normal incidence. Theoretically, a single layer will generate two reflected waves, one from the air/layer interface and one from the layer/substrate interface. If the optical thickness of the layer is such that the two reflected waves are exactly out of phase, and that the layer has a refractive index equal to the square root of that of the substrate, the two reflections will cancel exactly since they have the same amplitude. So a single layer could ideally behave as a perfect anti-reflection coating. Unfortunately most common optical glasses have a refractive index around 1.55, so the anti-reflection layer needs to have a refractive index of 1.245. Such a material does not exist in nature and more complex solutions are required.

Consider, however, what will happen if we introduce into a standard bulk material a very fine structure, e.g., a series of holes. When the scale of the structure is substantially smaller than the wavelength of light, it will not be resolved by the light thus the light will “see” a composite material that has its optical properties between air and the base material. Therefore it is possible to control the effective index of refraction by varying the fraction of material that is removed. This could extend the range of materials that are available for optical design.

When the wavelength of light is very much greater than the dimensions of the structure it is possible to consider the material as homogeneous and having an appropriate effective value of refractive index. On the other hand, when the dimensions of the structure are comparable to or larger than the wavelength of light the optical properties are dominated by diffraction. Between these two extremes is a region where the dimensions are sufficiently small that no diffracted orders could propagate, but it is not possible to apply simple approximations of a homogeneous medium. This is so called “subwavelength domain”, where homogenization technique does not strictly apply but can give a good physical understanding of the medium properties. Recent developments in micro and nano lithography and associated technologies make it possible to apply these principles to practice and in particular to produce “artificial media” which works in the subwavelength domain. As a result, the subject of subwavelength optical elements now attracts a great deal of research interest.

2.3 Effective medium theory

Rigorous solution of Maxwell's electromagnetic equations can be applied to give a full description of subwavelength structure. However, the numerical nature of rigorous solution makes it difficult to get an intuitive feel for underline physics. It is preferred to start with an approximate theory to gain insight into the subwavelength gratings, therefore we have used an effective medium theory (EMT). EMT treats heterogeneous media as a new medium with some effective permittivity, which is based on the permittivity of the constituent materials and their relative volumes [1]. EMT requires that the wavelength of the incident light be larger than the size scale of the individual media, namely the wavelength must be longer than the period of the grating. Under such condition, different mediums cannot be distinguished by the incident wavelength and their physical properties are averaged over.

As shown by Yeh and Rytov [2-4], the effective index of refraction depends on the polarization of the incident light, either transverse-magnetic (TM) polarization, which has the electric field perpendicular to the grating, or transverse-electric (TE) polarization, which has the electric field parallel to the grating, with the simplest forms for the effective index as follows:

$$n_{TE}^2 = (1-d)n_i^2 + dn_m^2 \tag{2.1}$$

$$\frac{1}{n_{TM}^2} = \frac{1-d}{n_i^2} + \frac{d}{n_m^2} \tag{2.2}$$

where d is the duty cycle (the fill factor of the material inside incident medium), n_i and n_m are the refractive indices of the incident medium and the material of the subwavelength structure, respectively. Consider an example of 1D dielectric grating in air at 1550nm wavelength with a 50% duty cycle. Then n_i = 1.0 and n_m =1.5 according to the handbook of optical constant [5]. Solving for the effective TE and TM indices gives 1.275 and 1.17, respectively. The general behavior of subwavelength gratings is demonstrated by above results, where the effective index of the grating is different for TE and TM incident light. It means even though the subwavelength structure cannot be "seen" by the incident light whose wavelength is much larger than the structure dimension, the two polarizations of incident light still travel at different speeds inside the material. This is exactly an asymmetry behavior resulting from the 1D nature of the grating. Such asymmetry gives birefringence similar to conventional birefringent crystal in which different indices of refraction are seen by different polarizations in the material. The two different indices could be used to generate a phase retardation on the two polarization components when light travels through the material, thus altering the polarzation nature of the light. In such a way, an artificial polarization element is created, by using subwavelength grating. That is the idea of using subwavelength structure for polarization control in this thesis.

Compared with convention polarization elements, the subwavelength structure could be made with much more tiny size, and be easily integrated on modern optical devices. Moreover, polarization properties can be tailored for specific applications by changing the physical parameters of the gratings, which is a feature not available with other types of polarization elements.

Depending on the ratio of the period to the wavelength, there are different orders of EMT, with the higher orders being more accurate. The equations given above are of zeroth order, which is exactly accurate when the period is close to zero. EMT averages over the properties of the different materials by making the assumption that the electromagnetic field is fairly constant over one period. A validity condition for this assumption was determined to be [2]

$$\frac{2\pi}{\lambda} p \left| n_{eff} \right| << 1 \tag{2.3}$$

where p is the period, λ is the wavelength of the light, and n_{eff} is the effective index of the material.

2.4 Subwavelength metallic grating

The earliest device to exploit the polarization effect of subwavelength metallic grating was probably made by Hertz to test the properties of the newly discovered radio wave in 1888 [6]. Hertz used a frame of stretched copper wires to show that the waves were unaffected when they passed through the device with polarization perpendicular to the wires, but were stopped completely if the polarization was parallel to the wires. In 1956, Pursley showed that wire gratings could work in the infrared by scaling down the grid parameters linearly with wavelength [7]. In 1964 Bird and Parrish fabricated wire grids by obliquely evaporating metal on plastic diffraction grating replicas [8]. In 1967, Auton used photolithographic processes to fabricate wire-grid polarizers with periods of 4 to 10 microns. In 1978, Yeh introduced EMT model for wire-gird polarizer [3]. Yeh showed that the grating could be modeled as a uniaxial birefringent medium by assuming a period much smaller than the wavelength. He also found expressions for the indices of refraction for each incident polarization. As an example, consider the case of aluminum wire in air with an incident wave of 500nm wavelength with a 50% duty cycle of any grating period. Then $n_i = 1.0$ and $n_m = 0.719 - 6.080i$ according to the handbook of optical constant [5]. Solving for the effective TE and TM indices through (2-1) and (2-2) gives 0.515 –4.242i and 1.433 – 0.004i, respectively. The general behavior of subwavelength metallic gratings is demonstrated by above result, which shows that the grating region behaves as if it was a metallic material for TE light therefore TE light is largely reflected and attenuated. The grating region behaves as a weakly absorbing dielectric material for TM light, therefore it is primarily transmitted. Compared with the dielectric grating discussed in the last section, the birefringence effect is greatly enhanced by the present of metal structures.

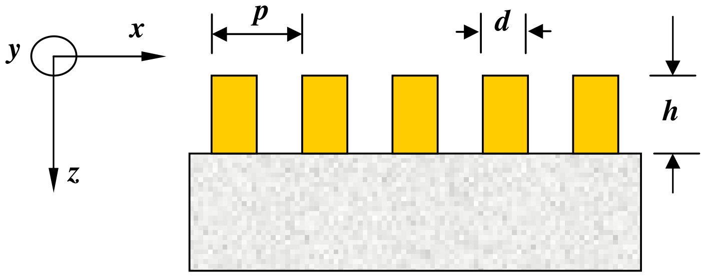

Figure 2-1 Subwavelength metallic grating geometry. The grating is periodic along the x-axis and infinite along the y-axis.

The physical parameters of a subwavelength metallic grating are illustrated in Figure 2-1. The grating is periodic along the x-axis and uniform along the y-axis. Using recent development of micro and nano lithography and associated technologies, the grating could be scaled down with the period p around 100nm, which is called subwavelength metallic nanograting (SMNG) in this thesis. For TE polarized light, the electric field is parallel to the wires along the y-axis as shown in Figure 2-2. Along this direction the electric field drives the electrons along the length of the wires. According to Drude model, the electrons collide with atoms in the metal lattice and attenuate the TE signal. These moving electrons will radiate in both the forward and backward directions, where the forward radiation is out of phase with the incident wave and reduces the transmission, while the backward radiation gives reflection. For TM polarization, the electric field is perpendicular to the wires in the x-z plane as shown in Figure 2-2. In this direction the electrons do not have space to move as far, which reduces both the attenuation and the radiation, thus enables the TM signal to pass through the wires with little change.

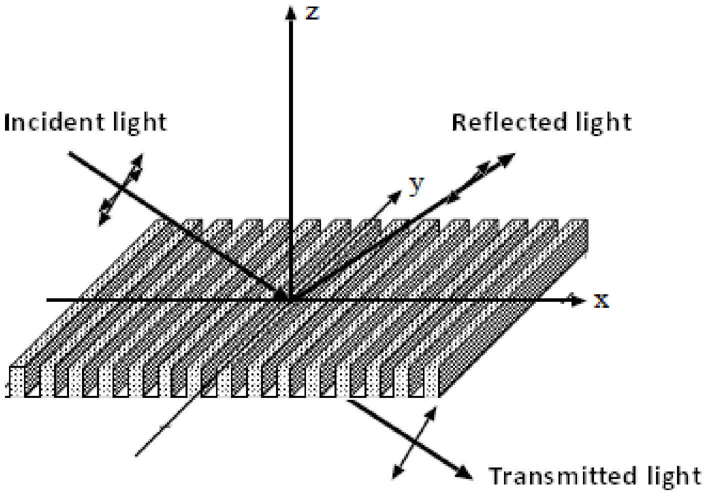

Figure 2-2 General behavior of SMNG. The reflected light is primarily TE polarized, while the transmitted light is primarily TM polarized.

When light is incident in the x-z plane as shown in figure 2-2, the TE and TM polarizations are well defined and completely separated from each other. This is called in-plane incidence. When light is incident outside the x-z plane, so called out-of-plane incidence, it is difficult to describe the behavior since TE and TM light are not well defined and the two orthogonal polarization states become coupled in the grating. The behavior of the grating stays the same in that the transmitted light in linearly polarized, but the modeling becomes more difficult. Previous calculation has shown that out-of-plane incidence results are quite close to that of in-plane incidence for a sufficiently large range of conical incident angles [9]. For this reason, in-plane incidence is used throughout this thesis.

The transmission coefficient of the polarizer is defined as the percent of the desired polarization that transmits through the polarizer. For a subwavelength metallic grating, the desired polarization in transmission is the TM polarization, which has the electric field perpendicular to the wires. The transmission coefficient is then equals to the transmissivity of TM polarization. The extinction ratio is defined using the transmission of the desired polarization divided by the transmission of the undesired polarization, shown as follows,

$$\text{Transmission coefficient} = T_{TM}$$

$$\text{Extinction ratio} = 10\times\log(T_{TM}/T_{TE}) \qquad (2.4)$$

This ratio can range from less than one to over 40 depending on the elements and wavelengths involved. The transmission coefficient is a measure of the efficiency while the extinction ratio is a measure of the contrast.

2.5 Numerical modeling method

Modeling is a complementary tool to design specific optical functions and predict the optical properties of the nanostructures. It involves solving Maxwell equations numerically, combined with the boundary conditions as shown in Eq.2.5. While EMT can give a qualitative idea of what happens in a subwavelength metallic grating, more accurate model for quantitative analysis is also needed. Two main methods are used to solve these equations, via frequency domain method and time domain method.

$$\begin{aligned} &\nabla \times \vec{E} = -\frac{\partial \vec{B}}{\partial t} \\ &\nabla \times \vec{H} = \frac{\partial \vec{D}}{\partial t} + J \\ &\nabla \cdot \vec{D} = \rho \qquad \vec{D} = \varepsilon \vec{E} \\ &\nabla \cdot \vec{B} = 0 \qquad \vec{B} = \mu \vec{H} \end{aligned} \tag{2.5}$$

The basic idea of frequency domain method is to directly obtain solution for each frequency, as shown in Eq.2.6, which involves a process for solving the eigenmodes. Examples are Plane wave expansion (PWE), Rigorous Coupled Wave Analysis (RCWA) and Finite Element Method (FEM).

$$\begin{aligned} &\nabla \times \vec{E} = -\frac{\partial \vec{B}}{\partial t} \\ &\nabla \times \vec{H} = \frac{\partial \vec{D}}{\partial t} \end{aligned} \quad \Longrightarrow \quad \nabla \times [\frac{1}{\varepsilon(r)} \nabla \times \vec{H}(r)] = (\frac{\omega}{c})^2 \vec{H}(r) \tag{2.6}$$

The Basic idea of time domain method is more straight-forward, directly discretize the Maxwell equation in time domain, as shown in Equ.2.3.

$$\begin{aligned} \vec{E}(r,t) &= \vec{E}(r)e^{-j\omega t} \\ \vec{H}(r,t) &= \vec{H}(r)e^{-j\omega t} \end{aligned} \quad \Longrightarrow \quad \frac{\partial \vec{D}}{\partial t} = \frac{\vec{D}(t+\Delta t)-\vec{D}(t)}{\Delta t}$$

(2.7)

2.5.1 Rigorous coupled-wave analysis (RCWA)

Rigorous coupled-wave analysis (RCWA) is widely used to study the optical behavior of grating surfaces. M. G. Moharam and T. K. Gaylord presented a RCWA that was easily adaptable to computer implementation in 1981 [10], which covered planar dielectric gratings with TE polarization. Later papers extended the theory to include TM polarization [11], dielectric surface relief gratings [12] and metallic surface relief gratings [13]. The stability and efficiency of RCWA [14-19] have also been improved. We have used RCWA integrated in software Rsoft for this work [20].

RCWA is an exact formulation of Maxwell's equations. For simplicity in the analysis presented, we consider the incident plane wave with TM polarization (Magnetic field vector perpendicular to the plane of incidence. In this case it is also parallel to the grating wires). The TE polarization could be derived similarly.

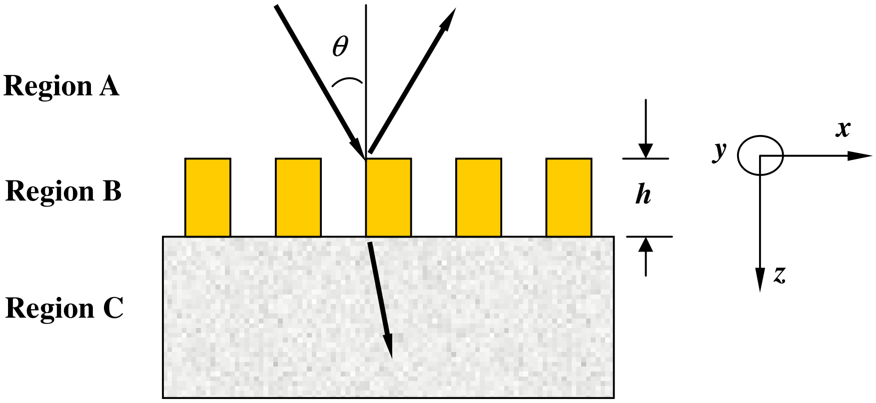

Figure 2-3 RCWA geometry for the SMNG analyzed.

General RCWA geometry for SMNG diffraction problem treated in this thesis is shown in Figure 2-3, where gratings with a rectangular profile are considered and an electromagnetic wave, obliquely incident upon the grating, produces both forward-diffracted and backward-diffracted waves. The electromagnetic field is broken into three regions. Region A and region C are the cover and substrate mediums, being homogeneous dielectric with indices of refraction of n_c and n_s, respectively. Region B is the grating region, which consists of a periodic distribution of both dielectric and metal. The index modulation is expressed as the Fourier series

$$n_g^2(x,z) = n_g^2(x+\Lambda,z) = \sum_p^N \tilde{n}_p(z)\exp(ipKx) \tag{2.8}$$

where Λ is the grating period, $i = (-1)^{1/2}$, $K = 2\pi/\Lambda$ is the magnitude of grating vector and N is the number of diffracted orders retained in the calculation. $\tilde{n}_p(z)$ is the Fourier component of the grating index. In the equations that follow, the subscripts g, c, and s are to denote grating, cover and substrate.

For TM case, the magnetic field in region A is along the y-direction and is written as

$$H_{cy} = \exp[-ik_0 n_c(\sin\theta\cdot x + \cos\theta\cdot z)] + \sum_m r_m \exp[-i(k_{xm}x - k_{czm}z)] \tag{2.9}$$

where $k_0 = 2\pi/\lambda_0$ is the wave vector in vacuum. θ is the angle of incidence, as shown in Figure 2-3. R_m and T_m are the *m*th-order reflection and transmission amplitude coefficients. Similarly, the magnetic field in region C is also along the y-direction and is written as

$$H_{sy} = \sum_m t_m \exp\{-i[k_{xm}x + k_{szm}(z-h)]\} \tag{2.10}$$

In the grating region, the tangential fields can be expressed as Fourier expansions

$$H_{gy} = \sum_m U_{ym}(z)\exp[-ik_{xm}x] \tag{2.11}$$

Substituting (2.11) into Maxwell's equations, the reflection and transmission coefficients are then found by matching the tangential field components at the z = 0 and z = h boundaries [13]. The final transmission and reflection efficiencies are then given by

$$R_m = r_m r_m^* \operatorname{Re}\left(\frac{k_{czm}}{k_0 n_c \cos\theta}\right)$$

$$T_m = t_m t_m^* \operatorname{Re}\left(\frac{n_c k_{czm}}{k_0 n_s^2 \cos\theta}\right) \tag{2.12}$$

Similarly, for TE polarization where the electrical field vector is along the y direction, the electric fields in the cover and substrate regions are given by

$$E_{cy} = \exp[-ik_0 n_c(\sin\theta\cdot x + \cos\theta\cdot z)] + \sum_m r_m \exp[-i(k_{xm}x - k_{czm}z)] \tag{2.13}$$

$$E_{sy} = \sum_m t_m \exp\{-i[k_{xm}x + k_{szm}(z-h)]\} \tag{2.14}$$

In the grating region, tangential fields are given by

$$E_{gy} = \sum_m S_{ym}(z)\exp[-ik_{xm}x] \tag{2.15}$$

By applying the boundary conditions at z = 0 and z = h in a similar way, the finally TE wave reflection and transmission efficiencies are given by

$$R_m = r_m r_m^* \operatorname{Re}\left(\frac{k_{czm}}{k_0 n_c \cos\theta} \right)$$

$$T_m = t_m t_m^* \operatorname{Re}\left(\frac{k_{czm}}{k_0 n_c \cos\theta} \right) \tag{2.16}$$

The coefficients in the above equations are solved numerically during our simulation. For each run of simulation, we need to specify the index of refraction of the three regions, grating period, grating height, duty cycle, and the angle of incidence. Then the transmission and reflection efficiency could be solved for both TE and TM polarization, respectively.

2.5.2 Finite difference time-domain (FDTD)

While RCWA is good to show the frequency response of subwavelength grating and to optimize the grating parameters, we would also like to have an insight into the physical process when light passes through the subwavelength structure. Finite Difference Time-Domain (FDTD) is a popular numerical method, because of its relatively ease of implementation, and applicability to arbitrary structures [21]. The principle is well known and straightforward. Consider a region of space in which light is travelling, Maxwell's curl equations can be written in Cartesian coordinates as six simple scalar equations. Two examples are:

$$\frac{\partial H_x}{\partial t} = \frac{1}{\mu}\left(\frac{\partial E_z}{\partial y} - \frac{\partial E_y}{\partial z}\right)$$

$$\frac{\partial E_x}{\partial t} = -\frac{1}{\varepsilon}\left(\frac{\partial H_z}{\partial y} - \frac{\partial H_y}{\partial z}\right) \qquad (2.17)$$

The other four are symmetric equivalents of (2.17) and are obtained by cyclically exchanging the x, y, and z subscripts and derivatives. Maxwell's equations describe a situation in which the temporal change in the **E** field is dependent upon the spatial variation of the **H** filed, and vice versa. The FDTD method solves Maxwell's equations by first discretizing the equations via central differences in time and space and then numerically solving these equations [20].

The most common method to solve these equations is based on Yee's mesh [22] and computes the **E** and **H** field components at points on a grid with grid points spaced Δx, Δy, and Δz apart. The **E** and the **H** field components are then interlaced in all three spatial dimensions as shown in Fig. 2-4. Furthermore, time is broken up into discrete steps of Δt. The **E** field components are then computed at times $t = n\,\Delta t$ and the **H** fields at times $t = (n+1/2)\,\Delta t$, where n is an integer representing the step count. For example, the **E** field at a time t = n Δt is equal to the **E** field at t = (n-1) Δt plus an additional term, Δ**E**, computed from the spatial variation, or curl, of the **H** field at time t.

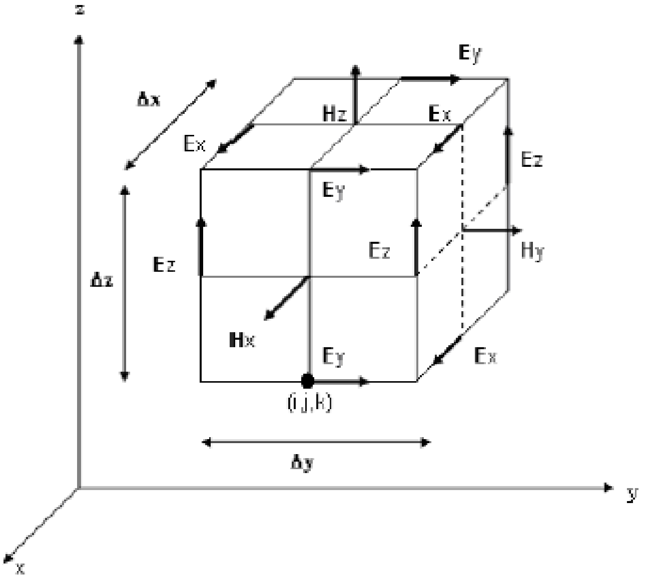

Figure 2-4 In a Yee cell of dimension Δx, Δy, Δz, note how the H field is computed at points shifted one-half grid spacing from the E field grid points [22].

This method results in six equations that can be used to compute the field at a given mesh point, denoted by integers *i*, *j*, *k*. For example, two of the six are:

$$H^{n+1/2}_{x(i,j,k)} = H^{n-1/2}_{x(i,j,k)} + \frac{\Delta t}{\mu \Delta z}\left(E^{n}_{y(i,j,k)} - E^{n}_{y(i,j,k-1)}\right) - \frac{\Delta t}{\mu \Delta y}\left(E^{n}_{z(i,j,k)} - E^{n}_{z(i,j-1,k)}\right)$$

$$E^{n+1}_{x(i,j,k)} = E^{n}_{x(i,j,k)} + \frac{\Delta t}{\varepsilon \Delta y}\left(H^{n+1/2}_{z(i,j+1,k)} - H^{n+1/2}_{z(i,j,k)}\right) - \frac{\Delta t}{\varepsilon \Delta z}\left(H^{n+1/2}_{y(i,j,k+1)} - H^{n+1/2}_{y(i,j,k)}\right) \quad (2.21)$$

These equations are iteratively solved in a leapfrog manner, alternating between computing the **E** and **H** fields at subsequent $\Delta t/2$ intervals [20].

Using this leapfrog manner, each field component in anywhere and at any time point could be calculated based on the field of the previous time step itself and the surrounding component. Thus the field distribution at any time point could be shown. A dramatic picture of how light flows through the material with any structure could be viewed by FDTD as well. In this thesis, we will use the FDTD in software [20, 23] to simulate the physical process of light transmission through subwavelength grating. Basically, to initiate a FDTD simulation, we need to specify the map of distribution for the index of refraction of the whole simulation regions, locate the light source and specify its frequency. Then the field distribution of the whole simulation region at any time point could be calculated.

Besides above obvious advantage of simplicity, FDTD is a time consuming method due to the iterative calculation process. FDTD is also limited in the application for non-dispersive materials, such as the case of calculating transmission spectrum of metallic grating in visible wavelength for this work, because the dispersion model is in spectrum domain. RCWA is a good frequency domain method to solve this problem.

2.6 Summary

For subwavelength structures, a first order approximation on the effect of TE and TM wave propagation can be obtained using EMT. For a grating this first order approximation is accurate when the period satisfies the condition (2.3). For more detailed computations, Maxwell's equations have to be solved numerically using either the RCWA or FDTD method.

Chapter 3: Fabrication and Characterization Tools

3.1 Introduction

In this chapter, an introduction is given to the main experimental tools, for both fabrication and characterization, used throughout this project. The working principle of the tools, instrumentation, primary parameters, and specific application in this project are presented in detail.

3.2 Process tools

3.2.1 Photolithography

Photolithography is the process of transferring geometric patterns on a mask to a thin layer of photo-sensitive material (e.g. photoresist) covering the surface of a semiconductor wafer. Figure 3-1 shows the schematic diagram of photolithography used in this work using positive and negative resist. The wafer is initially heated to a temperature sufficient to drive off any moisture that may be present on the wafer surface. A liquid or gaseous "adhesion promoter", such as hexamethyldisilazane (HMDS), is applied to promote adhesion of the photoresist to the wafer. This layer prevents the aqueous developer from penetrating between the photoresist layer and the wafer surface, thus preventing so-called lifting of small photoresist structures in the developing pattern.

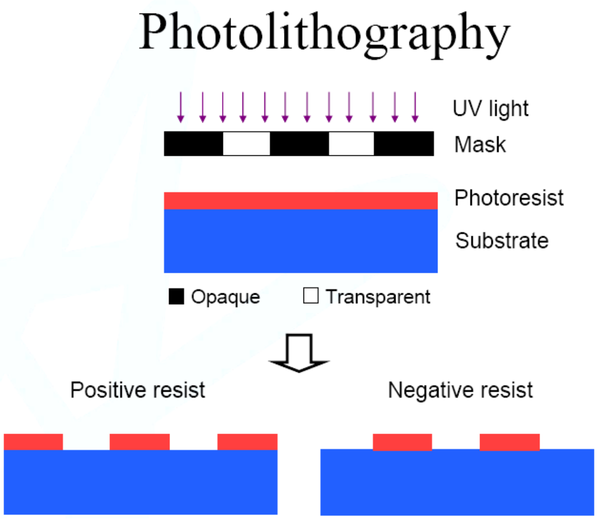

Figure 3-1 Schematic diagram of photolithography

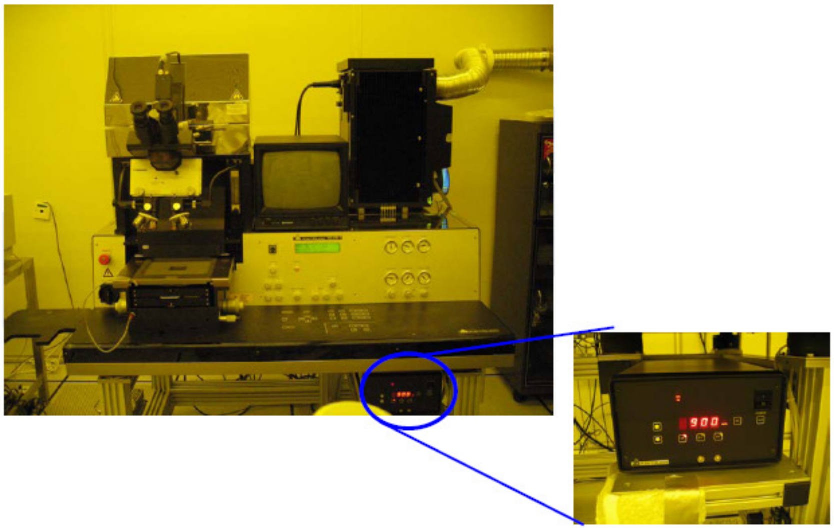

Figure 3-2 SUSS Mask Aligner MA8 in IMRE

The equipment used in this work is the KARL-SUSS Mask Aligner MA8 (Figure 3-2) available in IMRE, which uses an ultraviolet light source from a gas-discharge lamp using mercury. These lamps produce light across a broad spectrum with several strong peaks in the ultraviolet range. This spectrum is filtered to select a single spectral line, the so called "i-line" (365 nm). The minimum feature size for reliable pattern transfer and reproduction is 1um. It allows the alignment of masks sequence, which is important for LED processing in this work.

Figure 3-3 shows the basic recipe for photolithography used in this work. After cleaning and dehydration bake, the wafer is covered with photo resist by spin coating. A viscous, liquid solution of photo resist is dispensed onto the wafer. In this work, the spin coating is applied with the wafer spun at 1200 to 4800 rpm for 30 to 60 seconds, and produces a layer between 6.5 and 1.2 um thick according to our requirement. The spin coating process results in a uniform thin layer, with uniformity of within 5 to 10 nanometres. This uniformity can be explained by detailed fluid-mechanical modelling, which shows that essentially the resist moves much faster at the top of the layer than at the bottom, where viscous forces bind the resist to the wafer surface. Thus, the top layer of resist is quickly ejected from the wafer's edge while the bottom layer still creeps slowly radially along the wafer. In this way, any 'bump' or 'ridge' of resist is removed, leaving a very flat layer. The photo resist-coated wafer is then prebaked typically at 90 to 100 °C for 30 to 60 seconds on a hotplate to drive off excess photoresist solvent. The evaporation of liquid solvents from the resist also contributes to the final thickness.

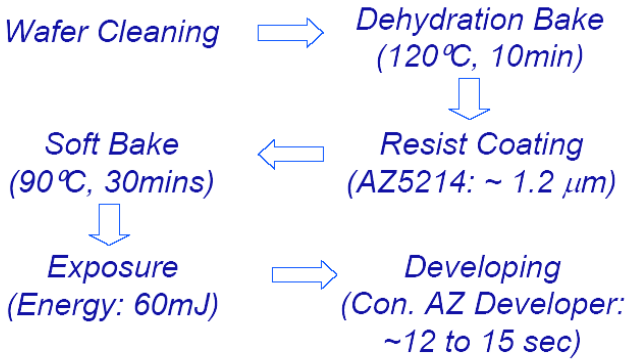

Figure 3-3 Basic Recipe for photolithography used in this work. The spin speed is 4800 rpm to achieve 1.2 um thickness AZ5214 resist. The exposure uses i-line 365nm.

After prebaking, the photoresist is exposed to a pattern of intense light. Optical lithography typically uses ultraviolet light. Positive photoresist, as used in this work, becomes soluble in the basic developer when exposed, while negative photoresist becomes insoluble in the (organic) developer. A post-exposure bake can be performed before developing, typically to help reduce standing wave phenomena caused by the destructive and constructive interference patterns of the incident light. The image for the mask is converted from a computerized data file to a series of polygons and written onto a square fused quartz substrate covered with a layer of chrome, which can be etched away, forming the pattern on the mask. The time used for development of the photoresist after exposure depends on the resist type and thickness chosen. The process parameters for three types of resist mainly used in this work are summarized in Figure 3-4, which work for most of the cases.

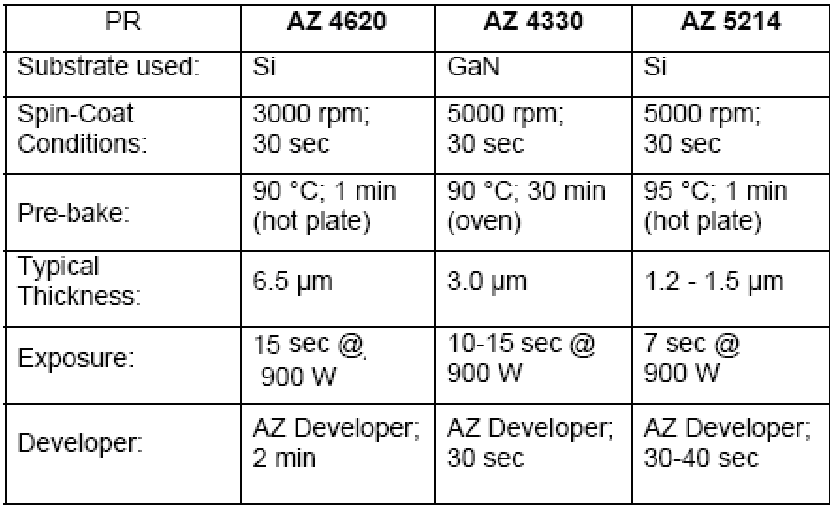

PR	**AZ 4620**	**AZ 4330**	**AZ 5214**
Substrate used:	Si	GaN	Si
Spin-Coat Conditions:	3000 rpm; 30 sec	5000 rpm; 30 sec	5000 rpm; 30 sec
Pre-bake:	90 °C; 1 min (hot plate)	90 °C; 30 min (oven)	95 °C; 1 min (hot plate)
Typical Thickness:	6.5 μm	3.0 μm	1.2 - 1.5 μm
Exposure:	15 sec @ 900 W	10-15 sec @ 900 W	7 sec @ 900 W
Developer:	AZ Developer; 2 min	AZ Developer; 30 sec	AZ Developer; 30-40 sec

Figure 3-4 Photolithography parameters for photoresists used in this work

The main advantage of using a mask aligner is the alignment of multiple masks in sequence to form the device structure. Figure 3-5 shows the aligned patterns from multiple masks which form the GaN LED arrays in this work. However, the minimum feature size of our mask aligner limited by diffraction is 1um, as shown in Figure 3-6, where the 1um wide grating (bottom) shows much lower contrast than 6um width grating (top). Advanced lithography techniques for submicron feature size used in this thesis will be introduced in subsequent sections.

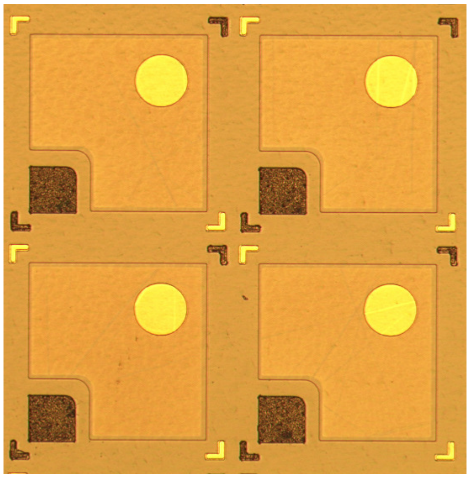

Figure 3-5 Microscope image showing the alignment of patterns from multiple LED masks

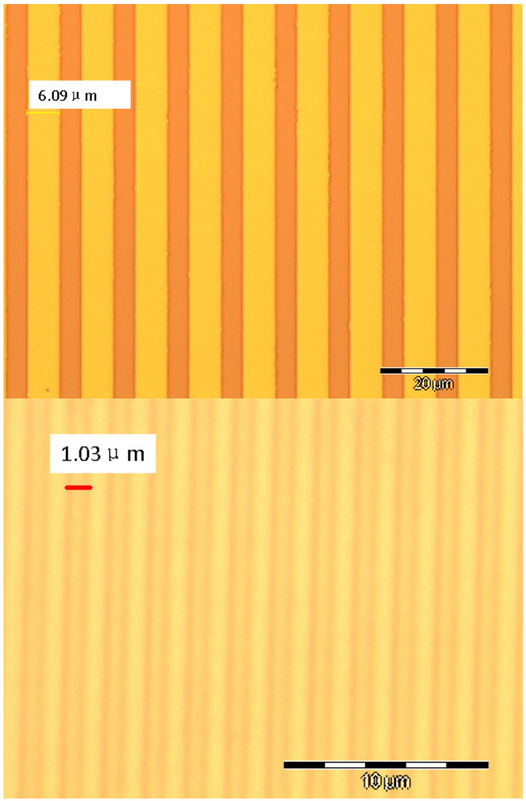

Figure 3-6 Microscope image of grating patterns generated by our mask align. The grating with 1um width (bottom) shows much lower contrast than that with 6um width (top).

3.2.2 Electron-beam lithography

The technology for electron-beam lithography (EBL) evolved from the scanning electron microscopes, which is introduced in the later part of this chapter. The main advantage of EBL is its very high resolution to create extremely fine patterns [1]. EBL consists of scanning a finely focused beam of electrons across a surface covered with an electron-sensitive resist film, thereby depositing energy in the desired pattern in the resist film. The main attributes of this technology includes: (1) capability of very high resolution (sub-10nm), (2) it can work with a variety of materials and infinite number of patterns, (3) a few orders of magnitude slower than optical lithography, (4) complicated instrumentation which costs many millions of dollars and require frequent maintenance.

The resolution of an e-beam lithography system is first determined by the beam diameter, which can be as small as a few nanometers. The ultimate resolution however is dependent on a number of parameters, such as the beam accelerating voltage, the type of substrate material, the resist material and thickness, and the resist development process. One of the dominant mechanisms that influence pattern resolution is electron scattering when the electrons hit the sample. Electrons traveling through a resist material undergo collisions with the constituent atoms, which cause the electrons to scatter and thus spread out the electron beam and increase the beam width. Most of the collisions occur in the substrate material, which cause the electrons to be scattered backwards into the resist, exposing the resist over a large area. This backscatter is dependent on the substrate material's atomic number, and higher numbers will scatter more electrons.

As a result, the dose delivered by the electron beam tool is not confined to the shapes that the tool writes thus the nominal exposed area can be broadened or distorted depending on the pattern such as if there is a bent. Such an effect is called the proximity effect. A number of schemes can be used to correct or minimize the proximity effect, such as dose modulation [2], pattern biasing [3] and GHOST [4]. E-beam resists are the recording and transfer media during e-beam lithography. In positive resists, electron irradiation breaks polymer backbone bonds into fragments of lower molecular weight. A solvent developer selectively cleans away the fragments, thus a positive tone pattern is formed in the resist film. Typical electron-beam resists are organic polymers such as polymethylmethacrylate (PMMA), which has very high resolution, the ability to form multi-layers for lift-off processes, but has poor resistance to plasma etching. Instead, the ZEP resist can work as a better etching mask. The negative resists work by cross-linking the polymer chains together during e-beam exposure, rendering them less soluble in the developer. Special care must be taken to resolve the charging problem that may cause considerable distortion when the e-beam exposure is performed on insulating substrates.

Primary application of e-beam lithography is for mask-making to support integrated circuit industry, typically the chrome-on-glass masks used in optical lithography. It is preferred because of its flexibility in providing rapid turnaround with the pattern described only by a computer CAD file. The second application is direct writing for manufacturing of small volume specialty products such as GaAs integrated circuits and optical waveguides [5].

Last, e-beam lithography is also used in the research of scaling limits of integrated circuits [6]. In addition to these applications, e-beam lithography has also been widely used as a powerful nanolithographic tools in the research of nanoscience and nanotechnology.

In this project, we perform e-beam lithography using a Sirion 200 scanning electron microscope equipped with a Nabity Nanometer Pattern Generation System (NPGS). Figure 3-7 shows a schematic NPGS setup. A Picoammeter is used to read the beam current hitting the sample. A beam blanker is installed, which has a response time of less than 5 μs at the output voltage of 135 V in our system, as shown in Figure 3-8. The basic steps for the pattern generation process consist of the design of patterns, creation of parameter run file, and pattern writing with alignment for multilevel lithography. Pattern sizes may range from the maximum field of view of the microscope down to the nanoscale. However, the writing resolution will decrease as the field size is increased. For the nanograting pattern generated in this work, a maximum field size is 300um by 300 um square.

Multi-pixel exposure scheme was employed, in which a single pattern is divided into many exposure pixels. The pixel dose, namely the dosage for each exposure pixel, is given by the product of the beam current and the dwell time of beam current staying on that pixel. The beam current must be adjusted according to the minimum size of the pattern. We use beam current of 20 pA for structure with periodicity less than 400nm in this project. The corresponding pixel spacing was selected to be 20 nm. The pixel dosage could be used as a lithographic tuning of pattern dimensions within same period.

Due to the trial and error nature of the e-beam writing process, the electron beam control parameters like stigmatism and dosage control always need adjustment from time to time, and various undesired patterns can result, e.g. pattern bias and non-uniformity, over-dosage, under-dose, as well as over develop time as shown in Figure 3-9. After optimizing the dosage and developing time, and most importantly, adjusting stigmatism, uniform pattern could be achieved having tunable holes size within same period, namely duty ratios, as shown in Figure 3-10.

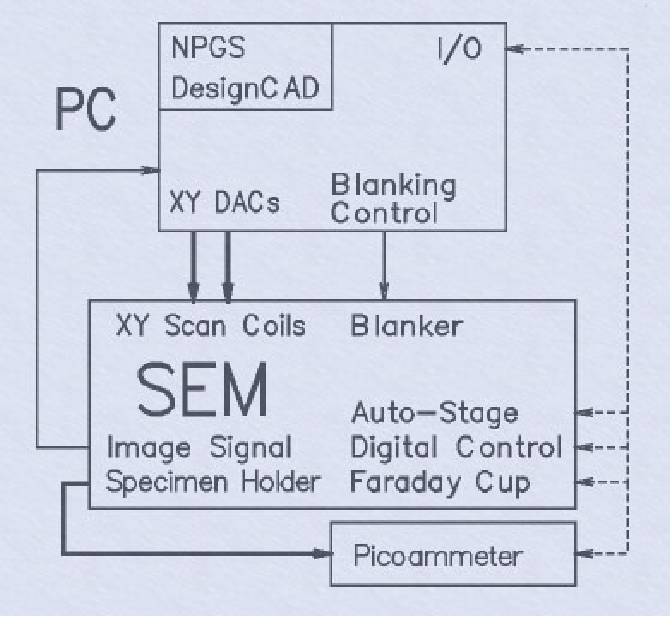

Figure 3-7 Schematic diagram of a Nabity Nanometer Pattern Generation System (NPGS) (adapted from *http://www.jcnabity.com*)

Figure 3-8 Equipment for e-beam lithography setup at Singapore Synchrotron Light Source (http://ssls.nus.edu.sg) in this work

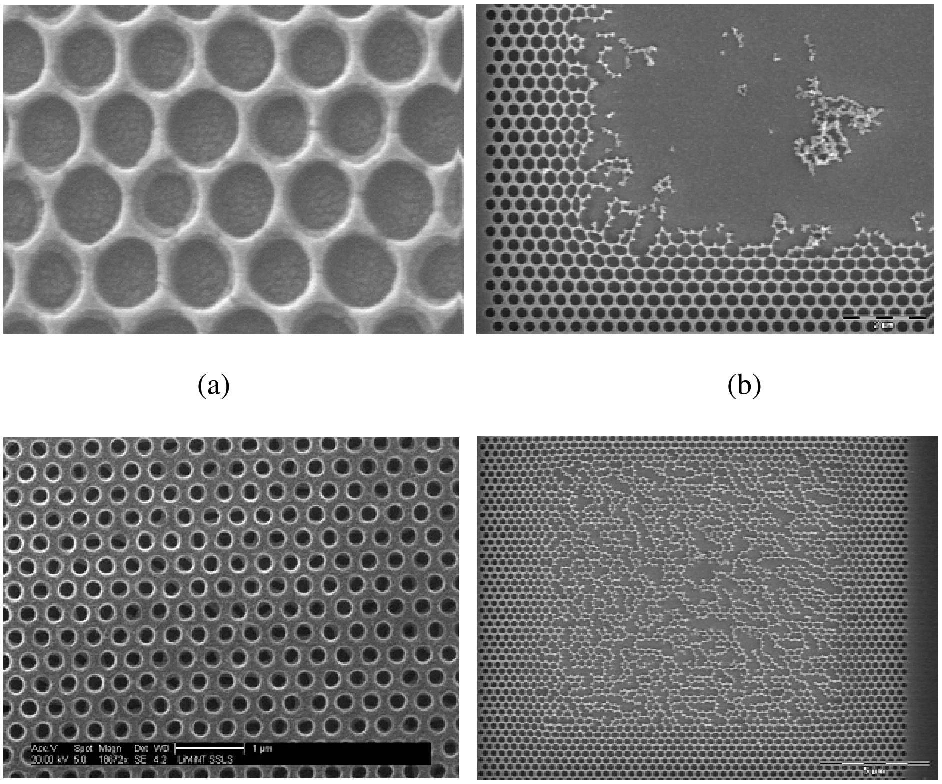

(a) (b)

(c) (d)

Figure 3-9 SEM images of various undesired patterns formed on the e-beam resist. (a) pattern bias and non-uniformity (b) over-dosage (c) under-dose (d) over developing time

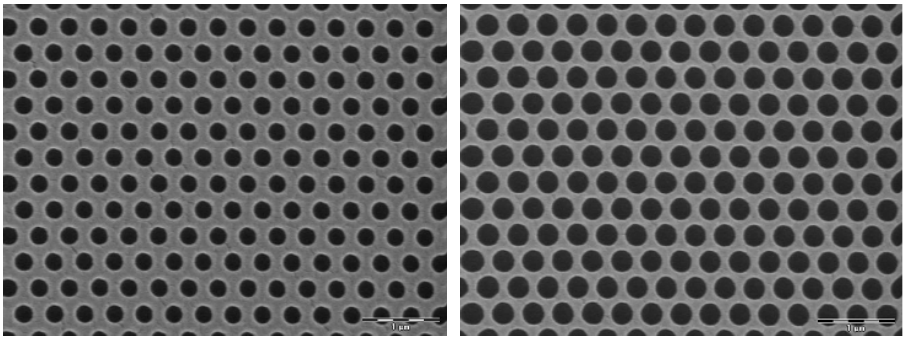

(a) (b)

Figure 3-10 SEM images of uniform pattern with duty ratios (a) ½ and (b) ¾

Repeatable nanowall pattern formed after development without distortion due to proximity effect has minimum width of 50nm. Further increasing the exposure dose or putting neighboring holes closer will distort the pattern as verified in experiment. At this limit the pattern is uniform over a large area as shown in Figure 3-11. It is noted that, the stigmatism has to be extremely well adjusted to reach this limit.

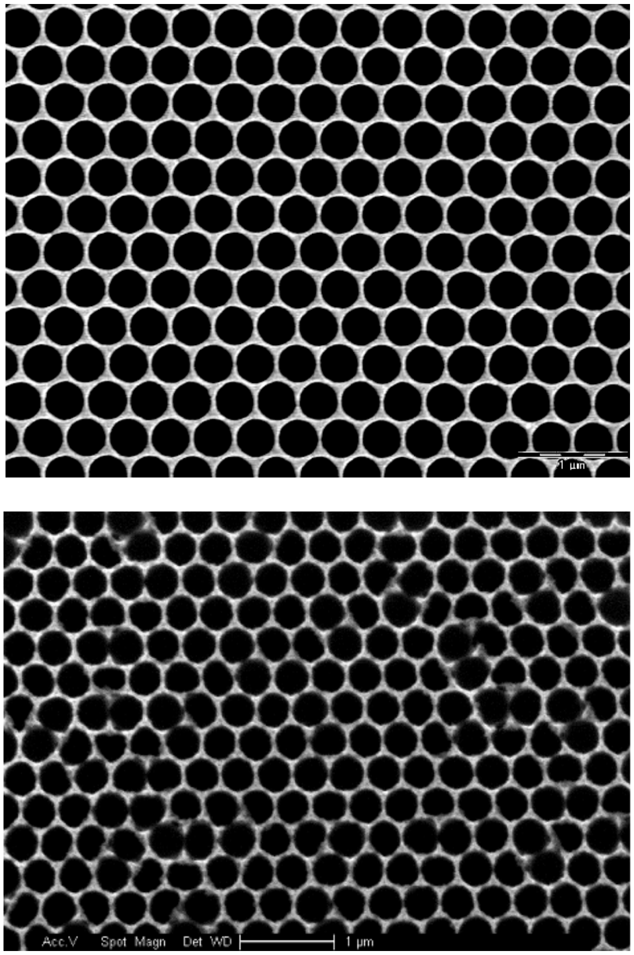

Figure 3-11 SEM image of pattern with minimum width of 50nm. Further scaling down makes the pattern distorted

3.2.3 Nanoimprint lithography

A major drawback of EBL is that it is a serial process. Patterns are exposed on a point-by-point basis. As a parallel process, nanoimprint lithography (NIL) was first developed by Stephen Y. Chou's group in 1996 [7]. NIL involves a pattern transfer from a rigid mould to a thin layer of polymer, followed by removing the residual polymer in the recessed areas of the patterns. NIL can be divided into two major categories depending on how the patterns are transferred to the polymer layer,: thermoplastic NIL and step and flash imprint lithography (SFIL) [8]. In a thermoplastic NIL process, the resist layer is physically deformed by the pre-defined patterns on the mould with a temperature above the glass-transition point of the polymer. In SFIL, UV curable liquid resist is coated on the substrate, which gets solidified after being cured in UV light under pressing of the mould. NIL has the advantages of simplicity, high throughput and low cost. A fine resolution down to 10 nm can be achieved as it is not limited by diffraction or scattering effects that are involved in optical and e beam lithography process. The disadvantages and issues for NIL involve template fabrication and the residue layer removal. The template fabrication relies dominantly on e-beam lithography, so the throughput is still very low. The existence of a residual layer is characteristic of NIL, which affects the control for critical dimension. NIL has been extensively used for the fabrication of devices for optical, electrical, photonic, magnetic and biological applications [9-14]. Three-dimensional (3-D) structures can be directly patterned by NIL with reduced number of process steps [11]. Currently the most popular mould materials include Si and Ni. The polycrystalline Ni moulds have the advantages of high corrosion resistance and elastic deformability, thus are considered as a more industrially relevant alternative compared with the Si counterparts [15].

In this project, the thermoplastic NIL was carried out in an Obduct NIL-4 nanoimprinter system. The maximum working temperature and pressure are 250 °C and 60 bar respectively.

3.2.4 Plasma etching

Etching is a necessary process to fabricate polarized LED in this thesis. There are many different types of etching, which can be grouped as isotropic etching and anisotropic etching. Isotropic etching, typically done in hot acid baths, has the advantage of simplicity. This is the reason we tried wet etching for subwavelength grating fabrication initially. However, because the etch will act in all directions, its usefulness is limited to the fabrication of large feature sizes. Beyond its isotropic nature, the surface tension of the chemical bath is often high enough so that it will not penetrate between two closely spaced resist strips and no etching takes place. So we pursued anisotropic etching, which normally use a high-speed stream of plasma to produce the ions to remove target materials. This method is called plasma etching.

Plasma etching is widely used for pattern transfer in semiconductor manufacturing. Two main plasma etching will be used in this project, the first is known as ion beam etching or ion milling, where energetic ions strike the sample and chip away the surface by momentum transfer, atom by atom. The second is though chemical reactions, where reactive particles attack the sample surface and convert the atoms into volatile compounds. Through a balance of chemical reaction and physical milling, high etch rates and high anisotropy can be achieved in an optimized etching process, known as reactive ion etching (RIE). Both etching processes use plasma to produce ions for etching. The difference is the composition of the plasma. In ion milling, the plasma is non-reactive, such as argon. In RIE, the plasma constituents depend on the material to be etched.

3.2.4.1 Ion Milling

Ion milling is a technique conceptually similar to sandblasting. In place of actual grains of sand, submicron ion particles are accelerated and bombard the surface of the target which is mounted on a rotating table inside a vacuum chamber [16]. The target is typically a wafer or substrate that requires the material to be removed by atomic sandblasting or dry ion etching. As with any etching process, a mask, e.g. photoresist, is applied to the work element to protect areas not to be etched prior to its introduction into the ion miller. The resist protects the underlying material during the etching process which may be up to four hours or longer, depending upon the amount of material to be removed and the etch rate of the materials.

During ion milling process, Argon ions contained within the plasma are formed by an electrical discharge and are accelerated by a pair of optically aligned grids. The highly collimated Argon ion beam is focused on a tilted work plate that rotates during the milling operation. This ensures uniform removal of waste material resulting in straight side walls in all features with zero undercutting. The work plate can be angled to address specific requirements, but it usually sits at an angle 8 to 10 degrees to the ion beam. A neutralization filament uses an independent electron source to prevent the buildup of positive charge on the work plate. The highly collimated, directional ion flux allows for anisotropic etching of any material. The precision and its attendant repeatability is ultimately the key strength of the strongly collimated ion beam milling process. Other methods of etching such as the chemical process simply do not deliver the same level of precision that an ion beam etch can. That is the main reason we use ion milling as our fabrication tool of subwavelength grating. Furthermore, for some materials such as Platinum that cannot be etched effectively using a chemical process, ion milling can just provide a universal etching solution.

In this work, we will use ion milling to etch away some portion of metal layer with resist as the etching mask, so as to form metallic grating by transferring the grating pattern from resist to metal layer. Figure 3-12 shows the SEM image of uniform aluminum grating fabricated by ion-milling process. The gratings in images (a) and (b) with different magnification have grating period of 2um defined by photolithography, where AZ5214 photoresist with a thickness of 1.3 um is used as the mask for ion milling. The gratings in the two lower images with different magnification show grating period of 500 nm defined by nanoimprint lithography, where PMMA with a thickness of 230nm is used as the mask for ion milling. In both cases the thickness of aluminum layer is 200nm and the ion milling duration is 15 min. The ion milling power is 160W , with a beam current of 110 mA, the chamber pressure during process is about 3.47×10^{-4} Torr.

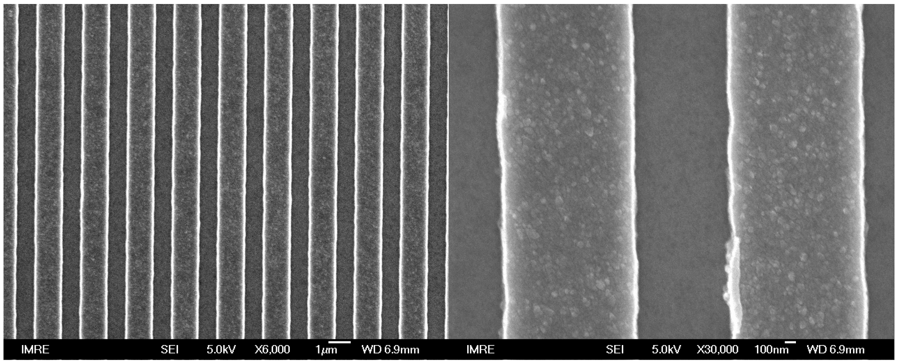

(a) (b)

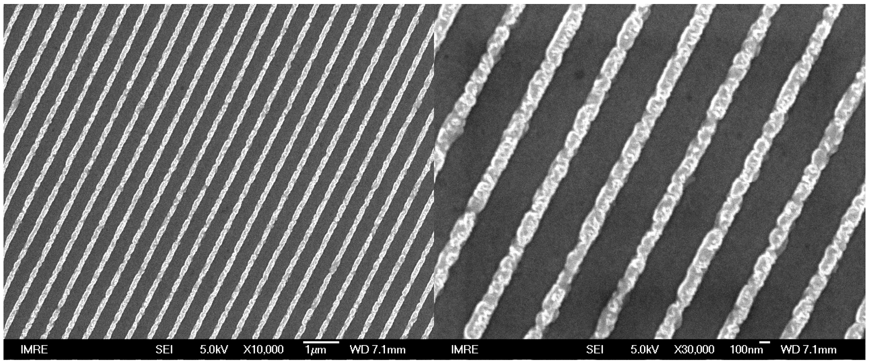

(c) (d)

Figure 3-12 SEM image of uniform aluminum grating fabricated by ion-milling process. (a) and (b) are images with different magnification for grating period of 2um defined by photolithography. (c) and (d) the lower two images are images with different magnification for grating period of 500 nm defined by nanoimprint lithography.

To determine the etching rate of aluminum under ion milling, we measured the etch depth on aluminum before it being completely etched away. Figure 3-13 shows the cross section SEM view of the aluminum grating partially etched by ion milling. The cross section profile of aluminum grating is almost rectangular in shape with its sidewalls remaining vertical and clean. The etch depth measurement shows an etch rate of 15 nm /min.

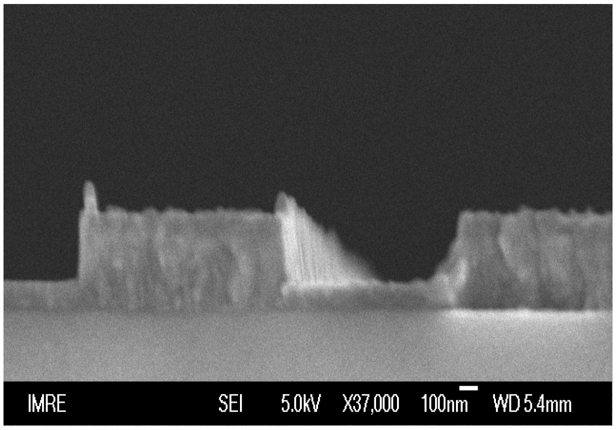

Figure 3-13 Cross section SEM view of aluminum grating before it being completely etched away

3.2.4.2 Reactive ion etching

Reactive ion etching (RIE) is a widely utilized dry-etch technique and requires a relatively simpler apparatus compared to ion beam etching [17, 18]. In a typical RIE process, BCl_3 is used for the etching of GaN. The major two types of reaction species involved in RIE are the radicals (Cl^*), namely atomic species in excited states produced from dissociation, and the ions (Cl^-, BCl_2^+) produced from ionization [19]. As the energy required for ionization is much higher than that for dissociation, the number of radicals is much larger than that of ions, therefore the neutral Cl^* radicals are responsible for chemical reaction. The reaction products of $GaCl_2$, and $GaCl_3$ are volatile and can be easily removed.

In this project, plasma etching is primarily used for InGaN LED mesa etch using an ICP-RIE system (Unaxis Shuttle Lock ICP System). The optimized process condition for ICP etching use 20sccm BCl_3 and 10 sccm Cl_2 under pressure of 5 mtorr at 6 °C. RIE power is 200W and ICP power is 500W.

3.3 Characterization tools

3.3.1 Scanning electron microscope

The scanning electron microscope (SEM) is an extensively used tool to produce images of a sample surface with high resolution. A typical SEM contains an electron gun, a focusing/lens system, an electron detector and a cathode ray display tube (CRT) [20]. The source electrons can be produced by field emission. The acceleration voltage can range from a few hundred volts to 50 kV. Condenser lenses can focus the electrons into a fine beam spot of a few nanometers. The spatial resolution of the SEM depends on the size of the electron spot which in turn depends on the magnetic electron-optical system.

Interaction of primary electrons with the sample surface leads to the emission of various signals including secondary electrons, back-scattered electrons and X-rays, as is shown schematically in Figure 3-14. The most commonly used imaging mode monitors secondary electrons that have low energy (< 10 eV). Only those secondary electrons close to the surface can escape from the surface and be detected due to low energy. Hence, the images formed by the secondary electrons are a good description of the surface topography of samples. The electrons are detected and the resulting signal is rendered into a 2-D intensity distribution that can be viewed as a digital image.

Back scattered electrons can also be detected, which could be used to detect contrast between areas with different chemical compositions, since heavy atoms with a high atomic number scatter electrons more than the light ones. Energy-dispersive (EDX) and wavelength-dispersive spectrometers can be coupled with an SEM, providing information about the chemical composition.

In this project, the Sirion 200 field emission SEM is used to characterize the surface morphology of sample. An acceleration voltage of 5-10 kV was used in most of the subsequent experiments, which could give resolution of 50nm feature size. A thin Au layer was coated on sample surface to avoid charging effect.

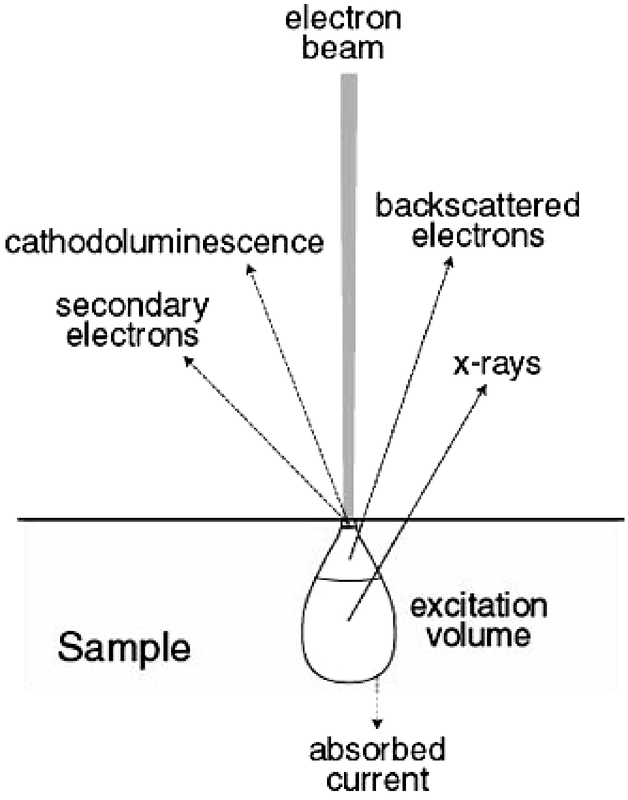

Figure 3-14 Interaction between incident electrons and specimen.

3.3.2 Atomic force microscopy

The atomic force microscopy (AFM) is one type of scanning probe microscopy, where a sharp probe is scanned across a surface and the probe/sample interaction is monitored. There are three primary modes of AFM: contact mode, non-contact mode and tapping mode [21].

Tapping Mode (TM) AFM operates by scanning a tip attached to the end of an oscillating cantilever across the sample surface, as shown in Figure 3-16. The cantilever oscillates at its resonance frequency (typically 200 ~ 400 kHz) with an amplitude ranging typically from 20 nm to 100 nm. The motion of the cantilever is sensed by a position- sensitive photodetector. The tip lightly “taps” on the sample surface during scanning, contacting the surface at the bottom of its swing. Constant tip-sample interaction is maintained during imaging by maintaining a constant oscillation amplitude. One advantage of TM AFM over contact mode AFM is the virtual elimination of lateral shear forces, which often results in the scrapping and damage of soft samples. A typical lateral resolution of 1 nm ~ 5nm can be achieved in TM AFM. The shape of the tip (the radius of curvature and tip sidewall angles) also affects the AFM resolution and images.

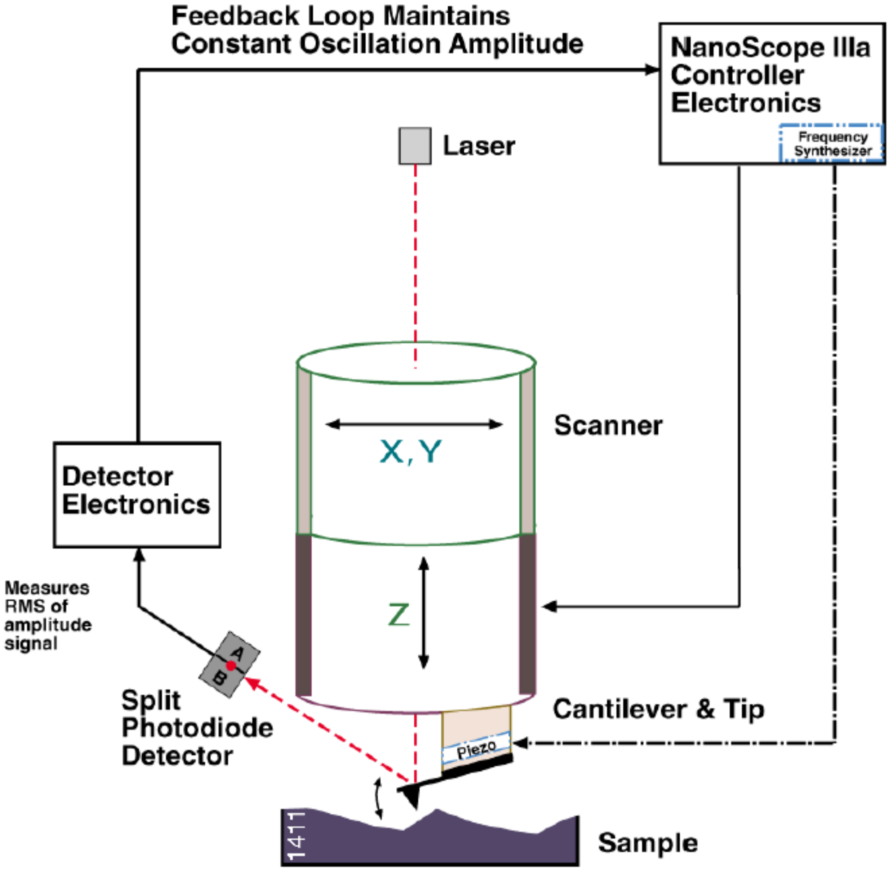

Figure 3-15 Schematic instrumental setup of Tapping Mode AFM [21]

In this project, a TM AFM from Digital Nanoscope was used to investigate the surface morphology of the nanostructures with sub-100-nm lateral dimensions. With sharp silicon tips, the detailed structural information was obtained. Extreme care should be taken when manipulate the AFM cantilever because it is fragile and expensive, especially for the case of scanning nano-gratings or nano-slits in this work where the tip with high aspect-ratio is used

After mounting the cantilever into the holder, it is aligned with the help of a red laser to ensure that the laser spot is located at the tip-side so that the reflected light hits the center of the detector to get an optimal signal. After tuning the cantilever and resetting it to zero-phase, the region of interest is chosen under microscope and the tip is brought to close vicinity of the sample surface by the feedback electronics. Then a rough scan with high scan rate is started and the signals are monitored by the trace and re-trace information. If the trace information and re-trace information are close to each other, the signal is considered to be accurate. Then a fine scan is performed with a lower scan rate to obtain high quality images.

Figure 3-16 is the AFM image showing 3D surface morphology and cross section profile of the hexagonal packed holes array fabricated by e-beam lithography as discussed in previous section. The AFM result is in agreement with SEM images.

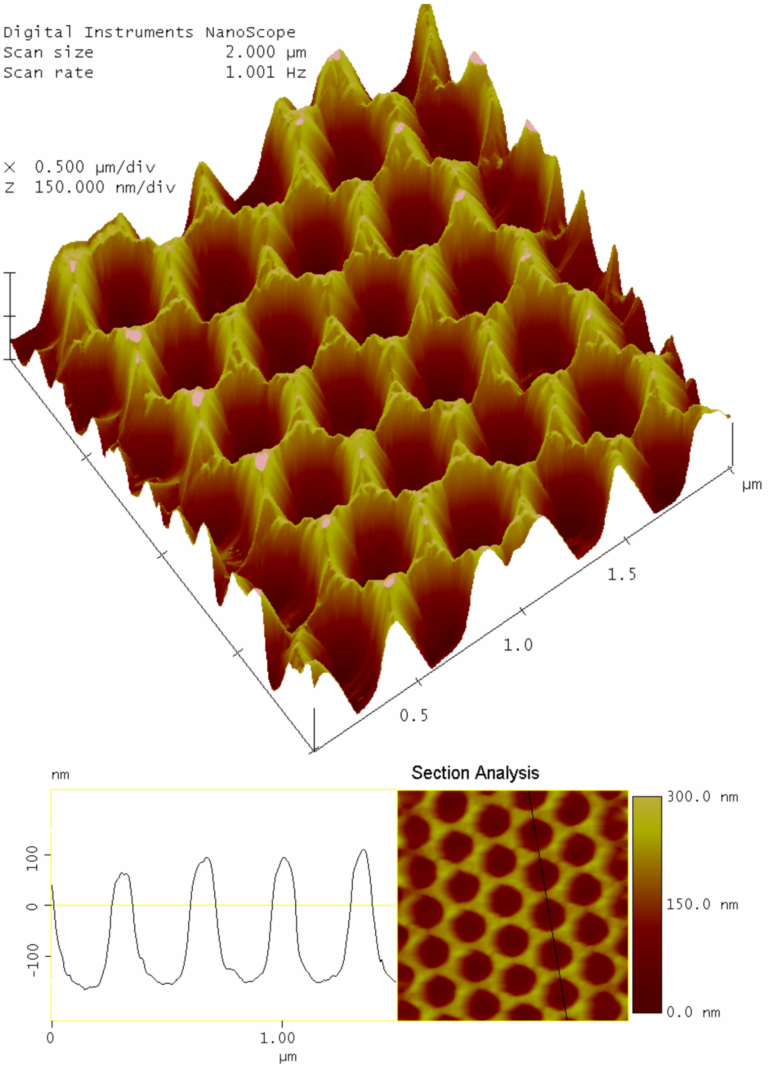

Figure 3-16 AFM image showing 3D surface morphology and cross section profile of the hexagonal packed holes array fabricated by e-beam lithography

3.3.3 Fourier transform infrared spectroscopy (FTIR)

Fourier transform infrared spectroscopy (FTIR) is a technique which is used to obtain an infrared spectrum of absorption or emission. An FTIR spectrometer simultaneously collects spectral data in a wide spectral range.

Figure 3-17 shows the VERTEX 80 vacuum FTIR spectrometer used in this work. It is equipped with optical components to cover the spectral range of terahertz. Just like any spectroscopy, the goal of our FTIR measurement is to measure how well a sample absorbs light at each wavelength. The most straightforward way to do this is to shine a monochromatic light beam at a sample, measure how much of the light is absorbed, and repeat for each different wavelength. Here we use an efficient way to obtain the same information. Rather than shining a monochromatic beam of light at the sample, our FTIR shines a beam containing many different frequencies of light at once, and measures how much of that beam is absorbed by the sample. Next, the beam is modified to contain a different combination of frequencies, giving a second data point. This process is repeated many times. Afterwards, a computer takes all this data and works backwards to infer what the absorption is at each wavelength through Fourier transform. Since the raw data collected for light absorption at each mirror position belongs in the length domain, Fourier transform inverts the dimension to the reciprocal length domain, which is the wave number domain. The resolution achieved in our step is 0.2 cm^{-1}.

Figure 3-17 VERTEX 80 vacuum FTIR spectrometer used in this work

3.3.4 Terahertz time-domain spectroscopy (THz-TDS)

Terahertz time-domain spectroscopy (THz-TDS) is a spectroscopic technique in which the properties of a material are tested by short pulses of terahertz radiation. The generation and detection scheme is sensitive to the sample material's effect on both the amplitude and the phase of the terahertz radiation, thus can provide more information than conventional Fourier-transform spectroscopy, which is only sensitive to the amplitude. Typically, the terahertz pulses are generated by an ultra-short pulsed laser and last only a few picoseconds. A single pulse can contain frequency components covering the whole terahertz range from 0.05 to 4 THz.

In this work, the THz-TDS setup utilizes a 76MHz fs laser. The spectral range of this setup is 0.1~4THz with spectral resolution 15GHz. The THz radiation from the THz-TDS is linearly polarized. After warm up of the laser, we first do an air background scan. After that we scan our sample by placing the sample grating parallel or perpendicular to the inherent polarization direction of the THz radiation, this corresponds to TE and TM incidence, respectively. For every scan we need to wait about 60 sec for the signal to get stabilized after placing the samples. Finally, we can get both time domain signal and transmission spectrum in frequency domain through Fourier transform.

3.4 Summary

The main fabrication and characterization tools used in this project have been reviewed, namely photolithography e-beam lithography, nanoimprint lithography, plasma etching, SEM, AFM, FTIR and THz-TDS.

Chapter 4: Simulation and Design of Subwavelength grating

4.1 Introduction

In this chapter we will use Rigorous Coupled Wave Analysis (RCWA) and Finite Difference Time Domain (FDTD) method to model the performance of subwavelength grating and design polarized LED. The choice of material to use for visible-wavelength subwavelength metallic grating is discussed, and the effect of the physical parameters on the polarization properties is investigated in details.

4.2 Comparison of different metals

An important consideration for visible subwavelength metallic nanograting (SMNG) is the correct choice of metal for the grating. In the infrared and especially the microwave regions of the spectrum, metals are typically assumed with reasonable accuracy to have infinite conductivity. In the visible, however, this assumption is not justified and cannot be made. Like all materials, the indices of metals change a great deal over the visible spectrum. It is then important to find the complex value of the indices of refraction for various metals and compare them to find the most suitable material for visible polarization applications.

Unfortunately, thin metal films are difficult to characterize. The indices of refraction vary with changes in growth conditions, such as temperature, thickness, vacuum level, deposition technique, growth rate, and with wavelength. E. D. Palik's Handbook of Optical Constants of Solids is one of the definitive works on the subject and was used to determine base values for the metal indices of refraction in this thesis [1]. The real and imaginary parts of the index of refraction for aluminum, gold and silver are shown in Figure 4-1. As can be seen, there is quite a variation between the indices of the metals and each of them shows considerable dispersion over the visible spectrum.

To ensure accurate results, when a wavelength evaluation is done at a wavelength that is not in the table, the n and k values for that certain wavelength were determined by linearly interpolation from the data presented in Figure 4-1. Based on these values, the transmission spectra were calculated using RCWA for aluminum, gold and silver in order to select the best material for the metal grating. The dimension of sample grating used for this calculation has a period of 150nm, grating height of 120nm and duty cycle of 0.5.

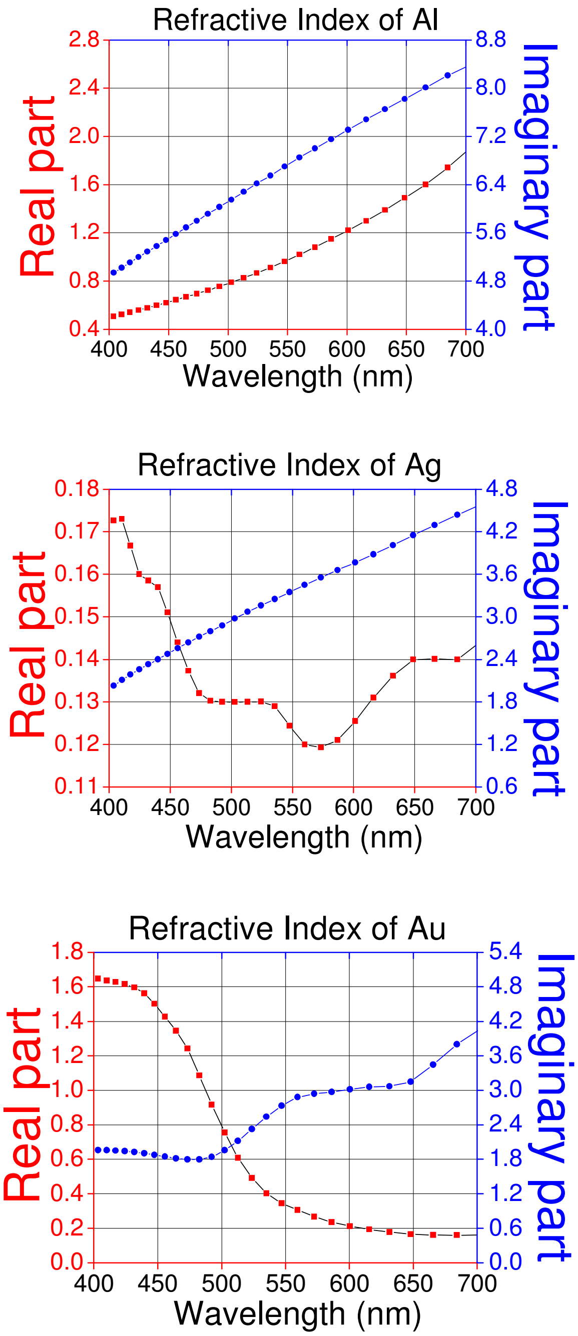

Figure 4-1 The real and imaginary parts of the index of refraction for aluminum, gold and silver in visible range

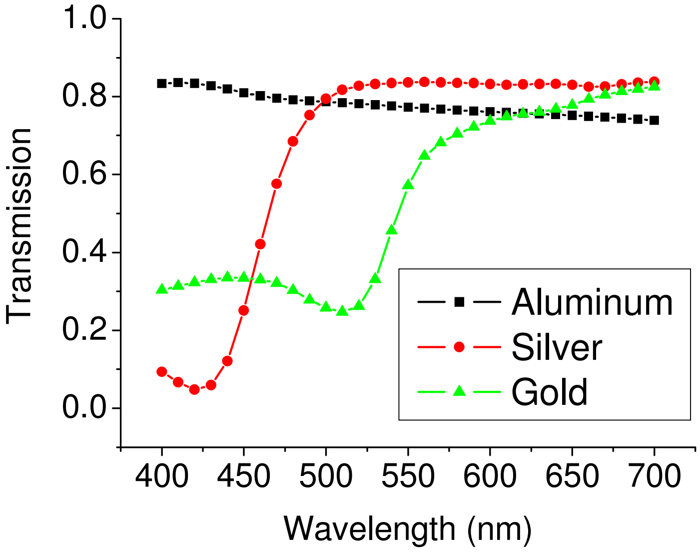

Figure 4-2 Transmission efficiency calculated by RCWA for aluminum, gold and silver grating in visible range. The dimension of sample grating used for this calculation has a period of 150nm, grating height of 120nm and duty cycle of 0.5.

As shown in Figure 4-2, aluminum gives the highest transmission efficiency in average of whole visible range compared with silver and gold. Gold, while being the material of choice for infrared applications, is not as good for the visible wavelength. Silver sits in the middle. As can be seen from Figure 4-1, the material with the highest imaginary values of refractive index is the best choice for used in grating polarizers. Aluminum also adheres well to substrates, is relatively easy to deposit, and is commonly used in semiconductor industry, making it a very attractive choice from a fabrication point of view as well. It is known that upon exposure to the atmosphere at even a pressure as low as 5 x 10^{-6} Torr [2], a thin dielectric oxide layer forms on the surface of the aluminum, generally from 2.0 to 5.5 nm thick on the aluminum [1]. We repeat the simulation of aluminum grating shown in Figure

4-2, but with 5nm oxide added having index of refraction is 1.77 [1]. It shows that this oxide film has only a small effect on the performance of the grating.

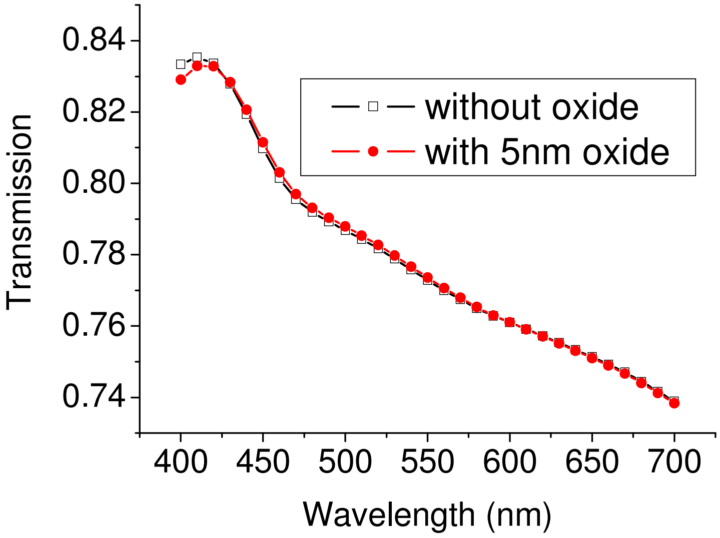

Figure 4-3 The effects of the oxide layer on the properties of an aluminum grating. The grating parameters are same as in Figure 4-2.

Most metals including silver also form such an oxide layer, with the exceptions of gold and platinum. While gold does not form an oxide, it has a low transmission at shorter wavelengths (<650 nm), a low extinction ratio, and suffers from adhesion problems. Often a thin layer of a different metal such as titanium is required because the gold will not adhere to the substrate, complicating the design and fabrication process. Other metals, not shown here, also do not exhibit properties as favorable as those of Al.

4.3 Effect of physical parameters of gratings

There are four important physical parameters influencing the performance of SMNG. These are the period, duty cycle, thickness and the angle of incidence of the beam. From a design point of view, our idea is to perform simulation to investigate how the grating performances are influenced by these parameters and determine the optimized parameter to guide our experimental work.

4.3.1 Period of grating

The most important physical parameter in a SMNG is the period. The period is the length of repeating unit, *p*, as defined in the Figure 2-1. The period determines the minimum wavelength that can be effectively polarized and, from a manufacturability point-of-view, sets limits on reasonable values for the duty cycle and wire thickness. The duty cycle is the ratio of the distance occupied by the wire over the period, namely $f = d / p$ as defined in the Figure 2-1.

It is shown in Figure 4-4 that, as the period is reduced, the transmission coefficient (b) and the extinction ratio (c) both increase. The transmission coefficiency and the extinction ratio are defined in Eq. 2.4.

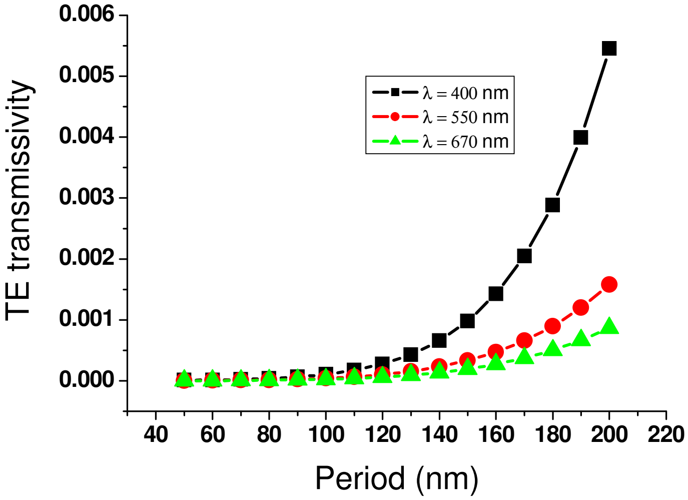

(a)

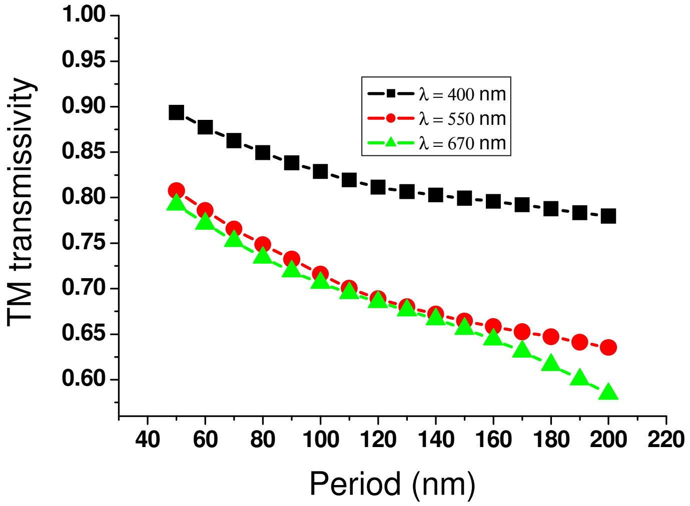

(b)

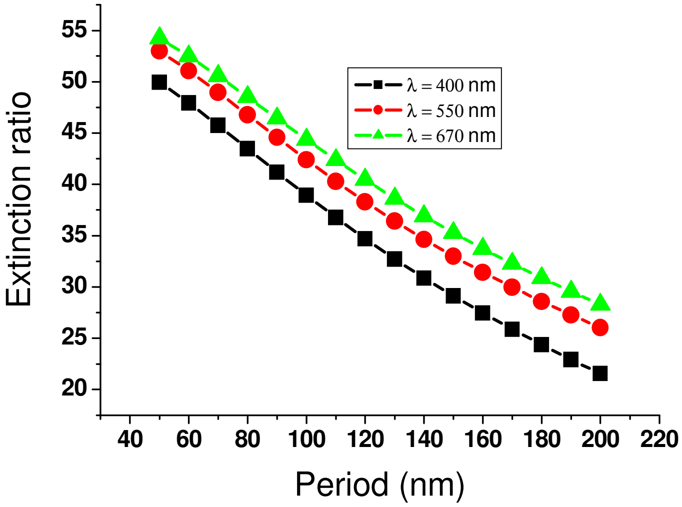

(c)

Figure 4-4 Polarization performance vs. period of grating. The wire thickness is 120 nm, the duty cycle is 50%, and it is at normal incidence. Reducing the period increases both the transmission efficiency and extinction ratio of the grating.

These results can be anticipated by understanding the qualitative description of WG polarizers. As the period is reduced, the wires become closer together and it is easier for the TE field to excite the electrons to along the length of the wires. Similarly, the wires are narrower for the TM field and so the electrons have even less space in which they can vibrate. This results in an increase in the attenuation of the TE light and a decrease in the attenuation of the TM light (thus an increase in the transmissivity of TM light). Therefore the polarizer has a higher transmission coefficient and a higher extinction ratio. This increased attenuation of the TE light for reduced period could also be understood by EMT theory. As described in Chapter 2, the subwavelength metallic grating is equivalent to a metal sheet for TE light under EMT approximation. EMT approximation prefers that the period is as small as possible compared with the wavelength. Therefore, with reduced period, the subwavelength metallic grating is more closed to a metal sheet, thus there is an increased attenuation. Ultimately, the period should be as small as possible for the most beneficial polarization properties.

4.3.2 Duty cycle of grating

The effect of changing the duty cycle is illustrated in Figure 4-5. For a given period and wire thickness, increasing the duty cycle increases the extinction ratio at the cost of a reduced transmission coefficient while decreasing the duty cycle has the opposite effect. By varying the duty cycle, we can fine tune a SMNG to get the exact behavior required. For example, if a high extinction ratio is vital, we can sacrifice some transmission to increase the extinction ratio by increasing the duty cycle. This behavior can also be understood qualitatively. As the duty cycle is increased, the wires get closer together, again allowing the TE field to easily excite the metal electrons and attenuate the TE field. However, the wires also get wider, and so the TM field can also more easily excite the electrons to move, attenuating the TM field and reducing the transmission coefficient. The increased attenuation in the TE field is proportionately higher than the reduction in TM transmission, leading to an increase in the extinction ratio. The opposite trend occurs if the duty cycle is reduced.

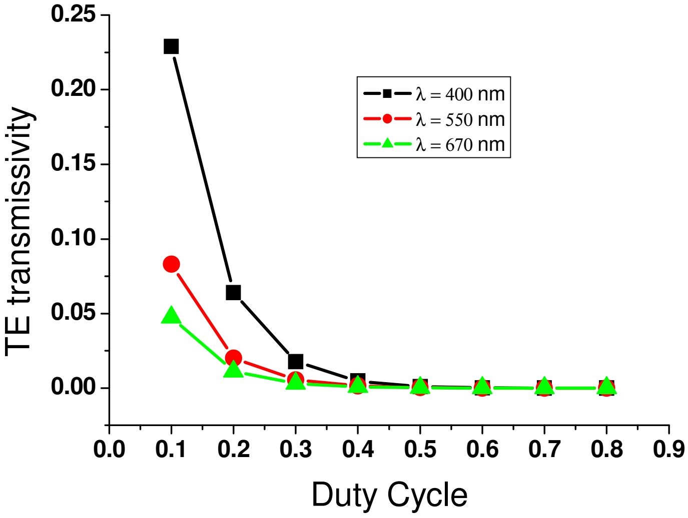
TE transmissivity
0.25
0.20
0.15
0.10
0.05
0.00
0.0
0.1
0.2
0.3
0.4
0.5
0.6
0.7
0.8
0.9
Duty Cycle
λ = 400 nm
λ = 550 nm
λ = 670 nm

(a)

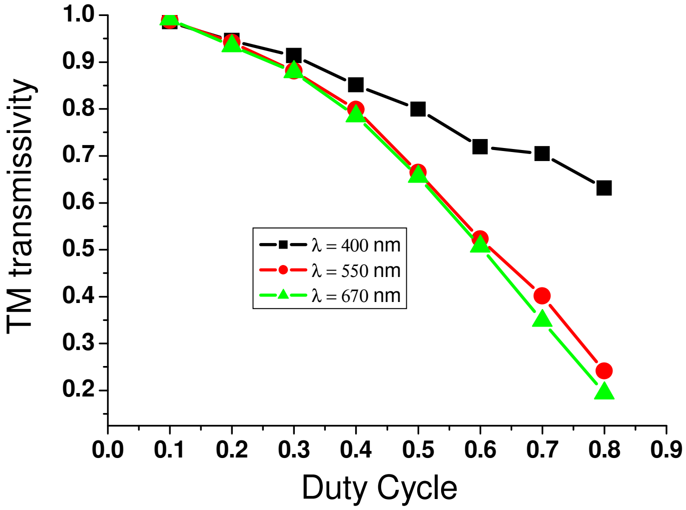
TM transmissivity
1.0
0.9
0.8
0.7
0.6
0.5
0.4
0.3
0.2
0.0
0.1
0.2
0.3
0.4
0.5
0.6
0.7
0.8
0.9
Duty Cycle
λ = 400 nm
λ = 550 nm
λ = 670 nm

(b)

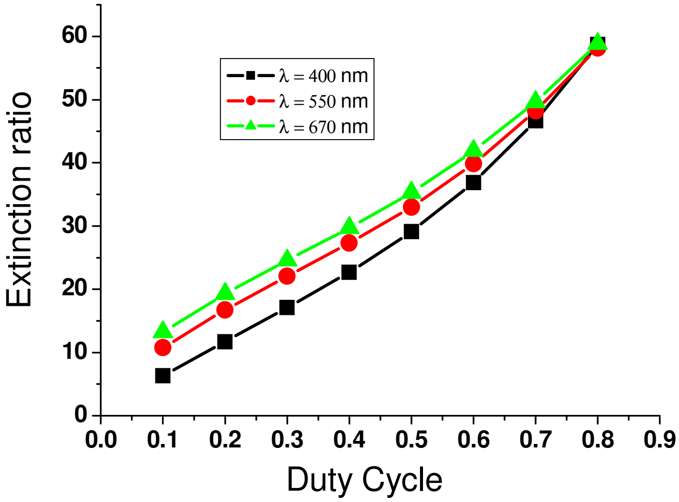

(c)

Figure 4-5 Polarization performance versus duty cycle. The grating period is 150nm, wire thickness is 120 nm, and it is at normal incidence. As the duty cycle increases, the transmission coefficient decreases and extinction ratio increases, and vice versa.

4.3.3 Thickness of grating

Not surprisingly, as the thickness of the grating s is increased, the TE transmission is reduced. Since the TE light sees the grating region as an absorbing film, increasing the grating thickness increases the absorption. The TM light sees the grating region as weakly absorbing dielectric material. Both of these effects lead to a greatly increased extinction ratio for the polarizer. This is illustrated in Figure 4-6, where the sinusoidal behavior of the transmission coefficient is due to interference effects, similar to other thin films. Unfortunately it is not possible to set the wire thickness to maximize the transmission coefficient for the entire visible region, as the maximum changes with wavelength. For a SMNG designed for a narrower wavelength band, the thickness could be optimized further for maximum transmission.

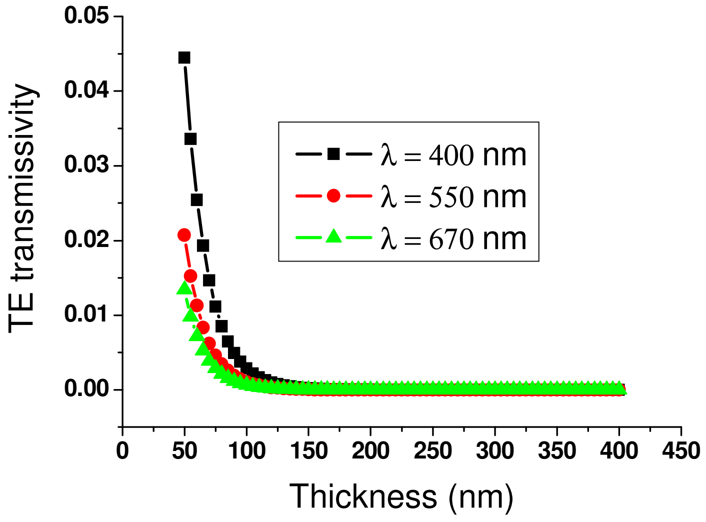

(a)

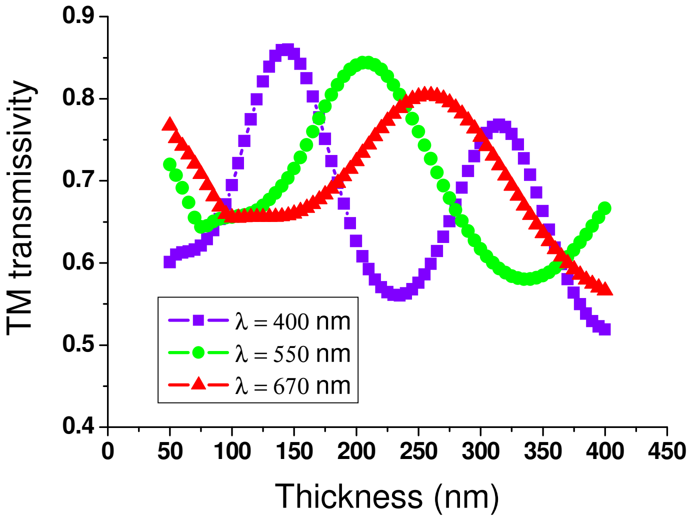

(b)

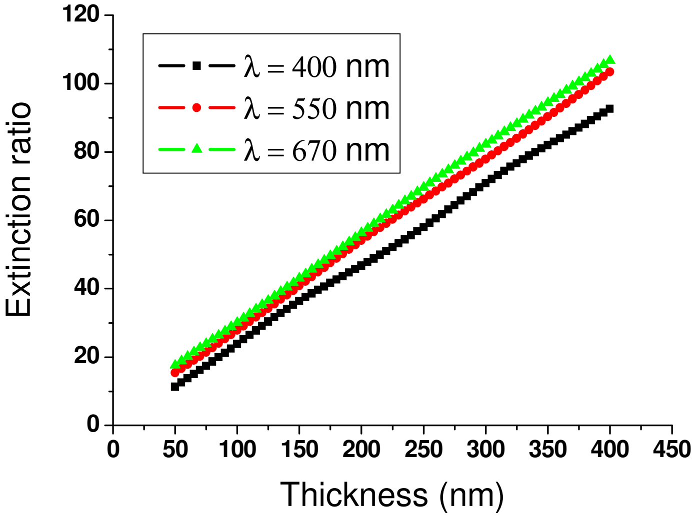

(c)

Figure 4-6 Polarization performance versus grating thickness. The grating period is 150nm, the duty cycle is 50%, and it is at normal incidence. The extinction ratio rises with increasing thickness

4.3.4 Angle of incidence

Finally, we look at the angle of incidence. The angle of incidence is defined as θ in x-z plane shown in Figure 2-3. As can be seen from Figure 4-7, the polarization properties improve with an increase in the angle of incidence of the light. This is due to the increased effective thickness of the grating region with increasing angle of incidence. Because the TE light sees the grating region as an absorbing material, increasing its effective thickness increases the TE attenuation. Similarly, because the TM light sees the grating region as a dielectric material, the increased effective thickness also changes the transmission properties of the gratings in a similar manner to any other thin film. The combination of these two effects leads to the improvements in polarization properties with increasing angle of incidence.

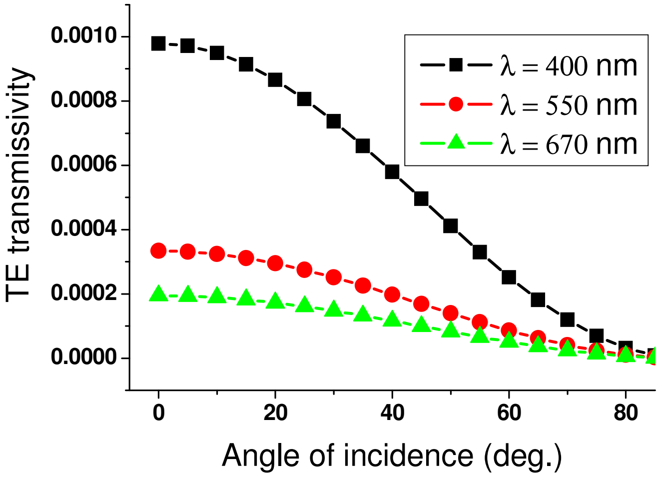

(a)

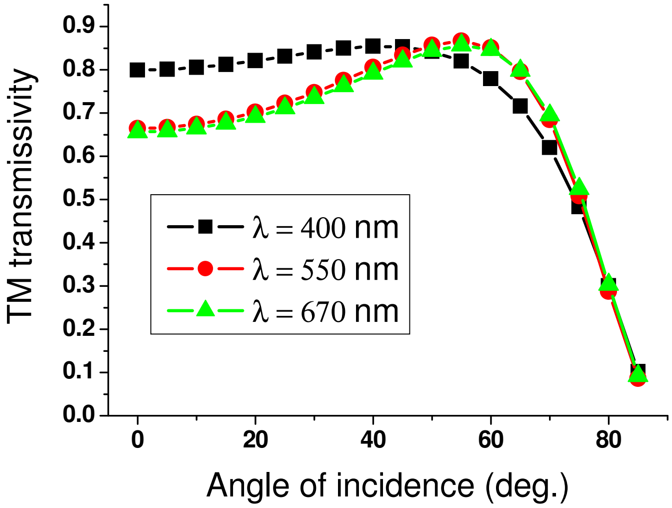

(b)

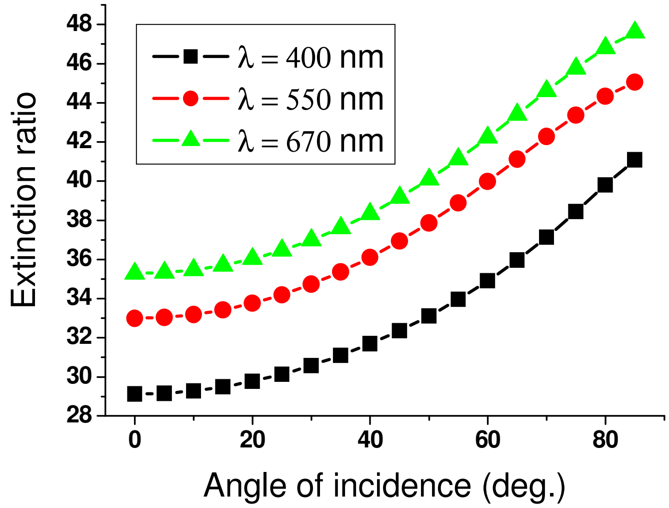

(c)

Figure 4-7 Polarization performance versus angle of incidence. The grating period is 150nm, the duty cycle is 50%, wire thickness is 125nm, and it is at normal incidence. The polarization properties actually improve with increasing angle of incidence θ, up to at least 45 degree, depending on the other parameters.

4.4 Field distribution of light propagating through the grating

While RCWA is good to show the performance of the grating at different wavelengths and to optimize the parameters, we would also like to see the physical process of light propagating through the grating. Thus we use FDTD to simulate the distribution of the electromagnetic field around the grating when light is passing through it.

The SMNG structure used in simulation is periodic along the x-axis and uniform along the z-axis. As shown in Figure 4-8(d), grating period is 150nm, grating height is 200nm and duty cycle is 0.5. Plane wave incidence comes from top of the grating, with wavelength of 550nm. Aluminum is used as the material of grating, with refractive index according to Palik's handbook. Again, we define incident light as TM polarized light if the electric field of incident light is perpendicular to the grating wires, and TE polarized light if the electric field of incident light is parallel to the grating wires. Generally, the intensity of light can be expressed by the sum of the amplitude squares for all electric field components, i.e. $|E|^2 = |E_x|^2+|E_y|^2+|E_z|^2$. For TM incidence, the electric field is in the x-y plane, thus $E_z = 0$. And $E_y = 0$ for normal incidence. For TE incidence, electric field is along z-axis, thus $E_x = E_y = 0$ for both normal and oblique incidence.

Figure 4-8 (a) to (c) show the field distribution for normal incident of TM polarization, where the color bars specify the range of value for field amplitude and intensity. Let's first look at (a) the plot of E_x amplitude. Light incident from the top of the grating, where the amplitude of plane wave is changing periodically. In the grating region, the amplitude reaches maximum since the wave is concentrated insides the slits. Inside the metal grating itself where zero amplitude is shown, light is unable to propagate except for a little penetration at the surface. After light transmits through the grating region, the amplitude changes back to plane wave again, with smaller variation period than the incidence light because the refractive index of substrate shortens the wavelength.

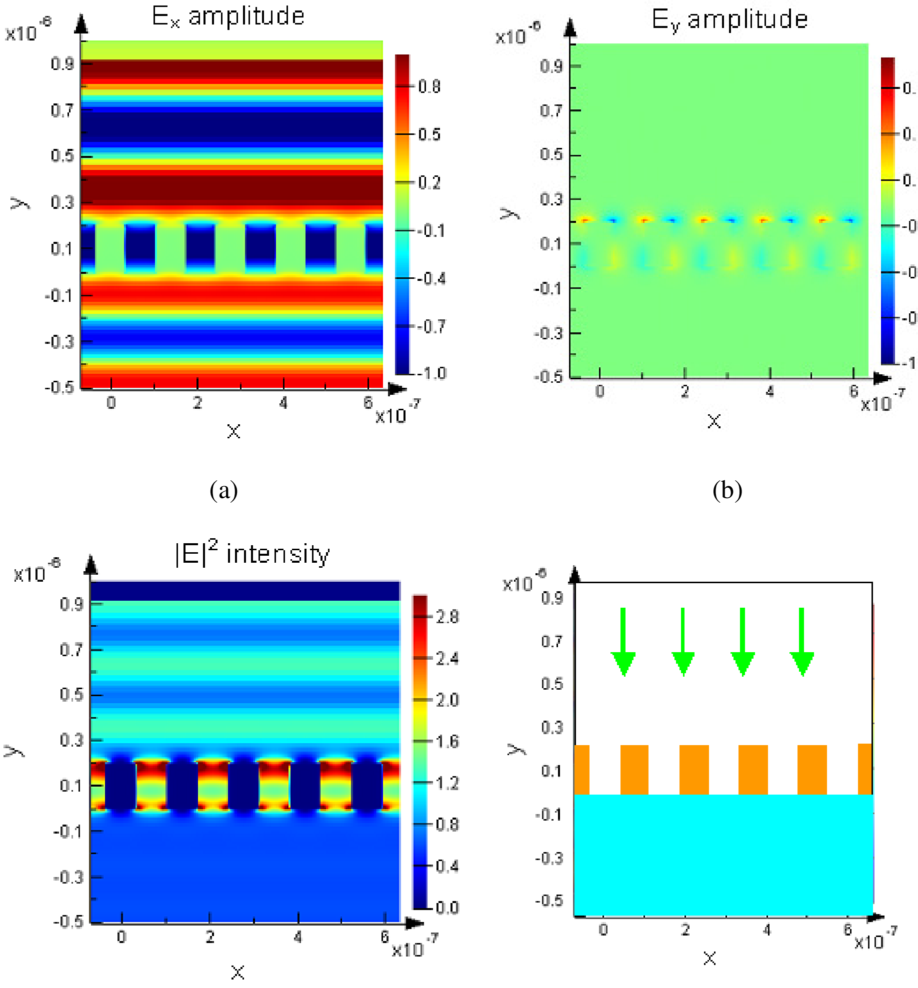

(a) (b)

(c) (d)

Figure 4-8 Field distribution for normal incident of TM polarization from upper region of grating. Grating period is 150nm, grating height is 200nm

Then we move to (b) the plot of Ey amplitude. It is shown Ey equals to zero for both incident and transmitted light, but non-zero in the grating region. The resonance of electrical field tends to drive the electrons on the surface of grating to move along x direction. However, due to the confinement of grating width, which is smaller than the wavelength, the surface electrons are forced to resonance along y direction, which generate radiation with non-zero electrical field along y direction. Since light is transverse wave, thus the propagation of such y component is not supported by the grating slits, which is also parallel along y direction. Thus this y-component vanished and does not exist in the transmitted wave.

Finally we arrive at our conclusion on the $|E|^2$ intensity distribution as shown in (c). Unlike the amplitude plot of (a), the intensity shows a uniform distribution in the region below grating. This is because the definition of intensity averages the time variation of local amplitude at each position within one period, thus the periodic distribution in (a) is vanished. However, we observe a special periodic change of intensity in upper region of grating, where the maximum intensity is even higher than that of initial incidence. This is due to interference of reflected wave and incidence wave. Although the simulation shows 86% of TM is transmitted through the grating, the rest is still reflected by the grating surface except for a tiny amount of absorption. This reflected TM wave would interfere with the incident TM wave since they have same polarization direction. The maximum intensity resulted from this interference of the two wave is reasonably larger than either of them, thus the initial incidence.

After above investigation of TM incidence, we investigate the TE incidence similarly under same condition. Since E_z is the only component contributes to the intensity of TE wave, the plot of E_z amplitude and intensity is shown in Figure 4-9. It shows that a strong interference in the upper region of grating while zero amplitude and intensity in the below region, which suggests most of TE wave is reflected back with zero propagating through the grating. This result shows that the simulated grating structure acts as good polarizer for 550nm wavelength under normal incidence.

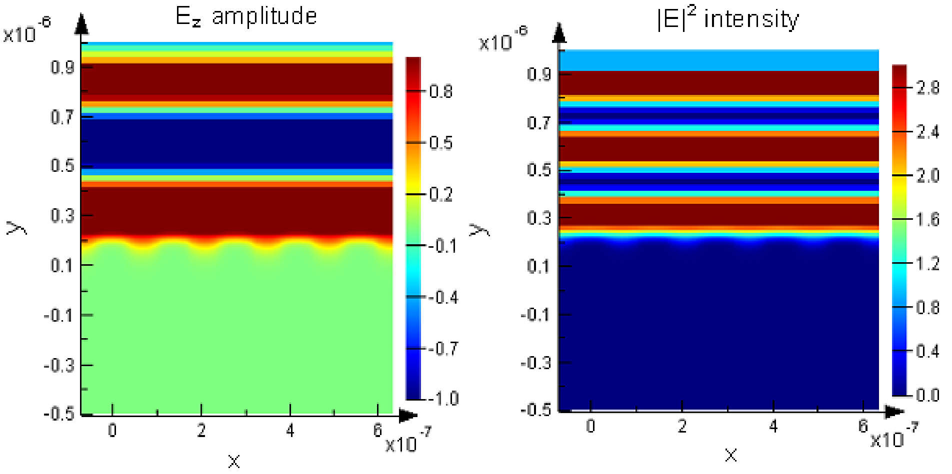

Figure 4-9 Field distribution for normal incident of TE polarization from upper region of grating.

Now we investigate the case of oblique incidence. To get a clearer view on the filed distribution inside the grating slits for oblique incidence, we increase the grating height to 400nm for investigation purpose even through this is not a good value to use based on our previous discussion. An incident angle of 45 degree is used in this simulation and the phase distribution will also be calculated, while the rest parameters are kept the same as Figure 4-8. Figure 4-10 shows the field distribution for oblique incident of TM polarization from upper region of grating, where both E_x and E_y are plotted since both component contribute to the total intensity for oblique incidence. The ripples in the region above the grating result from interference between the incoming light and that reflected from the top surface of the grating. E_x and E_y are same in the upper region, since they are evenly divided component under 45 deg incidence. However, a clear difference is shown inside and blow grating region. This is due to the propagation of such y-component is not supported by the grating slits, as explained in Figure 4-8 (b).

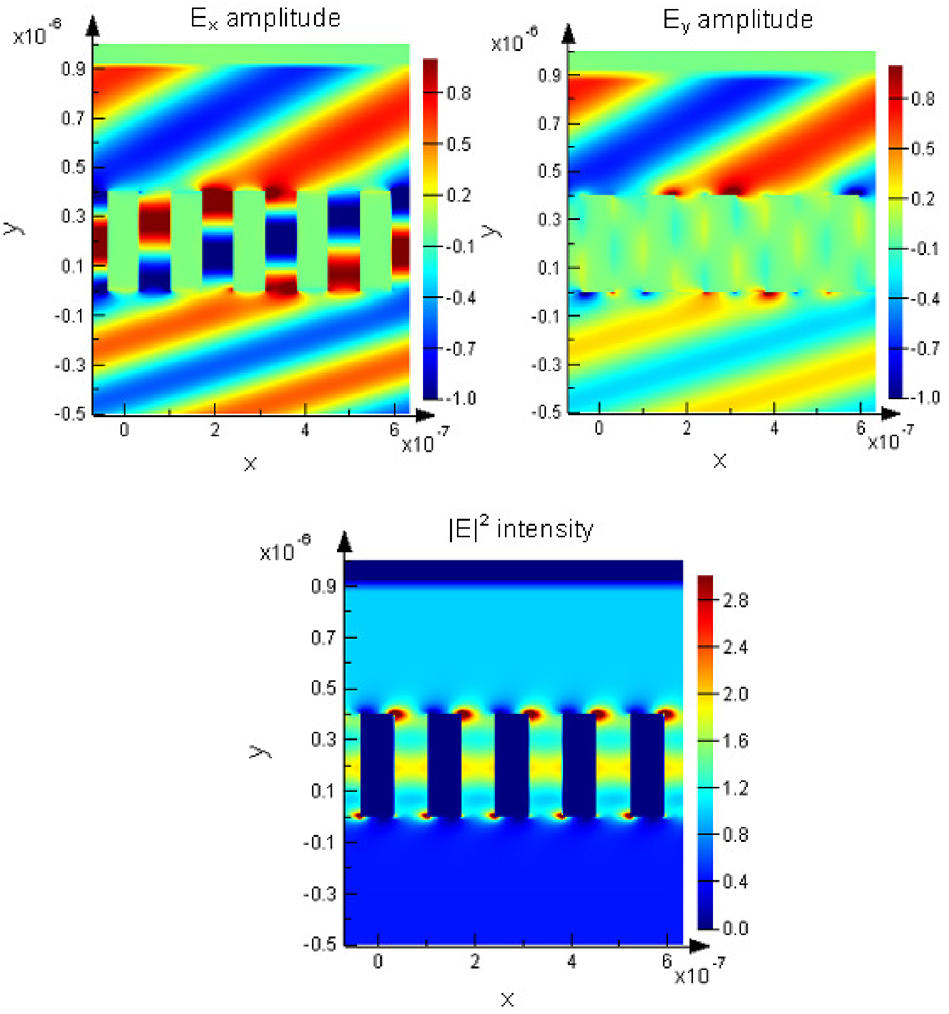

Figure 4-10 Field distribution for oblique incident of TM polarization from upper region of grating.

By combining these two components, the final intensity distribution for oblique incidence is shown in Figure 4-10 (c). The interference is not as strong as in the case of normal incidence, thus there is no clear intensity variation in the upper region of grating. Figure 4-11 shows the phase of the E_x and E_y field components. The change in angle of the wave front results from the higher refractive index of the substrate relative to the air region above the aluminum grating.

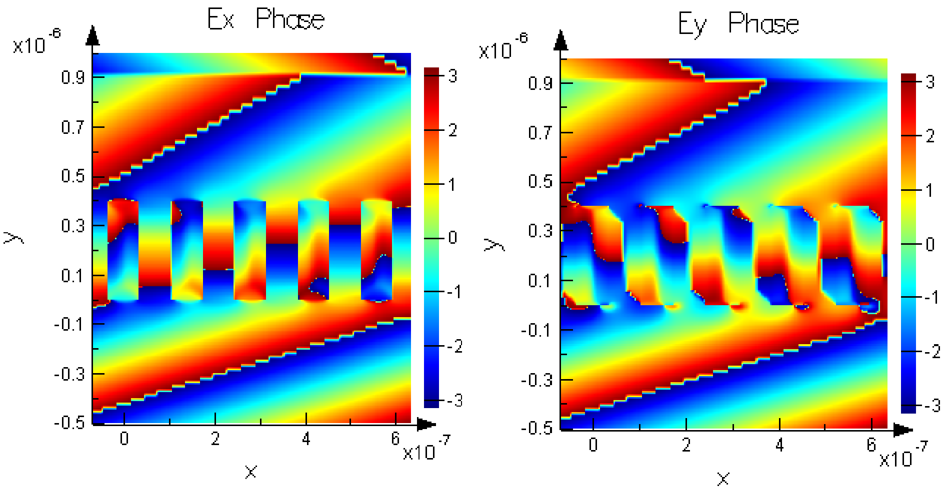

Figure 4-11 Phase distribution of the Ex (left) and Ey (right) field components for oblique incident of TM polarization from upper region of grating.

4.5 Summary

RCWA was used to model the performance of subwavelength grating and design polarized LED. The choice of material to use for visible-wavelength subwavelength metallic grating is discussed, and the effect of the physical parameters on the polarization properties is investigated in details. FDTD was used to simulate the distribution of the electromagnetic field around the grating when light is passing through it.

Chapter 5: Fabrication and Characterization of Polarized Light Emitting Diode

5.1 Introduction

In this chapter we will discuss the experimental work on the polarized LED. The fabrication techniques will be described in detail and process flow and parameters will be given. The fabricated device is electrically pumped and characterized, the EL emission shows high polarization degree. Based on this successful demonstration, we further propose several improved LED structures to meet various application demands.

5.2 Polarized InGaN LED structure

Figure 5-1 shows the schematic diagram of the cross section of the polarized InGaN/GaN green LED structure fabricated in this work [1]. The LED structure is grown on (0001) sapphire substrate by metal organic chemical vapor deposition. The grown epi- layer of 200 nm *p*-GaN layer, four InGaN/GaN quantum wells (QWs) and a 2000 nm thick *n*-GaN form the active region where carrier injection and light emission take place in the LED. The subwavelength metallic nanograting (SMNG) is designed on top of the emitting surface of LED. The restricted movement of electrons in the direction perpendicular to the SMNG gives rise to the polarized light emitting from this device. When the unpolarized emission from QW arrives at the LED surface, for polarization along SMNG, the conduction electrons are coherently driven along SMNG with unrestricted movement and the physical response of SMNG is exactly the same as the case of a thin metal sheet. The resonating electrons give forward radiation, which has exactly opposite phase to the incoming wave, thus the two waves cancel each other and no net propagating wave through the metal. For polarization perpendicular to SMNG, since the period of SMNG is much smaller than the incident wavelength, the electron movement is confined similar to the case of a dielectric. The radiation field generated by electrons is no longer sufficiently strong to cancel the incoming field, thus most of light with this polarization will propagate through the dielectric. So the final output of light emission contains only one polarization.

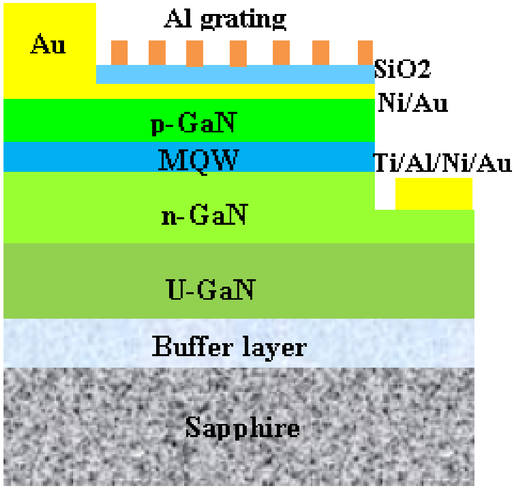

Figure 5-1 Schematic diagram of the cross section of the polarized InGaN/GaN green LED structure fabricated in this work

5.3 Polarized InGaN LED fabrication process

The LED structure is grown on (0001) sapphire substrate by metal organic chemical vapor deposition. The epi layered structure from top has a ~200 nm thick *p*-GaN layer, four InGaN/GaN quantum wells (QWs), ~2000 nm thick *n*-GaN and a ~2000 nm thick *u*-GaN layer. Figure 5-2 shows the fabrication process flow in details.

As described in Figure 5-2, the LED mesa area is about 300 um by 300 um, which is defined by standard photolithographic patterning, using AZ5214 photoresist, spun at 2000 rpm/1sec, 3000 rpm /1sec, 5000 rpm/30 sec with all acceleration of 2000 rpm/sec, achieving ~1.3um thickness. Parts of the *p*-GaN and MQWs were first etched to expose the *n*-type GaN layer and to form a mesa. ICP etching uses 20sccm BCl_3 and 10 sccm Cl_2 under pressure of 5 mTorr at 6 °C. RIE power is 200W and ICP power is 500W. Figure 5-3 is the plot of measured etch depth under different etch time, which indicates a GaN etch rate of ~0.4um/min. The etch rate is stable under above conditions, however, it will be lower if the pattern size of the etch mask is significantly small. Results show that the etch rate will decrease to 0.14 um/min for sub-100nm pattern size.

The 2nd photolithographic patterning was done with alignment to the mesa, then a 10nm/150 nm/10nm/100 nm Ti/Al/Ni/Au metal layers was deposited by electron-beam evaporation followed by lift-off, and then annealed at air ambient at 650 °C to form Ohmic contact for *n*-type GaN. Figure 5-4 shows the plot of deposition rates of different metals using electron-beam evaporation with various process conditions.

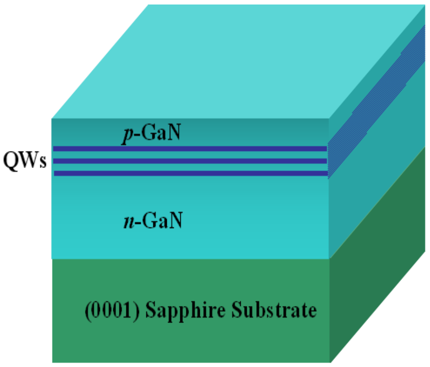

Step 0. Layers grown by MOCVD growth on (0001) sapphire substrate. The layered structure starting from the top is made up of

1) ~200 nm *p*-GaN layer
2) InGaN/GaN QWs
3) ~2000 nm thick *n*-GaN
4) ~2000 nm thick *u*-GaN

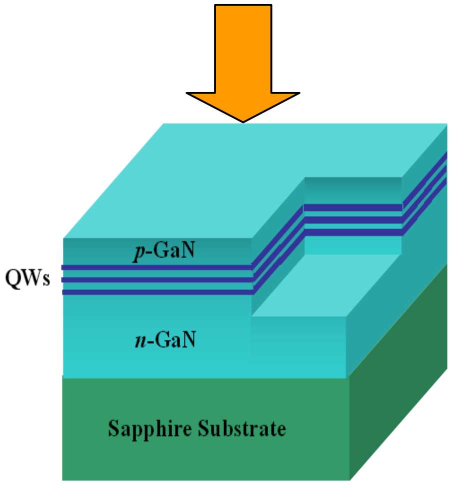

Step 1) Photolithography, using AZ5214 photoresist, spun at 2000rpm for 1sec, 3000rpm for 1sec then 5000rpm for 30sec with all acceleration at 2000rpm/sec, achieving ~1.3um thick resist.

Step 2) Parts of the *p*-GaN and MQWs were first etched to expose the *n*-type GaN layer and to form a mesa.

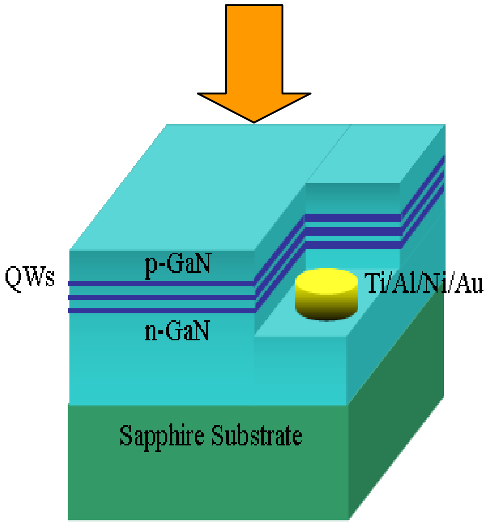

Step 3) The 2nd photolithography was done with alignment to the mesa, which opens a window for n-type contact

Step 4) Electron-beam evaporation of 10nm/150 nm/10nm/100 nm Ti/Al/Ni/Au metal layer

Step 5) Lift-off of Ti/Al/Ni/Au metal layer

Step 6) Annealing at air ambient at 650°C to form n-type Ohmic contact

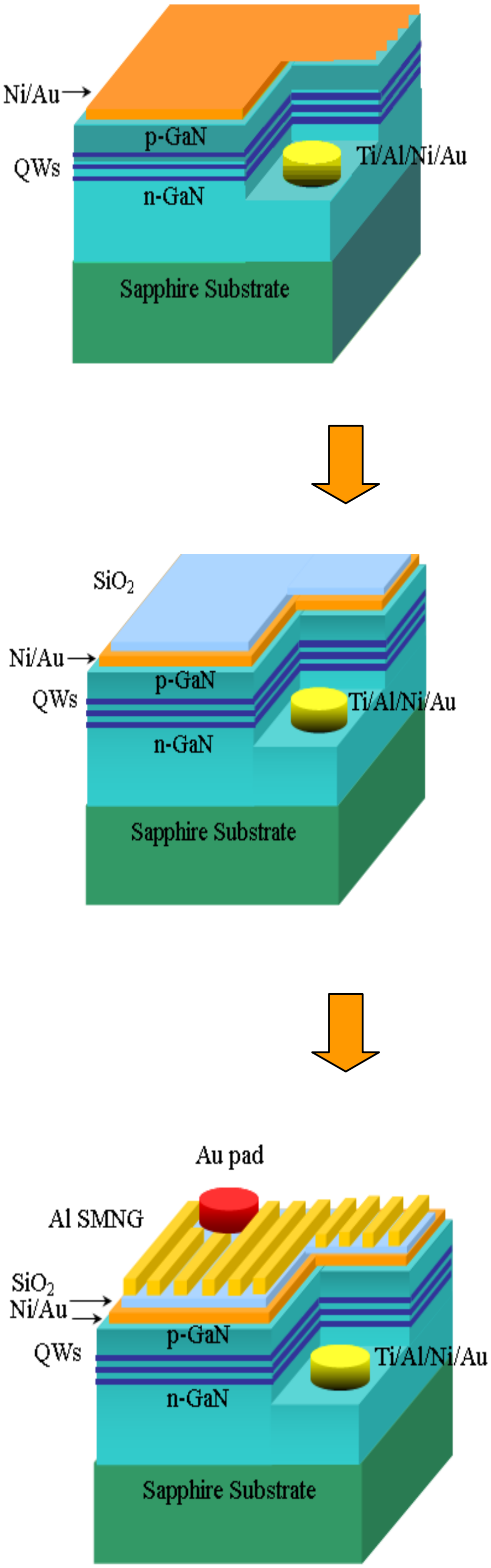

Step 7) The 3rd photolithography step was done on the mesa, to protect the n-GaN region on which the above-mentioned n-type contact is fabricated.

Step 8) Electron-beam evaporation of a 5 nm/5 nm thick Ni/Au metal layer as the current spreading layer for the p-contact.

Step 9) Lift-off of Ni/Au metal layer

Step 10) Annealing at air ambient at 550°C to form ohmic contact to *p*-type GaN.

Step 11) Deposition of SiO_2 layer with thickness of 100nm on top of Ni/Au.

Step 12) The 4th photolithography step was done to the mesa, to open windows for the Au pad

Step 13) Electron beam evaporation and lift-off of 200nm gold to form *p*-pad

Step 14) Deposition of aluminum layer with thickness of 120nm on top of SiO_2.

Step 15) Electron beam lithography was done with alignment to the mesa region, followed by ion-milling to pattern Al SMNG (period = 150nm)

Figure 5-2 Fabrication process flow of polarized InGaN LED (15 steps in total).

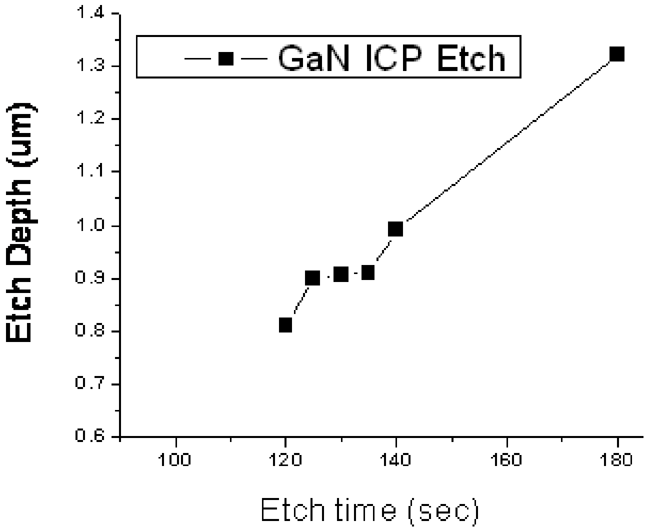

Figure 5-3 Plot of measured GaN ICP etch depth under different etch time, which indicates an etch rate of ~0.4um/min. ICP etching condition is: 20sccm BCl_3 and 10 sccm Cl_2 under pressure of 5 mTorr at 6 °C. RIE power is 200W and ICP power is 500W.

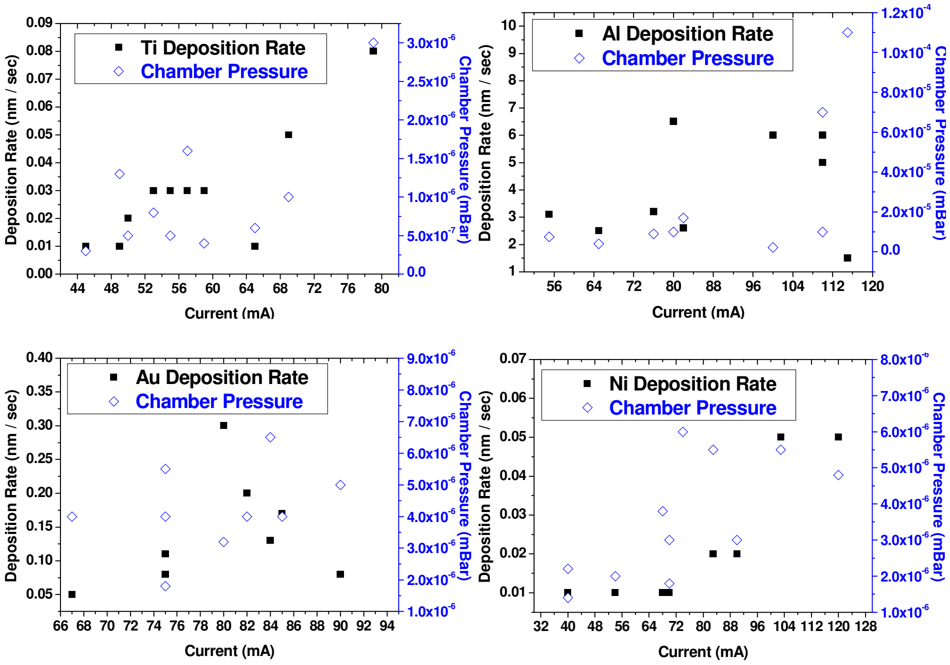

Figure 5-4 Plot of deposition rate of different metals using electron-beam evaporation with various process conditions.

It is noted in Figure 5-4 that both Ti and Ni show increasing deposition rate with increasing current, so as the chamber pressure. This is reasonable because when the e-beam current is increased, the metal source inside crucible heated up by the e-beam is getting higher temperature, thus a higher evaporation rate and deposition rate. Both the increased evaporation flux and increased temperature will increase the chamber pressure. However, such a trend is not obviously seen for Al and Au. The evaporation rate for Al and Au is much higher compared with Ti and Ni, thus a larger variation during the process. This variation adds noise to this diagram, making the relationship not clearly shown from statistic point of view when the sample size (# of evaporation runs) is small.

By repeating a 3rd photolithography step, a 5 nm/5 nm thick Ni/Au metal layer was deposited and annealed at 550°C to form an Ohmic contact to *p*-type GaN. After a 4th photolithography step, ~200nm Au was deposited to form the *p*-bond pad. A thin layer of SiO_2 is deposited by plasma enhanced chemical vapor deposition (PECVD) on top of the Ni/Au 5 nm/5 nm *p*-type Ohmic contact layer. The 5th photolithography step is done to form the *p*-bond pad, where the deposited SiO_2 was removed by etching in buffered HF solution. Aluminum is then evaporated on top of SiO_2 with a thin titanium transition layer to enhance adhesion. ZEP520 resist is mixed with Aniso in the ratio 2:1, then spun onto the sample surface at 3000rpm for 90sec, giving a thickness of ~250nm. The film is then baked on a hotplate at 180°C for 2min to evaporate the solvent. Then a thin layer of carbon particle suspended in water is spun on top of the resist at 1000 rpm for 30 sec, then baked on a hotplate at 95°C for

2min to evaporate the water. The carbon particles left behind forms a conductive coating to conduct away the charges during e-beam writing, which is especially helpful for the non-conductive sapphire substrate used.

Electron beam lithography (EBL) is then performed on ELS-7000 e-beam direct write system with 100 kV acceleration voltage to define accurate 150 nm period grating array on ZEP resist. A field of 300um by 300um is used to covers the whole writing area indicated by the red square shown in the SEM image Figure 5-5. Such a writing strategy gives uniform pattern in large area since no relative movement is needed between gun and stage within one field writing time, thus avoiding any mis-aliment of nanograting pattern which will degrade the polarization effect.

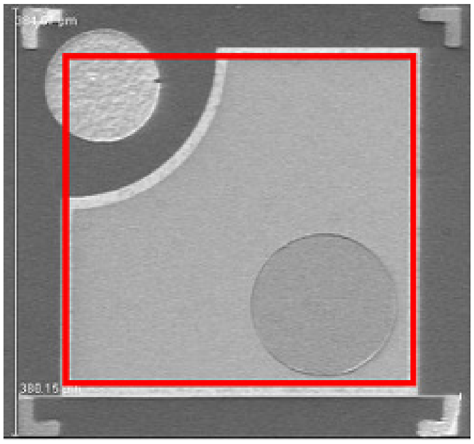

Figure 5-5 E-beam writing field of 300um by 300um indicated by the red square shown under the SEM

After e-beam writing, the sample is rinsed with DI water to clean the carbon conduction layer, and then immersed into oxylene for 30s developing time. The grating pattern was replicated into the underlying aluminum layer through etching process. Figure 5-6 (left) shows that the grating pattern is uniform across the emission region of LED surface [2], while Figure 5-6 (right) shows that the grating pattern is discontinuous around p-pad, leaving a gap where unpolarized emission should come out through the gap. This is because of un-conformal deposition of aluminum around the pad from the shadowing effect during e-beam evaporation and the uneven resist resulted in grating pattern distortion around the pad.

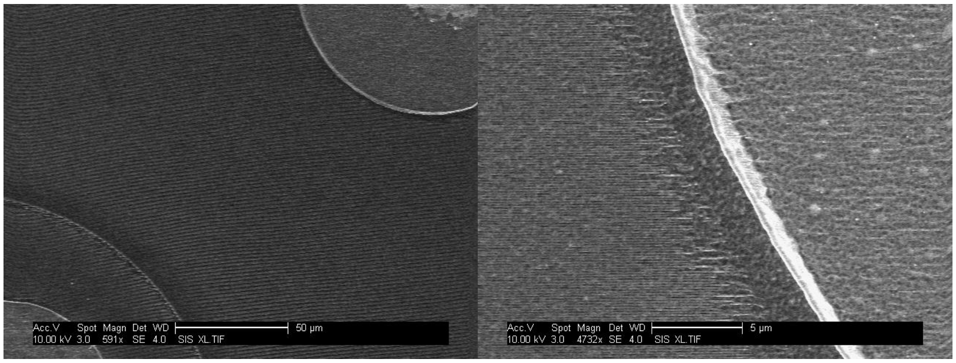

Figure 5-6 SEM image of (left) uniform grating pattern across the emission region of LED surface and (right) discontinuous grating pattern around p-pad.

It is noted that the pre-deposited SiO_2 on top of the Ni/Au 5 nm/5 nm thick *p*-type ohmic contact layer, serves as both a protective layer for *p*-metal contact surface during ion-milling process and as an insulating layer between the metal grating and *p*-contact.

Figure 5-7 (left) shows the optical micrograph of the fabricated SMNG InGaN/GaN LED, where the original LED mesa, defined by optical lithography, is NOT entirely covered by e-beam writing area (The area covered by the SMNG appears darker in shade). We purposely left a margin in the upper and left sides, while increased the coverage in the lower and right side, and also in the area neighboring to the mesa and *n*-contact region. Figure 5-7 (right) shows the scanning electron microscope (SEM) image of the SMNG within the darker square.

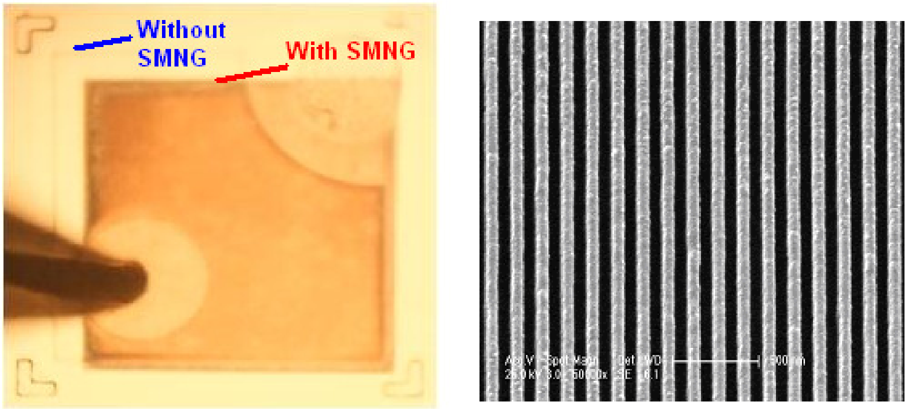

(a) (b)

Figure 5-7 (a) Optical micrograph of fabricated SMNG LED mesa, where the SMNG patterned area appears as darker in shade. (b) Scanning electron microscope image of SMNG with a grating period of 150 nm

To further characterize the surface profile of fabricated Al SMNG, Figure 5-8 shows AFM image of fabricated Al SMNG (upper) and cross section profile (lower). The measured grating period is 150nm, which is consistent with the measurement obtained from SEM. Some discrepancy may exist due to AFM tip used in the measurement not being sharp enough, which prevents the tip from reaching the grating groove. Thus the grating height can not be measured accurately.

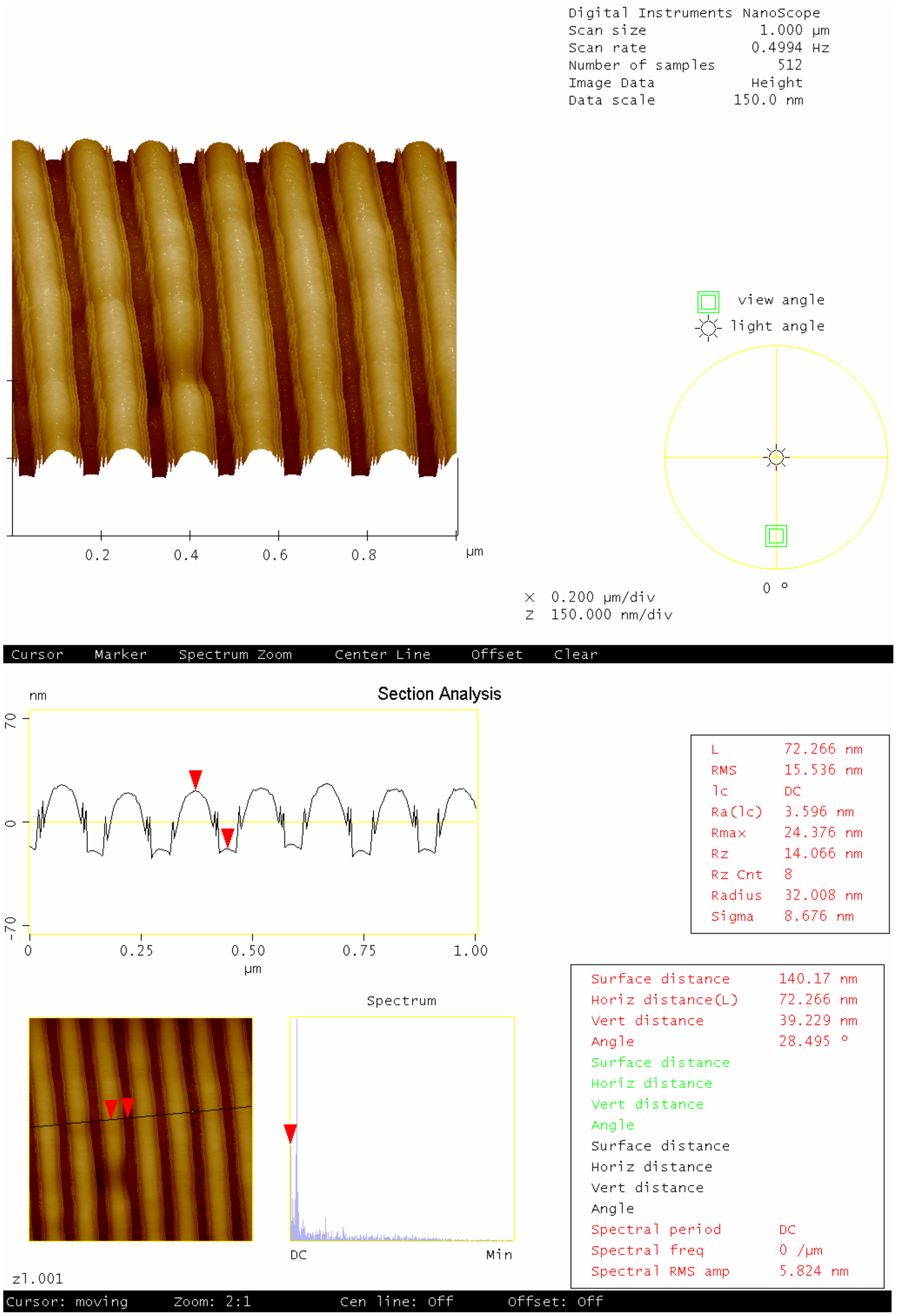

```
Digital Instruments NanoScope
Scan size              1.000 µm
Scan rate             0.4994 Hz
Number of samples        512
Image Data            Height
Data scale          150.0 nm
```

```
X  0.200 µm/div
Z  150.000 nm/div
```

```
L          72.266 nm
RMS        15.536 nm
lc         DC
Ra(lc)     3.596 nm
Rmax       24.376 nm
Rz         14.066 nm
Rz Cnt     8
Radius     32.008 nm
Sigma      8.676 nm
```

```
Surface distance      140.17 nm
Horiz distance(L)     72.266 nm
Vert distance         39.229 nm
Angle                 28.495 °
Surface distance
Horiz distance
Vert distance
Angle
Surface distance
Horiz distance
Vert distance
Angle
Spectral period       DC
Spectral freq         0 /µm
Spectral RMS amp      5.824 nm
```

```
Cursor: moving     Zoom: 2:1        Cen line: Off      Offset: Off
```

Figure 5-8 (a) 3D AFM image of fabricated Al SMNG (b) cross section profile

Figure 5-9 shows the room temperature electroluminescence (EL) spectra of SMNG LED at a forward current of 10 mA [1]. The peak wavelength and the full-width-at-half maximum (FWHM) of the emission spectra of the LED are 546 nm and 80 nm, respectively. Compared with original LED without SWMG fabricated, there was no obvious change for both peak wavelength and FWHM, which is consistent with the fact that our SMNG is designed for giving almost uniform transmission efficiency within this spectral range. It can be seen from the inset optical micrograph that the emission area is exclusively defined by the squared EBL written area where SMNG is patterned. This area is smaller than the mesa area defined by optical lithography as in conventional LEDs. The planar Al layer in the region outside the EBL written area was not etched away during ion-milling as described in the fabrication process flow.

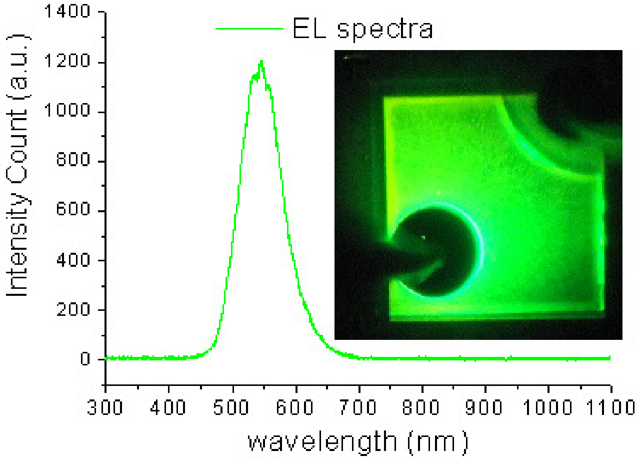

Figure 5-9 Room temperature EL spectra of the InGaN/GaN SMNG LED at a forward injection current of 10 mA, The inset image is the optical micrograph showing the green light emission across the mesa.

Figure 5-10 shows the EL intensity as a function of the orientation angle of the linear polarizer placed between the InGaN/GaN green SMNG LED and the spectrometer [1]. The intensity at various polarizer angles was determined by measuring the peak intensity of the central wavelength of the spectrum in steps of 5-degree intervals. Only the light components with polarization parallel to the polarizer axis will be allowed to pass through the polarizer. The InGaN/GaN green LED before adding on the SMNG showed no polarization and the light intensity is almost constant when turning the polarizer angle in a complete circle. For the LED with the Al SMNG, the measured intensity varies with the polarizer angle, revealing polarized light emission from the LED. The measured polarization ratio, defined as the maximum intensity divided by the minimum intensity I_{max}/I_{min}, is 7:1. The measured results match well with the simulated results using rigorous coupled-wave analysis (RCWA), as seen in the solid curve in Figure 5-10, except around the extinction angle at which the simulated curve almost reach zero for a perfect linear polarization without any orthogonal component. The non-zero orthogonal component in the measured result originated from the leakage light from the P-contact pad edge areas, as seen in the inset optical micrograph of Figure 5-10. The eclipse-like emission suggests that light around the pad has a lower polarization degree possibly because of un-conformal deposition of aluminum around the pad due to the shadowing effect occurring during e-beam evaporation and to the uneven resist resulting in grating pattern distortion around the pad.

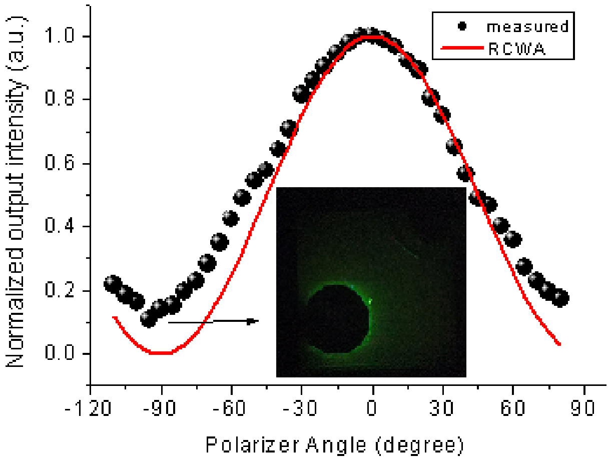

Figure 5-10 EL intensity of the InGaN/GaN SMNG LED as a function of the polarizer angle within one period. Dots are measured at 5-degree intervals while the red curve is simulated by RCWA also with 5-degree intervals but connected as a continuous curve. The inset image shows an optical micrograph of the eclipse like light emission around the p-pad when the polarizer angle is placed at extinction position.

5.4 Summary

In this chapter we have described techniques to make polarized light from a conventional InGaN/GaN LED structure by using a subwavelength metal nanograting (SMNG). The device structures and fabrication methods are compatible to conventional InGaN/GaN LED fabrication. High polarization degree has been demonstrated on fabricated device under electrical pumping.

Chapter 6: Fabrication and characterization of wire-grid polarizer in Terahertz range

6.1 Introduction

In this chapter we apply a similar design idea as that described in the previous chapter to develop polarized emitter in the terahertz (THz) range, which is the last frontier in the electromagnetic spectrum to be explored by human beings. The polarization response of subwavelength metallic grating to terahertz wave is studied systematically. Simulations are performed to study the polarization performance variation with different physical parameters of the grating. Fabrication process is discussed for gold and aluminum grating with period varying from 2 um to 0.5 um based on Si and quartz substrate. Large area grating array with 500nm period is demonstrated by nanoimprint lithography while conventional photolithography was used to define 2um period grating, followed by lift-off or etching method to transfer pattern to metal layer. Characterization was performed by Terahertz time-domain spectroscopy (THz-TDS) and Fourier transform infrared spectroscopy (FTIR) measurement, where a good polarization performance is shown.

6.2 Motivation and design

The least-explored region of the electromagnetic spectrum consists of terahertz waves, which falls between microwaves and infrared light. It has great promise as a security-imaging tool because its frequencies, which range from 300 gigahertz to 3 terahertz, easily pass through clothes but reflect off biological tissue [1, 2]. And since the THz waves do not have the energy that x-rays do, they do not pose a health risk. For years, engineers have had their eyes on terahertz radiation for its ability to capture images as clear as x-rays without the harmful radiation effect. But terahertz applications remain few because scientists have not yet developed all the tools needed to modify and control the waves, one of which is polarization control.

Current commercial THz polarizer is made of ~20 μm wide tungsten wire wound on a circular frame [3]. The fabrication process makes it difficult to have the wire dimension scaled down [4]. In previous chapters, we integrate subwavelength metallic nanograting to InGaN LED. The same design idea can be applied to THz emitter as well. Motivated by this idea, we investigate the polarization performance of subwavelength metallic grating in the terahertz frequency. It was found that the extinction ratio can be greatly enhanced and insertion loss can also be reduced if the grating period could be scaled down to submicron dimension. A THz polarizer with 500nm period grating over a large area of Si substrate is demonstrated by using nanoimprint lithography method.

6.3 Simulation on the physical parameters of grating

The simulation model is same as that used in previous chapters except for the refractive index of material. Since terahertz is the least-explored region of the electromagnetic spectrum, there are few data on the refractive indices of material that we can readily use. Fortunately, the wavelength of THz wave is much larger than the dimension of gratings that we are going to study in this work, and the THz range is far away from the resonance frequency of metals. In this case, the Drude model [6] is applicable to calculate the refractive indices of materials giving results with almost no difference from the experimentally measured data for real materials. So the Drude model will be used through all the simulations in this chapter.

Drude model is a simple analytic index of refraction model based on a simplified physical model of the material which assumes that in a metal one ore more valance electrons per atom were completely delocalized and were free to bounce around inside the metal. The complex index of refraction n_c is defined as

$$n_c^2 = (n + ik)^2 \equiv \varepsilon_c = \varepsilon_1 + i\varepsilon_2$$

The Drude model dielectric function is

$$\varepsilon_c = \varepsilon_\infty - \frac{\omega_p^2}{\omega^2 + i\omega\omega_\tau}$$

Separating the real and imaginary parts yields

$$\varepsilon_1 = \varepsilon_\infty - \frac{\omega_p^2}{\omega^2 + \omega_\tau^2},$$

$$\varepsilon_2 = \frac{\omega_p^2 \omega_\tau}{\omega^3 + \omega\omega_\tau^2}.$$

In these equations, the plasma frequency is

$$\omega_p\left(cm^{-1}\right) = \frac{1}{2\pi c}\left(\frac{4\pi Ne^2}{m^* \varepsilon_\infty}\right)^{1/2}$$

Where N is the free electron density, e is the electron charge, m* is the effective mass of the electrons. ε_∞ is the high frequency dielectric constant. ω_τ is the damping frequency known for each metals. By inputting the frequency value, the refractive index at each frequency could be calculated.

Grating period is a key factor that determines the performances of wire-grid polarizer. One most important design goal for a wire-grid polarizer is to achieve as higher extinction ratio and lower insertion loss as possible. The former indicates the purity of polarized light obtained and the latter indicates the efficiency as defined in Equ 2.4. Figure 6-1 shows the simulation results of extinction ratio and insertion loss of Al wire-grid polarizer as a function of terahertz frequencies. The parameters for two Al gratings are of thickness ~120nm, duty cycle ~50%, period of 500nm and 3 um. The complex refractive index of Al was derived from the Drude model. Here, we defined the extinction ratio as –10log (T_{TE}/T_{TM}), and the insertion loss as 10log ($1/T_{TM}$). It is noted that the extinction ratio is greatly enhanced and the insertion loss is greatly reduced over the frequency range 0.5-5 THz when the grating period is scaled down from 3 um to 500 nm. As is known, 3um is a critical value close to the feature size limit to be fabricated by conventional masking photolithography. To take full advantage of the enhanced wire grid polarizer performance when the period is scaled down to 500 nm, other lithography techniques should be applied.

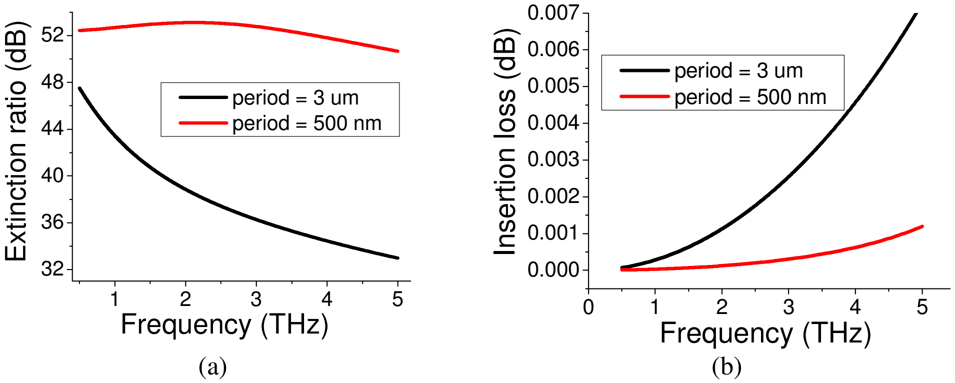

(a) (b)

Figure 6-1 Simulation results of (a) extinction ratio and (b) insertion loss of Al wire-grid polarizer with period of 500 nm and 3 um as a function of terahertz frequencies under normal incidence. Al thickness used in this simulation is 120nm.

For large area sub-micron patterning, NIL is a promising technology and wafer level nano-patterning has been demonstrated. A polarizer made from Al grating on Si substrate was demonstrated in this chapter using NIL and the wet chemical etching.

It is known that highly doped Si with low resistivity causes strong absorption in the THz range but intrinsic Si has very low absorption [7]. The substrate used in this work is intrinsic Si (100) wafer with resistivity above 18,000 Ωcm and thickness of 500 um, which provides sufficient chemical stability, thermal durability, high robustness and very low absorption.

Figure 6-2 shows the simulation results of TE and TM transmittances as a function of THz frequencies for the Al grating at normal incidence. The parameters for the Al grating are same as that used in Figure 6-1 and the period is 500nm. The refractive index of Si, treated as lossless and dispersionless, was selected as 3.4 [7]. It is noted that the TM transmittance is around 50% while the TE transmittance is below 0.02% in the frequency range up to 5 THz. This can result an extinction ratio of 35 dB at 5 THz and >35dB below 5 THz. It is noted that we have included Si substrate into this simulation to show the performance of the whole device. The value of 50% is very close to the well-known transmittance of a dielectric sheet in air, when its refractive index is 3.4. This suggests that the TM transmittance is almost 100% if we purely consider the Al grating without Si substrate, which is true as verified by further simulation on free standing Al grating in air. This conclusion is also consistent with the FDTD result, as shown in following sections.

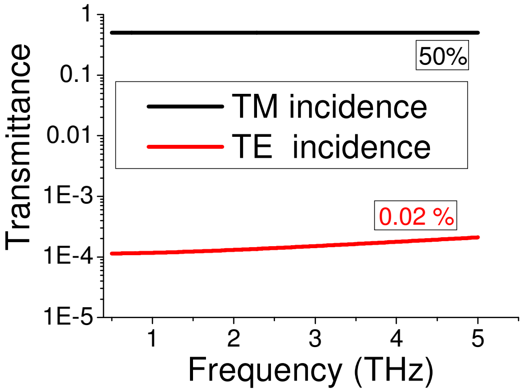

Figure 6-2 Simulation results of TE and TM transmittances at normal incident angle as a function of terahertz frequencies.

Figure 6-3 shows FDTD simulation on the transmittance of TM wave and extinction ratio in 0~5 THz region with different metal thicknesses, while the duty cycle and grating period were fixed at 50% and 500nm, respectively. It is found that TM transmittance is lower with increasing metal thickness and that the TM transmittance decreases faster with frequency for larger metal thickness. The extinction ratio increases by more than 30 dB when the metal thickness varies from 200 nm to 600 nm. This is reasonable because as the thickness of the metal is increased, the TE transmission is reduced. Since the TE wave sees the grating region as an absorbing film, increasing the grating thickness increases its absorption. Since TM transmittance always stays at a high value of above 98%, the variation of extinction ratio shown in Figure 6-3 (b) is the result of the variation of TE transmission. It is observed in Figure 6-3 (b) an increasing variation in extinction ratio with increasing metal thickness, which indicates an increasing variation of TE transmission with increasing metal height. Also the variation period decrease with increasing metal height. We suspect that this variation is due to the Fabry-Perot cavity effect. It is noted that the wavelength of THz wave is much larger than the cavity length, namely the metal thickness here. So a larger cavity length means a larger phase difference between the TE waves reflected at the top and the TE wave reflected at the bottom of the cavity, thus a larger variation in the total TE transmission as the result of interference between these two phases. Since the TE transmission is very small, this difference in TE transmission makes a considerably large contribution to the variation, which is further amplified through the calculation of extinction ratio as defined by (2.4).

It is noticed that for the purpose of investigating the physical mechanism solely from the grating effect, this simulation does not include the substrate effect. The effect of substrate will be considered later.

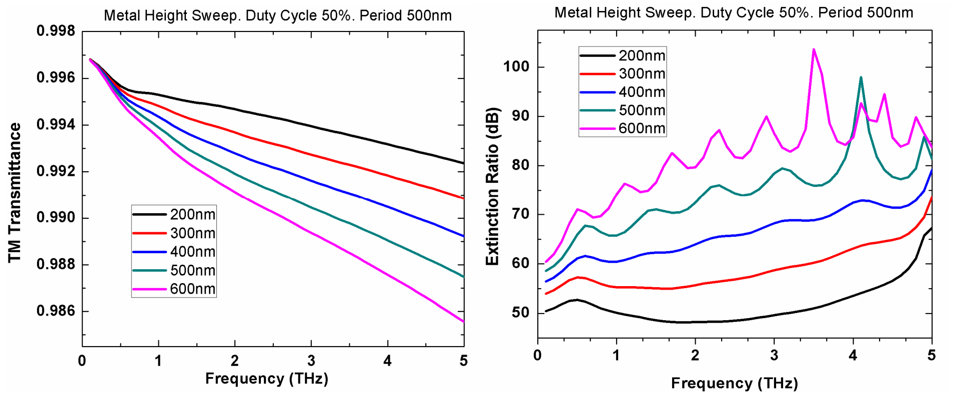

(a) (b)

Figure 6-3 FDTD simulation on (a) transmittance of TM wave and (b) extinction ratio in 0~5 THz region with different metal thicknesses, while the duty cycle and grating period were fixed at 50% and 500nm, respectively.

Figure 6.4 shows the FDTD simulation on the transmittance of TM wave and extinction ratio in the 0~5 THz region with different grating period, while the duty cycle and metal thickness were fixed at 50% and 500nm, respectively. It is found that the TM transmittance decreases with increasing frequency while the different period does not give a significant difference to TM transmittance. This is reasonable because as the frequency is increased thus the wavelength is shorter, the wires become equivalently wider for TM field therefore the electrons have more space in which they can vibrate. This results in an increase in the attenuation of the TM wave. It is also found that the smaller period gives higher extinction ratio. This is mainly due to the reduced period resulting an increased attenuation of the TE wave, which was explained in chapter 4. Since we have already shown that different period does not give a significant difference to TM transmittance, the smaller period results in higher extinction ratio simply due to smaller TE transmission.

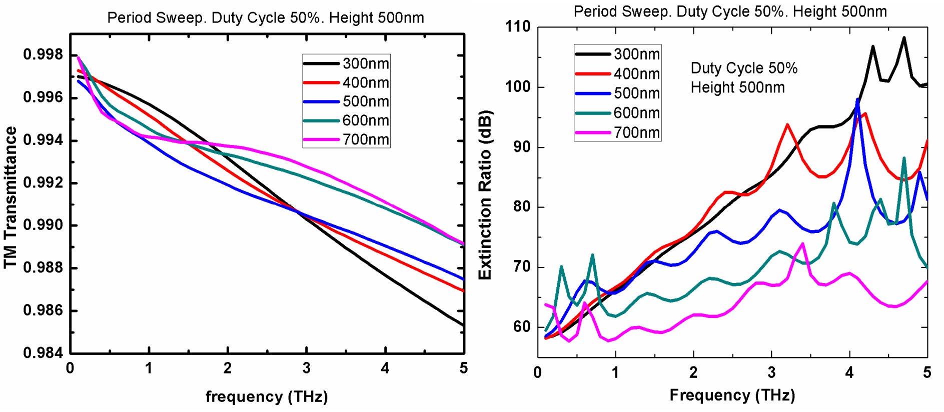

(a) (b)

Figure 6-4 FDTD simulation on (a) transmittance of TM wave and (b) extinction ratio in 0~5 THz region with different grating period, while the duty cycle and metal thickness were fixed at 50% and 500nm, respectively.

Figure 6.5 shows the FDTD simulation on the transmittance of TM wave and extinction ratio in 0~5 THz region with different duty cycle, while both the grating period and metal thickness were each fixed at 500nm. It is found that the TM transmittance decreases with increase in duty cycle while the extinction ratio will increase. This behavior is similar to that described in Figure 4.5 (b) and (c). The difference lies in that the wavelength of THz wave is much larger compared with visible light and the grating period. So even though a larger duty cycle gives more space for electrons to move perpendicular to the grating under excitation of TM wave, the grating width is still so small compared to the wavelength that the attenuation in TM wave is also smaller. Similarly, since the wires are too close together compared with THz wave, it is extremely easy for the TE field to excite the electrons to move along the wires. This results in an increase in the attenuation of the TE wave so the transmission of TE wave is several magnitude smaller compared with the case in visible range. Therefore the extinction ratio is much larger than that is shown in Figure 4.6 (c).

After performing the analysis focusing on the grating itself, we investigate the effect of substrate. As shown in Figure 6-6, Si with a high resistivity and a refractive index 3.4 was chosen as substrate. The extinction ratio is around 51 dB when substrate thickness is zero, this is consistent with the result shown in Figure 6-3 (b). The extinction ratio then decreases with thicker substrate. Since the two interfaces of the Si can also form a FP cavity, the constructive or destructive interference at different thicknesses will also influence the extinction ratio. So substrate with a smaller thickness (<0.1 um) is desired from a simulation point of view, but a reasonable thickness is required to provide enough physical support for the gratings during fabrication.

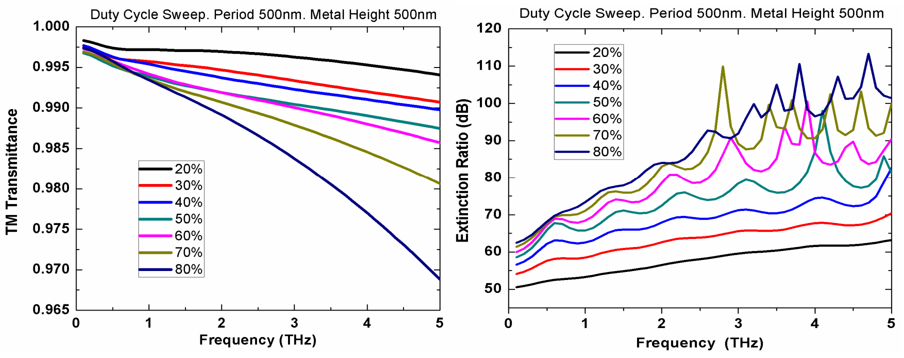

(a) (b)

Figure 6-5 FDTD simulation on (a) transmittance of TM wave and (b) extinction ratio in 0~5T THz region with different duty cycle, while both the grating period and metal thickness were fixed at 500nm.

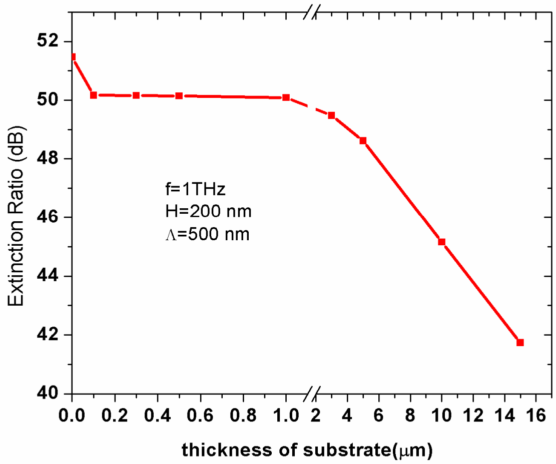

Figure 6-6 FDTD simulation on extinction ratio at 1 THz with different thickness of substrate. Metal thickness is 200 nm and grating period is 500nm.

6.4 Fabrication of grating

The process flow for the grating fabrication is shown in Figure 6-7. After a piranha clean (H_2SO_4: H_2O_2 = 3:1), an aluminum layer with thickness of 120 nm was deposited on the Si wafer by electron beam evaporation. Then the sample is spin-coated with PMMA of molecular weight 120K at 1500 rpm to achieve a thickness of about 300nm.

A (1H,1H,2H,2H)-Perfluorodecyltrichloro mold with 500nm is placed on top of the wafer and imprinted in Obducat Nanoimprinter at 150^0C and 60 bar for 300s. The residual layer after the imprint has the thickness of about 60nm, which is then removed by O_2 plasma etching. Then the sample was immersed into the mixture of H_3PO_4: H_2O_2: H_2O (8:1:1) for wet etching of aluminum, the etching rate is 10nm/sec at 35 ^{o}C. Finally the sample is rinsed with acetone to remove all remaining PMMA. Figure 6.8 shows a scanning electron microscopy image of the fabricated element with grating period of 500 nm and duty cycle of 0.5.

Besides the 500nm period grating described above fabricated by nanoimprint lithograohy, conventional photolithography was used to fabricate 2um period grating on photoresist, as shown in Figure 6-9 (a) (microscope image of 2um photoresist grating). Then 10 nm Cr was deposited by ebeam evaporation as adhesion layer followed by 200nm Au.

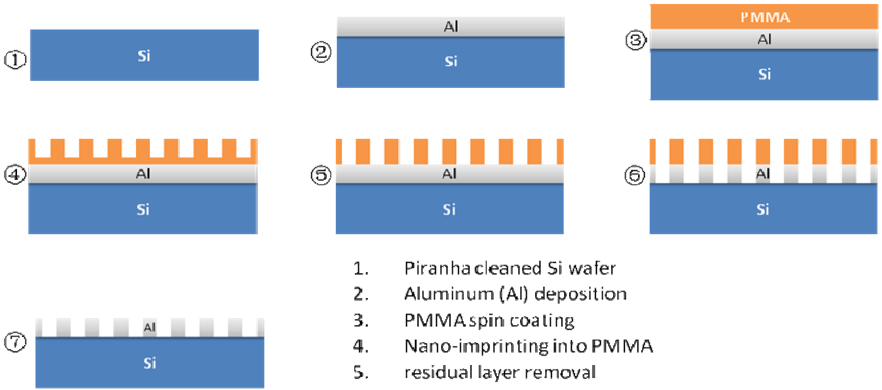

1. Piranha cleaned Si wafer
2. Aluminum (Al) deposition
3. PMMA spin coating
4. Nano-imprinting into PMMA
5. residual layer removal
6. Pattern transfer into Aluminum
7. Removal of PMMA

Figure 6-7 Process flow for the grating fabrication

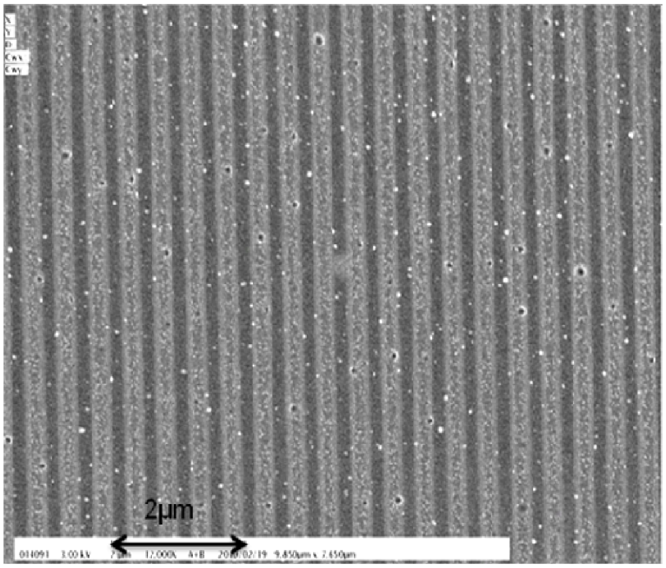

Figure 6-8 SEM image of the fabricated wire-grid polarizer with a period of 500nm

The sample was immersed in acetone to lift off the Au on top of photoresist, leaving the Au grating inside the groove, as indicated in Figure 6-10. The final Au grating with period of 2um after lift-off is shown in Figure 6-9 (b).

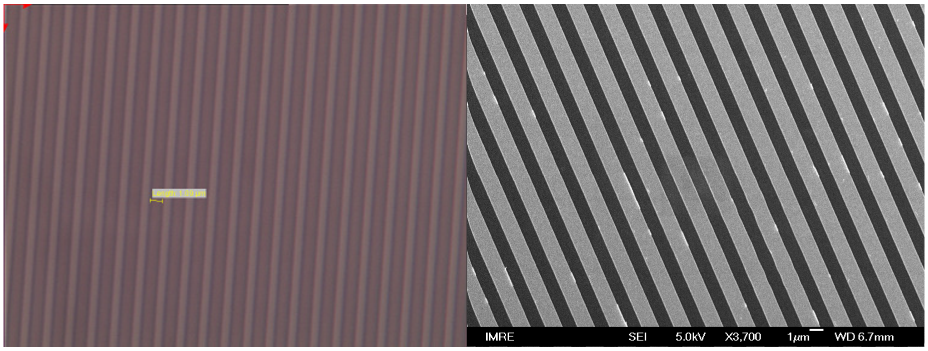

Figure 6-9 (a) Grating on photoresist with 2um period defined by conventional photolithography. The sample is exposed under UV light for 700 mw/cm2 for 10 sec and then developed with diluted developer (1:1 with DI water) for 12sec. (b) SEM image of Au grating with period of 2um after lift-off

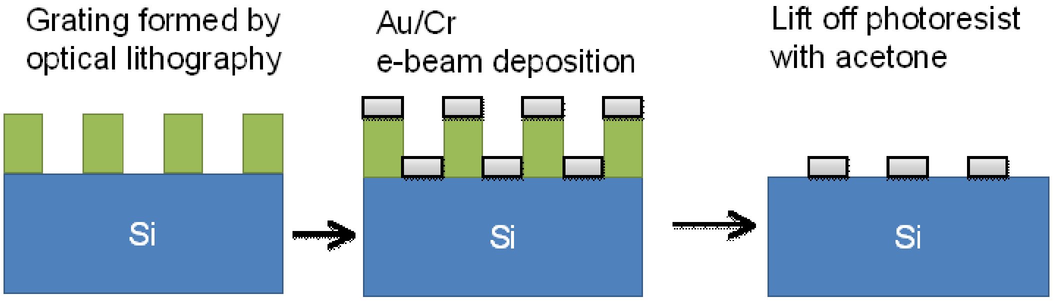

Figure 6-10 Lift-off process of Au grating with 2um period. The substrate could be Si or quartz.

6.5 Characterization

The fabricated sample is characterized by Fourier Transform Infrared Spectrometry (FTIR) and Terahertz time-domain spectroscopy (THz-TDS) measurement. In the FTIR measurement, both air and bare Si substrate are chosen as background reference.

The THz transmission spectrum of the fabricated element was measured by using a FTIR in a frequency range of 0.5-5 THz. Figure 6-11 shows the transmission spectra of the fabricated element for TM and TE polarizations at normal incidence, as well as that of a bare Si substrate without the wire grid to be use for comparison. Preliminary results show that the TM transmission is very close to the reference Si substrate transmission line, except for the abnormal peaks at around 1.7 THz and 3.6 THz. We have taken re-scan for several time and got this abnormal peak repeatedly. These abnormal peaks are caused by the error of our FTIR measuring system, which is confirmed by THz-TDS measurement shown later. It also shown in Figure 6-11 that TE transmission gets larger when the wavelength is reduced. This suggests the existence of etch defects on wire grid, uneven distribution of Al density along the wire grid, surface roughness and oxidation resulted from wet etch process. At low frequency, since the grating structure is so smaller compared with wavelength, these defects are not recognized by the incidence wave with long wavelength. However, when the wavelength gets reduced, these defects could be identified and result in higher transmission of TE polarization. These defects could be eliminated by optimization of the device processing such as changing the wet etch process to lift-off or dry etch process, thus the performance could be further improved by having a lower TE transmission and a high extinction ratio. The technique described for the fabrication of a THz polarizer grating is low in cost and has high throughput.

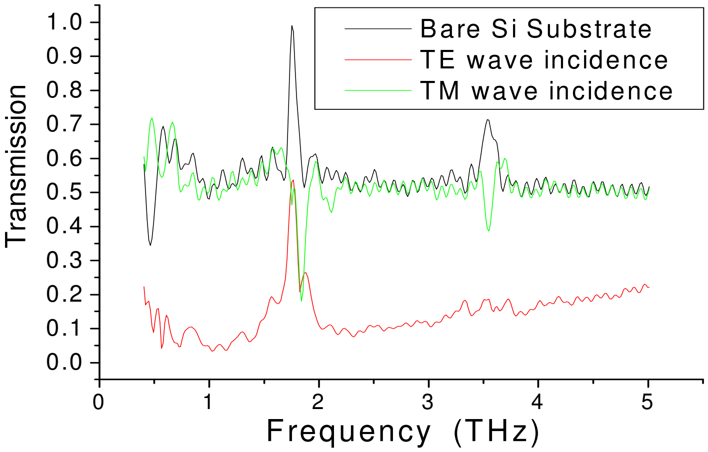

Figure 6-11 Measured THz spectrum using FTIR for the fabricated wire-grid polarizer with a period of 500nm by nanoimprint lithography and wet etching process

Figure 6-12 shows the measured THz spectrum by FTIR for the fabricated wire-grid polarizer with a period of 2um by photolithography and lift-off process. Grating of 200nm Au, 2um period and 50% duty cycle on 300um quartz was also characterized. It is shown that the TM transmission is also close to the reference Si substrate transmission. The TE transmission is closed to zero even at high frequency, which is an improvement in the grating performance compared with Figure 6-11. It is also confirmed that the increasing TE transmission in Figure 6-11 is due to wet-etch defect which could be eliminated by changing the wet etch process to lift-off.

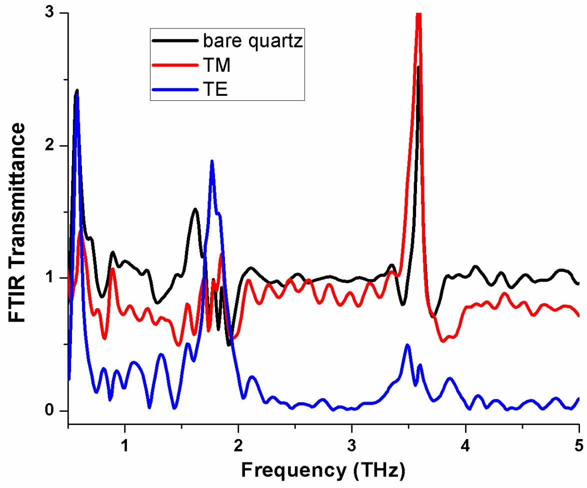

Figure 6-12 Measured THz spectrum using FTIR for the fabricated wire-grid polarizer with a period of 2um by photolithography and lift-off process.

The fabricated sample was also characterized by THz Time Domain Spectrometry (THz-TDS). It is showed in Figure 6-13 (a) that the signal of TM is exactly the same as bare Si. The signal of TE is much smaller since most of the TE wave is reflected by the grating and the transmitted intensity is very low, this is also confirmed by FTIR measurement. The frequency response of the sample to TE and TM wave is extracted by performing Fourier transformation, as shown in Figure 6-13 (b). The corresponding extinction ratio spectrum is shown in Figure 6-13 (c), where average extinction ratio above 25dB in 0.6~3THz. The fringes are formed by constructive or destructive interference.

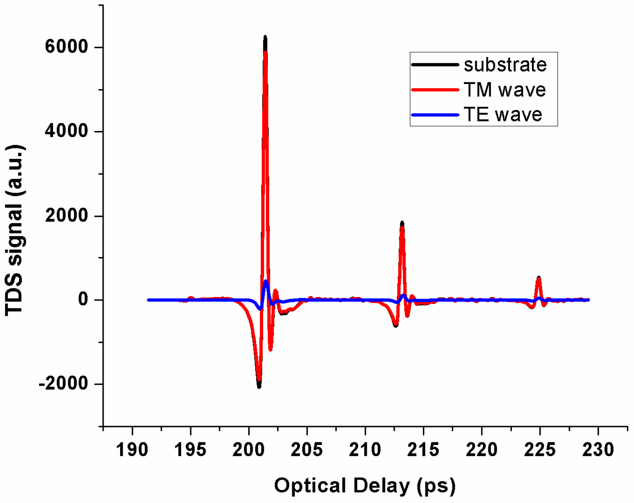

TDS signal (a.u.)
6000
4000
2000
0
-2000
substrate
TM wave
TE wave
190
195
200
205
210
215
220
225
230
Optical Delay (ps)

(a)

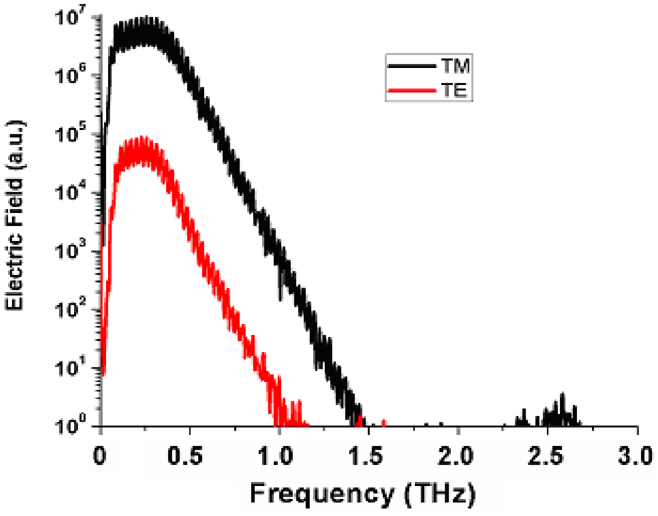

Electric Field (a.u.)
10^7
10^6
10^5
10^4
10^3
10^2
10^1
10^0
TM
TE
0
0.5
1.0
1.5
2.0
2.5
3.0
Frequency (THz)

(b)

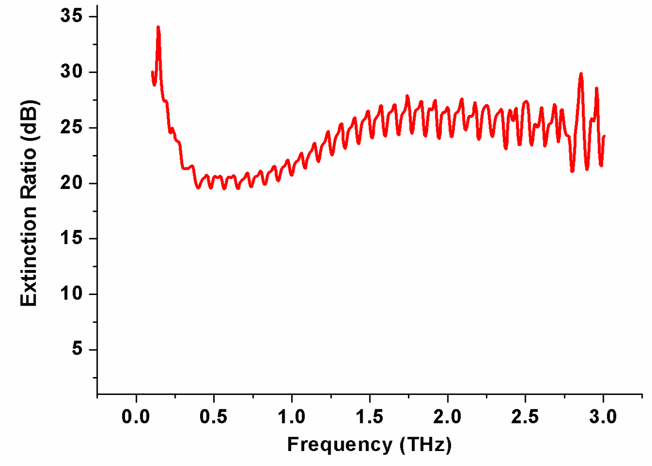

(c)

Figure 6-13 (a) THz-TDs testing raw data showing that signal of TM is exactly the same as bare Si and the signal of TE is much smaller than TM. (b) The frequency response of the sample to TE and TM wave extracted by performing Fourier transformation. (c) The corresponding extinction ratio spectrum

6.6 Summary

In this chapter we have systematically studied the polarization response of subwavelength metallic grating to terahertz wave. Simulations are performed to study the polarization performance variation with different physical parameters of the grating. Fabrication process is discussed for gold and aluminum grating with period varying from 2 um to 0.5 um based on Si and quartz substrate. Characterization was performed by Terahertz time-domain spectroscopy (THz-TDS) and Fourier transform infrared spectroscopy (FTIR) measurement.

Chapter 7: Summary and Future Work

7.1 Summary

The work described in this thesis is summarized as follows.

We have used RCWA to model the performance of SMNG. The choice of material to use for visible-wavelength SMNG is discussed, and the effect of the physical parameters on the polarization properties is investigated in details. FDTD was used to simulate the distribution of the electromagnetic field around the grating when light is passing through it. These investigations show a promising design of polarized InGaN LED by using SMNG.

We have developed the process flow to make polarized InGaN LED by integrating SMNG on the emitting surface of InGaN LED. Both device structures and fabrication methods are compatible to conventional InGaN/GaN LED fabrication. The process parameters for photolithography, e-beam lithography, nanoimprint lithography, e-beam evaporation, plasma etching and ion milling are studied and optimized.

Based on above structure design and process development, a linearly polarized surface emitting InGaN/GaN LED on sapphire substrate was demonstrated, with a polarization ratio of 7:1 (~88% polarization of light) for electroluminescence emission from the device under electrical pumping. This value is the highest ever reported among those achieved by other methods such as from LEDs grown on non-polar/semi-polar surface, LEDs with backside reflector or those incorporating photonic crystal.

The polarization response of SMNG to terahertz wave is also studied.

7.2 Future work

The above experimental result serves as experimental demonstration of polarized InGaN surface emitting LED. Simulation results presented in chapter 4 showed that the polarization ratio and the light output efficiency are related to the grating parameters, such as grating period, grating height and duty cycle. The grating parameters can be tuned to obtain desired polarization performance. The device size can be smaller or bigger than the current device used in the experiment and the p-mesa shape can be different. We propose several improved LED structures with different designs to meet various application demands.

One alternative LED structure with polarized emission is to make the SMNG directly on top of the p-GaN layer serving as the top electrode [1]. Figure 7-1 shows schematic diagram of a polarized LED with SMNG in cross section view and top view. In this method, the SMNG will be serving as both polarizer and the metal contact to the p-GaN, like a transparent conducting electrode. To get better ohmic contact as well as polarizer function, the grating can be formed by Ni/Au/Al with thickness of 5nm/5nm/150nm. The p-metal contact pad is modified to have all the grating lines connected. This structure will save the steps of separate Ni/Au and Al metal deposition, and the PECVD SiO_2 deposition. Alternatively, the Ni/Au 5nm/5nm thin contact layer can be kept as a continuous film and the Al sub-wavelength grating is formed directly on top of the Ni/Au contact without the SiO_2 insulation layer. In this case, the SMNG should be made within the p-contact layer to avoid any potential electrical short circuit to the n-GaN.

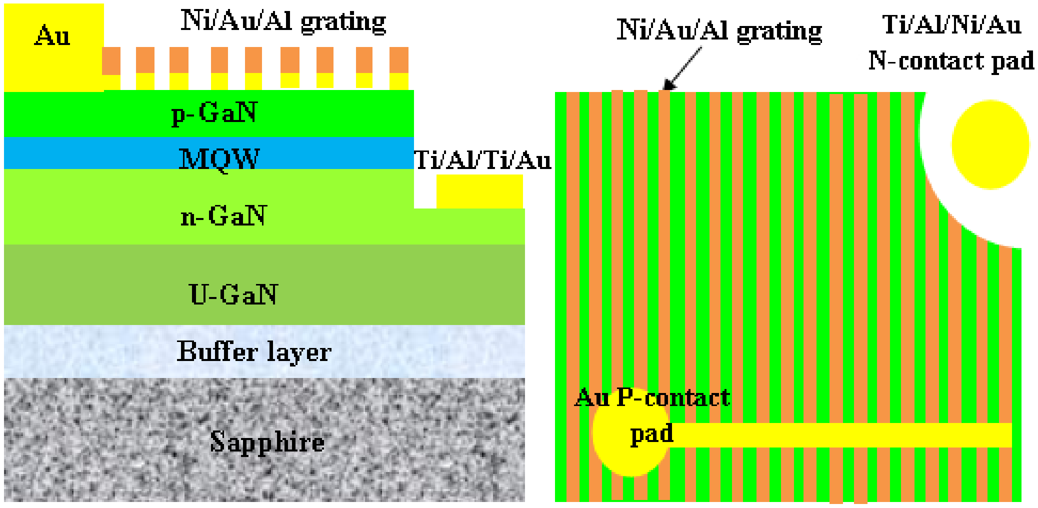

Figure 7-1 Cross section view (left) and top view (right) of the polarized LED with SMNG directly on top of the p-GaN layer

Before packaging, the LED wafer is diced into individual chips. Due to the higher refractive index of the InGaN and GaN layers with respect to that of sapphire, the InGaN/GaN layer on top of the sapphire substrate will form a waveguide layer facilitating the light propagation in the horizontal plane perpendicular to the surface. This part of light will be partially emitted out from a packaged LED, which will deteriorate the overall device polarization ratio. To solve this problem [1], a mesa etching and metal reflector coating can be applied during the LED processing to polarized SMNG LED structures as shown in Figure 7-2. For example, after the fabrication of the above-mentioned SMNG LED structure, the wafer can be patterned and plasma etched using plasma etching to remove the GaN layers down to the sapphire substrate to isolate the chip. The trench should have an area larger than the LED mesa and surrounding it. The width of the trench can be about 20um, which can be used later as the guiding line for chip dicing. The wafer is next coated with a dielectric layer e.g. 100nm SiO_2 using PECVD to act as an electrical isolation layer. A metal layer such as Al with a thickness of 200nm can be further deposited by e-beam evaporation and lift-off process to cover the trench and side wall of the InGaN/GaN layers on top of the sapphire substrate to block the light propagating along the InGaN/GaN waveguide layer. The metal layer can also cover any other part on the p-GaN surface, such as the p-mesa edge as shown in the Figure 7-2 (top view), to eliminate any potential light leakage through the mesa edge. This method will greatly improve the polarization ratio in a packaged LED.

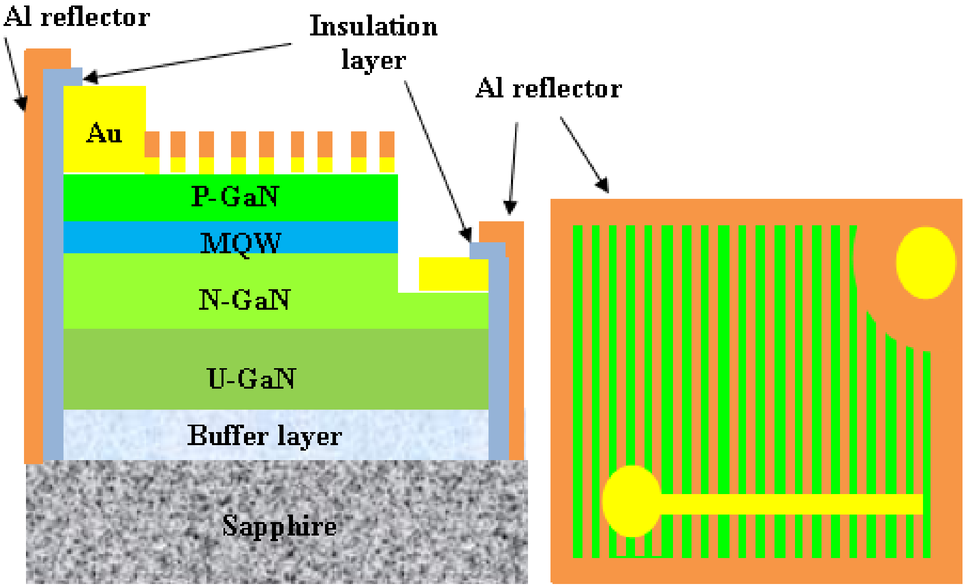

Figure 7-2 Cross section view (left) and top view (right) of the polarized SMNG LED having dicing trench etched and coated with reflecting metals.

In high brightness LEDs with high current injection and under high power operation, the LED can operate with p-side mounted down in contact with the heat sink with the light emission coming through the sapphire substrate. This mounting is carried out with flip-chip technology. The sapphire substrate can also be removed by, e.g., laser lift-off or photo-electro-chemical etching. The SMNG polarizer structure can be applied to both cases [1]. Figure 7-3 shows the schematic diagrams of the cross section view of the flip-chip LED with SMNG fabricated on the sapphire substrate and on the membrane LED with sapphire substrate removed and with SMNG formed on n-GaN layer.

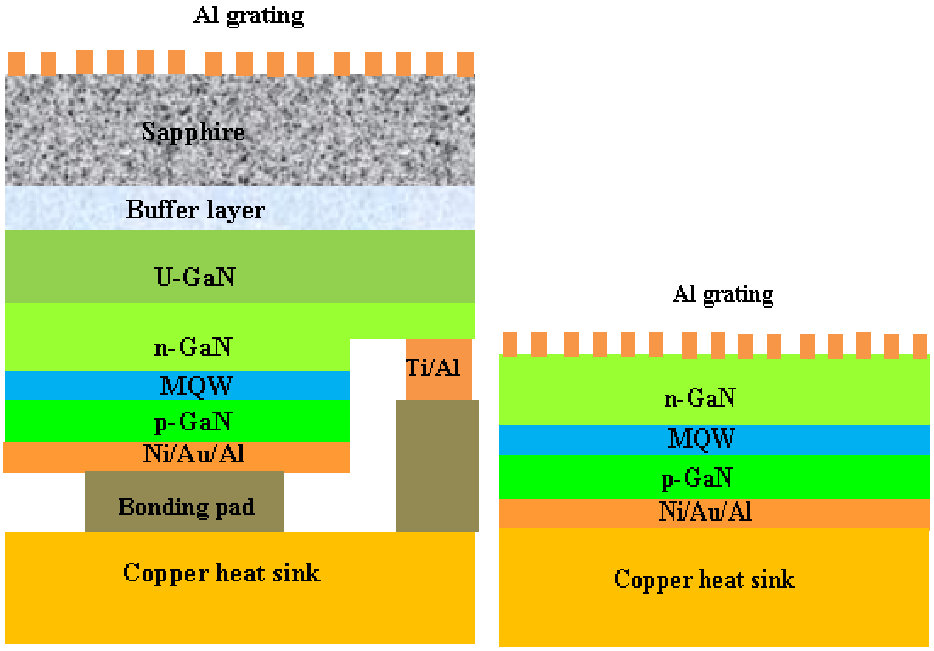

Figure 7-3 Cross section diagram of flip-chip LED with SWMG made on sapphire substrate (left) and a membrane LED with SMNG made on N-GaN (right)

We have carried out some preliminary experiments on fabricating the copper heat sink by electroplating. The seeding layer is Cr/Au 10nm/500nm. The current used for the electroplating process is 5A/dm^2 which gives a growth rate of 0.9um/min. After 2 hours of electroplating, we get a Cu layer with thickness of 100um is grown, as shown in the microscope image of Figure 7-4. The surface morphology of Cu after electroplating is further investigated using SEM, as shown in Figure 7-5, where the grain boundary of Cu can be seen clearly, suggesting a polycrystalline nature.

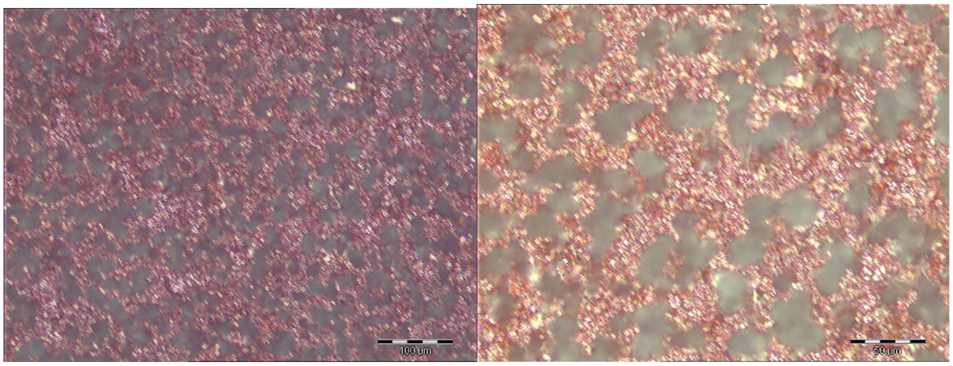

Figure 7-4 Microscope image surface of Cu after electroplating

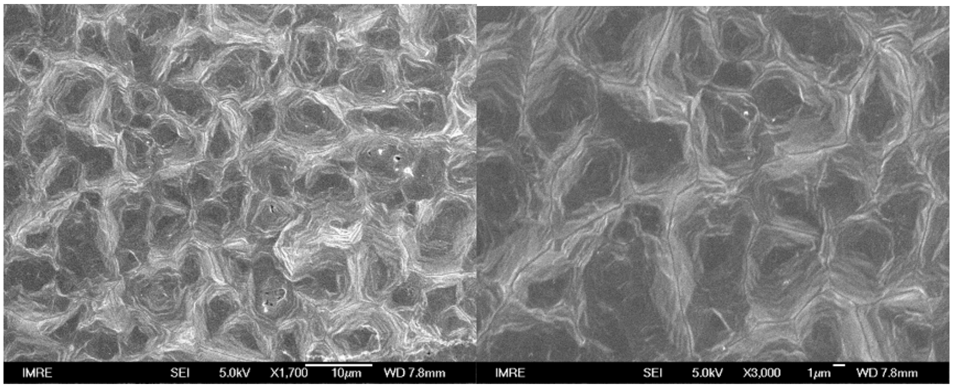

Figure 7-5 SEM image of surface morphology of Cu after electroplating, where the grain boundary of Cu is shown

The last design idea is to remove the substrate under the emission area, making the active region free-standing in the air. This will decrease the substrate absorption, and increase the refractive index contrast at the backside since the air gives the lowest refractive index of 1. The sample of GaN grown on Si (111) substrate was used to demonstrate this idea. The Si substrate below GaN was removed using isotropic Si etch, forming a microdisk structure pivoted by Si in the center, which is shown in Figure 7-6. Such an undercut microdisk LED will benefit from the strain release due to the removal of the Si substrate, and it also gives a brighter surface emission due to the larger refractive index contrast at the bottom surface. Figure 7-7 shows the PL measurement result. It shows that the undercut region gives much higher PL intensity compared with the non-undercut region. The non undercut region gives an intensity similar with that of the bare substrate, but with a different peak wavelength. This is due to the strain relaxation after the Si substrate removal. The emission peak from GaN around 360nm is too weak to observe because the MQW gives a much stronger light emission intensity.

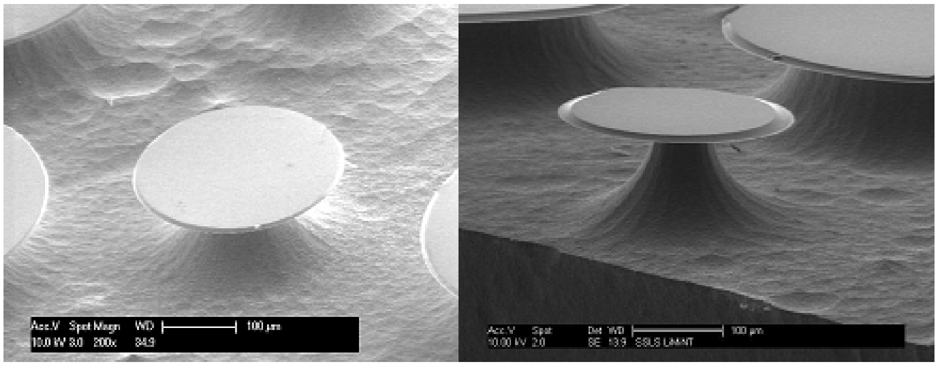

Figure 7-6 SEM image showing the undercut microdisk LED structure

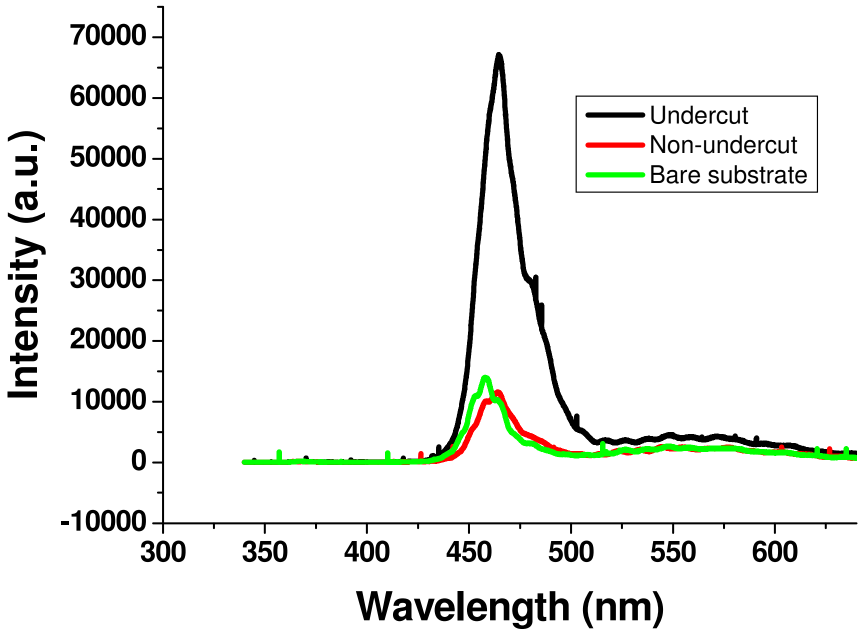

Figure 7-7 PL measurement of undercut GaN microdisk on Si substrate

The SMNG can be formed by ion milling, plasma etching or lift-off process. In the top surface emission LED structure, the dielectric insulation layer such as SiO_2 can be purposely etched to some extend, like 100nm. This will help the light extraction out of the GaN surface. Similarly, in the flip-chip LED or membrane LED structures, the Sapphire substrate or the n-GaN layer can be milled or etched to create surface subwavelength grating structure to enhance the light extraction from the LED chip. The principle of light emission enhancement is based on the EMT, as discussed in chapter 2.

In the above discussion, the active light emitting region of InGaN/GaN based quantum wells could have emission wavelength in the full visible range. It could also be InN based quantum dots or In-rich InGaN nano-crystals that give either colored emission or direct white light emission.

For polarized white light emission from a white LED, the phosphor or colloidal quantum dots materials can be coated directly on top of the InGaN/GaN blue or UV LED. In this configuration, the SMNG can be fabricated on top of the flat phosphor or quantum dots layers. The total polarized light emission efficiency could be enhanced by the extra phosphor or quantum dots layers due to their light recycling effect.

7.3 Summary

The work described in this thesis is summarized. Several improved LED structures with different designs to meet various application demands are proposed for future developments.

References

Chapter 1

[1] Nakamura S. and Fasol G. “The blue laser diode” (Springer, Berlin, 1997)

[2] Nakamura S., Senoh M., and Mukai T. “P-GaN/n-InGaN/n-GaN double-hetero -structure blue light-emitting diodes” *Jpn. J. Appl. Phys*. **32**, L8 (1993a)

[3] Nakamura S., Senoh M., and Mukai T. “High-power InGaN/GaN double-heterostructure violet light-emitting diodes” *Appl. Phys. Lett*. **62**, 2390 (1993b)

[4] Nakamura S., Iwasa N., and Senoh M. “Method of manufacturing p-type compound semiconductor” US patent 5,306,662 (1994a)

[5] Nakamura S., Mukai T. and Senoh M. “Candela-class high-brightness InGaN/AlGaN doubleheterostructure blue-light-emitting diodes” *Appl. Phys. Lett*. **64**, 1687 (1994b)

[6] Nakamura S., Senoh M., Iwasa N., Nagahama S. “High-brightness InGaN blue, green, and yellow light-emitting diodes with quantum well structures” *Jpn. J. Appl. Phys.* **34**, L797 (1995)

[7] Nakamura S., Senoh M., Nagahama S., Iwasa N., Yamada T., Matsushita

T., Sugimoto Y., and Kiyoku H. “Room-temperature continuous-wave operation of InGaN multi-quantum-well structure laser diodes” *Appl. Phys. Lett*. **69**, 4056 (1996)

[8] LIGHT-EMITTING DIODES by E. FRED SCHUBERT, 2003

[9] Optics, 3rd edition, Hecht, ISBN 0-201-30425-2]

[10] K. Horino, A. Kuramata, K. Domen, R. Soejima, and T. Tanahashi, Int. Symposium on Blue Laser and Light Emitting Diodes, pp. 530–533 (1996).

[11] K. Domen, K. Horino, A. Kuramata, and T. Tanahashi, 15th IEEE Int. Semiconductor Laser Conference Digest, pp. 149–150 (1996).

[12] K. Domen, K. Horino, A. Kuramata, and T. Tanahashi, IEEE J. Select. Top. Quantum Electron. 3, 450 (1997).

[13] S. L. Chuang and C. S. Chang, Phys. Rev. B 54, 2491 (1996).

[14] M. Suzuki and T. Uenoyama, Phys. Rev. B 52, 8132 (1995).

[15] T. Ohtoshi, A. Niwa, and T. Kuroda, J. Appl. Phys. 82, 1518 (1997).

[16] A. Niwa, T. Ohtoshi, and T. Kuroda, Appl. Phys. Lett. 70, 2159 (1997).

[17] B. Gil and A. Alemu, Phys. Rev. B 56, 12446 (1997).

[18] P. P. Paskov, T. Paskova, P. O. Holtz, and B. Monemar, Phys. Rev. B 70, 035210 (2004).

[19] P. Waltereit, O. Brandt, A. Trampert, H. T. Grahn, J. Menniger, M. Ramsteiner, M. Reiche, and K. H. Ploog, Nature (London) 406, 865 (2000).

[20] Y. J. Sun, O. Brandt, M. Ramsteiner, H. T. Grahn, and K. H. Ploog, Appl. Phys. Lett. 82, 3850 (2003).

[21] B. Rau, P. Waltereit, O. Brandt, M. Ramsteiner, K. H. Ploog, J. Puls, and F. Henneberger, Appl. Phys. Lett. 77, 3343 (2000).

[22] T. Koida, S. F. Chichibu, T. Sota, M. D. Craven, B. A. Haskell, J. S. Speck, S. P. DenBaars, and S. Nakamura, Appl. Phys. Lett. 84, 3768 (2004).

[23] A. Chitnis, C. Chen, V. Adivarahan, M. Shatalov, E. Kuokstis, V. Mandavilli, J. Yang, and M. A. Khan, Appl. Phys. Lett. 84, 3663 (2004).

[24] A. Chakraborty, B. A. Haskell, S. Keller, J. S. Speck, S. P. DenBaars, S. Nakamura, and U. K. Mishra, Appl. Phys. Lett. 85, 5143 (2004).

[25] A. Chakraborty, B. A. Haskell, S. Keller, J. S. Speck, S. P. DenBaars, S. Nakamura, and U. K. Mishra, Jpn. J. Appl. Phys. 44, L173 (2005).

[26] N. F. Gardner, J. C. Kim, J. J. Wierer, Y. C. Shen, and M. R. Krames, Appl. Phys. Lett. 86, 111101 (2005).

[27] H. Masui, A. Chakraborty, B. A. Haskell, U. K. Mishra, J. S. Speck, S. Nakamura, and S. P. DenBaars, Jpn. J. Appl. Phys. 44, L1329 (2005).

[28] R. Sharma, P. M. Pattison, H. Masui, R. M. Farrell, T. J. Baker, B. A. Haskell, F. Wu, S. P. DenBaars, J. S. Speck, and S. Nakamura, Appl. Phys. Lett. 87, 231110 (2005).

[29] H. Masui, T. J. Baker, M. Iza, H. Zhong, S. Nakamura, and S. P. DenBaars, J. Appl. Phys. 100, 113109 (2006).

[30] H. B. J. Jagt, H. J. Cornelissen, D. J. Broer, and C. W. M. Bastiaansen, “Linearly polarized light-emitting backlight,” J. Soc. Inf. Disp. **10**, 107-112 (2002)

[31] S. M. P. Blom, H. P. M. Huck, H. J. Cornelissen, and H. Greiner, “Towards a polarized light-emitting backlight: micro-structured anisotropic layers,” J. Soc. Inf. Disp. **10**, 209-213 (2002)

[32] Ko-Wei Chien and Han-Ping D. Shieh, "Design and Fabrication of an Integrated Polarized Light Guide for Liquid-Crystal-Display Illumination," Appl. Opt. **43**, 1830-1834 (2004)

[33] K.-W. Chien, H.-P. D. Shieh, and H. J. Cornelissen, “Polarized backlight based on selective total internal reflection at microgrooves,” Appl. Opt. **43**, 4672-4676 (2004)

[34] H. Masui, H. Yamada, K. Iso, J. S. Speck, S. Nakamura, and S. P. DenBaars, “Non-polar-oriented InGaN light-emitting diodes for liquid-crystal-display backlighting” J. Soc. Inf. Disp. 16, 571-578 (2008).

[35] R. Oldenbourg, “A new view on polarization microscopy,” Nature **381**, 811-812 (1996)

[36] S.-S. Lin, K. M. Yemelyanov, E. N. Pugh. Jr., and N. Engheta, “Separation and contrast enhancement of overlapping cast shadow components using polarization,” Opt. Express **14**, 7099-7108 (2006)

[37] J. B. Carruthers, “Wireless infrared communications,” in *Wiley Encyclopedia of Telecommunications*, J. G. Proakis, ed. (Wiley, 2002)

[38] J. Shakya, K. Knabe, K. H. kim, J. Li, J. Y. Lin, and H. X. Jiang, Appl. Phys. Lett. **86**, 091107 (2005).

[39] Schubert, M. F., Chhajed, S. Kim, J. K., Schubert, E. F., and Cho, J., “Polarization of light emission by 460nm GaInN/GaN light-emitting diodes grown on (0001) oriented sapphire substrates,” *Appl. Phys. Lett.* **91**, 051117 (2007).

[40] Martin F. Schubert, Sameer Chhajed, Jong K. Kim, E. Fred Schubert, and Jahee Cho, "Linearly polarized emission from GaInN lightemitting diodes with polarization-enhancing reflector," Opt. Express **15**, 11213-11218 (2007)

[41] Martin F. Schubert, Ahmed Noemaun, Sameer Chhajed, Jong Kyu Kim, E. Fred Schubert, and Cheolsoo Sone, "Encapsulation shape with non-rotational symmetry designed for extraction of polarized light from unpolarized sources," Opt. Express **15**, 10452-10457 (2007)

Chapter 2

[1] L. K. H. van Beek, “Dielectric Behavior of Heterogeneous Systems,” in Progress in Dielectrics, edited by J.B. Birks (CDC Press, Cleveland, 1967), Vol. **7**, pp.69-114.

[2] S. M. Rytov, “Electromagnetic properties of a finely stratified medium,” Soviet Physics JETP **2** (3), 466-475 (1956).

[3] P. Yeh, “A new optical model for wire grid polarizers,” Opt. Commun. **26** (3), 289-292 (1978).

[4] P. Yeh, “Generalized model for wire grid polarizers,” SPIE **307**, 13-21 (1981).

[5] E. D. Palik, “Handbook of optical constants of solids,” (Academic Press, San Diego, 1998).

[6] H. Hertz, Electric waves; being researches on the propagation of electric action with finite velocity through space.(Dover Publications, New York, 1962).

[7] W. K . Pursley, “The Transmission of Electromagnetic Waves Through Wire Diffraction Gratings,” Ph.D., University of Michigan, 1956

[8] G. R. Bird and M. Jr. Parrish, “The wire grid as a near-infrared polarizer,” J. Opt. Soc. Am .**50** (9), 886-891 (1964)

[9] M. Xu, H. Urbach, D. de Boer, and H. Cornelissen, "Wire-grid diffraction gratings used as polarizing beam splitter for visible light and applied in liquid crystal on silicon," Opt. Express **13**, 2303-2320 (2005)

[10] M. G. Moharam and T. K. Gaylord, “Rigorous coupled-wave analysis of planar-grating diffraction,” J. Opt. Soc. Am. **71** (7), 811-818 (1981).

[11] M. G. Moharam and T. K. Gaylord, “Rigorous coupled-wave analysis of grating diffraction—E-mode polarization and losses,” J. Opt. Soc. Am. **73** (4), 451-455 (1983).

[12] M. G. Moharam and T. K. Gaylord, “Diffraction analysis of dielectric surface-relief gratings,” J. Opt. Soc. Am. **72** (10), 1385-1392 (1982).

[13] M. G. Moharam and T. K. Gaylord, “Rigorous coupled-wave analysis of metallic surface-relief gratings,” J. Opt. Soc. Am. A **3** (11), 1780-1787 (1986)

[14] N. Chateau and J. P Hugonin, “Algorithm for the rigorous coupled-wave analysis of grating diffraction,” J. Opt. Soc. Am. A **11** (4). 1321-1331 (1994)

[15] M. G. Moharam, D. A. Pmmet, E. B. Grann *et al.*, “Stable implementation of the rigorous coupled-wave analysis for surface-relief gratings – enhanced transmittance matrix approach,” J. Opt. Soc. Am A **12** (5), 1077-1086 (1995).

[16] M.G. Moharam, E. B. Grann, D. A. Pommet *et al.,* “Formulation for stable and efficient implementation of rigorous coupled-wave analysis of binary gratings” J. Opt. Soc. Am .A **12** (5), 1068-1076 (1995).

[17] S. Peng and G. M .Morris, “An efficient implementation of rigorous coupled-wave analysis for surface-relief gratings,” J. Opt. Soc. Am A **12** (5), 1087-1096(1995).

[18] P. Lalanne and G. M. Morris, “Highly improved convergence of the coupled-wave method for TM polarization,” J. Opt. Soc. Am. A **13** (4), 779-784 (1996).

[19] G. Granet and B. Guizal, “Efficient implementation of the coupled-wave method for metallic lamellar gratings in TM polarization,” J. Opt. Soc. Am. A **13**, 1019-1023 (1996)

[20] www.**rsoft**design.com

[21] A. Tavlove, Computational Electrodynamics: The Finite-Difference Time-Domain Method, (Artech House, Norwood, MA, 1995)

[22] K. Yee, “Numerical solution of initial boundary value problems involving Maxwell's equations in isotropic media,” IEEE Trans. Antennas and Propag. **14,** 302–307 (1966).

[23] http://www.lumerical.com

Chapter 3

[1] M. A. McCord and M. J. Rooks, *Handbook of microlithography, micromachining, and microfabrication: volume 1*, edited by P. Rai-Choudhury, SPIE Optical Engineering Press, Bellingham, 1997

[2] K. Harafuji, A. Misaka, K. Kawak ita, N. Nomura, H. Hamaguchi and M. Kawamoto, “Proximity effect correction data processing system for electron beam lithography”, *J. Vac. Sci. Technol. B* **10**, 133 (1992)

[3] J. Jacob, S. Lee, J. McMillan and N. MacDonald, “Fast proximity effect correction: An extension of PYRAMID for circuit patterns of arbitrary size”, *J. Vac. Sci. Technol. B* **10**, 3077 (1992)

[4] G. Owen and P. Rissman, “Proximity effect correction for electron beam lithography by equalization of background dose”, *J. Appl. Phys.* **54**, 3573 (1983)

[5] M. G. Rosenfield, M. G. R. Thomson, P. J. Coane, K. T. Kwietniak, J. Keller, D. P. Klaus, R. P. Volant, C. R. Blair, K. S. Tremaine, T. H. Newman and F. J. Hohn, “Electron-beam lithography for advanced device prototyping: Process tool metrology”, *J. Vac. Sci. Technol. B* **11**, 2615 (1993)

[6] S. A. Rishton, H. Schmid, D. P. Kern, H. E. Luhn, T. H. P. Chang, G. A. Sai-Halasz, M. R. Wordeman, E. Ganin and M. Polcari, “Lithography for ultrashort channel silicon field effect transistor circuits”, *J. Vac. Sci. Technol. B* **6**, 140 (1988)

[7] S. Y. Chou, P. R. Krauss and P. J. Renstrom, “Nanoimprint lithography”, *J. Vac. Sci. Technol. B* **14**, 4129 (1996)

[8] M. Colburn, S. Johnson, S. Damle, T. Bailey, B. Choi, M. Wedlake, T. Michaelson, S. V. Sreenivasan, J. Ekerdt, and C. G. Willson, " Step and flash imprint lithography for sub-100nm patterning", *Proc. SPIE* **3676**, 379 (1999)

[9] M. Li, L. Chen and S. Y. Chou, "Direct three-dimensional patterning using nanoimprint lithography", *Appl. Phys. Lett.* **78**, 3322 (2001)

[10] M. D. Austin and S. Y. Chou, "Fabrication of 70 nm channel length polymer organic thin-film transistors using nanoimprint lithography", *Appl. Phys. Lett.* **81**, 4431 (2002)

[11] W. Zhang and S. Y. Chou, "Fabrication of 60-nm transistors on 4-in. wafer using nanoimprint at all lithography levels", *Appl. Phys. Lett.* **83**, 1632 (2003)

[12] Z. N. Yu, S. J. Schablitsky, and S. Y. Chou, "Nanoscale GaAs metal–semiconductor–metal photodetectors fabricated using nanoimprint lithography", *Appl. Phys. Lett.* **74**, 2381 (1999)

[13] Z. N. Yu, P. Deshpande, W. Wu, J. Wang, and S. Y. Chou, "Reflective polarizer based on a stacked double- layer subwavelength metal grating structure fabricated using nanoimprint lithography", *Appl. Phys. Lett.* **77**, 927 (2000)

[14] M. T. Li, H. Tan, L. Chen, J. Wang, and S. Y. Chou, “Large area direct nanoimprinting of SiO2–TiO2 gel gratings for optical applications”, *J. Vac. Sci. Technol. B* **21**, 660 (2003)

[15] M. Keil, M. Beck, T. G. I. Lin g, M. Graczyk, L. Montelius and B. Heidari, “Development and characterization of silane antisticking layers on nickel-based stamps designed for nanoimprint lithography” *J. Vac. Sci Technol. B* **23**, 575 (2005)

[16] http://www.ionbeammilling.com/ABOUT_THE_ION_MILLING_PROCESS

[17] R. J. Shul and S.J. Pearton (editors), *Handbook of advanced plasma processing techniques*, Springer, New York, 2000

[18] M. R. Steph en, J. C. Jerome and D. W. William (editors), *Handbook of Plasma Processing Technology: fundamentals, etching, deposition and surface interactions*, Noyes Publications, N. J., 1990

[19] G. Franz, C. Hoyler, an d J. Kaindl, “Reactive ion etching GaAs and AlAs: Kinetics and process monitoring”, *J. Vac. Sci. Technol. B* **14**,126 (1996)

[20] R. E. Lee, *Scanning electron microscopy and x- ray microanalysis*, P T R Prentice Hall, N. J. 1993

[21] Digital Instruments, “Scanning probe microscopy training notebook: version 3.0”, 2000

Chapter 4

[1] E.D. Palik, *Handbook of Optical Constants of Solids* (Academic, San Diego, CA, 1985)

[2] R. P. MADDEN and L. R. CANFIELD, "Apparatus for the Measurement of Vacuum Ultraviolet Optical Properties of Freshly Evaporated Films before Exposure to Air," J. Opt. Soc. Am. **51**, 838-845 (1961)

Chapter 5

[1] L. Zhang, J. H. Teng, S. J. Chua and E. A. Fitzgerald “Linearly polarized light emission from InGaN light emitting diode with subwavelength metallic nano-grating”, Appl. Phys. Lett. 95, 261110, 2009

[2] L. Zhang, J. H. Teng, S. J. Chua and E. A. Fitzgerald "Design and fabrication of subwavelength nanogratings based light-emitting diodes" Applied Physics A. vol 103, no.3, 827-830, 2011

Chapter 6

[1] P. H. Siegel, “Terahertz technology,” IEEE Trans. Microwave Theory and Tech. **50**, 910 (2002).

[2] R. Köhler, et.al, “Terahertz semiconductor-heterostructure laser,” Nature **417**, 156-159 (2002).

[3] Microtech (http://www.mtinstruments.com/thzpolarizers/index.htm)

[4] A. E. Costley, et.al, J. Opt. Soc. Am. **67**, 979 (1977).

[5] Itsunari Yamada et. al “Terahertz wire-grid polarizer with micrometer-pitch Al gratings” Optics Letters **34** 274 (2009)

[6] M. A. Ordal et. al., "Optical properties of the metals Al, Co, Cu, Au, Fe, Pb, Ni, Pd, Pt, Ag, Ti, and W in the infrared and far infrared," Appl. Opt. **22**, 1099-1119 (1983)

[7] Takeshi Nagashima and Masanori Hangyo, “Measurement of complex optical constants of a highly doped Si wafer using terahertz ellipsometry” Applied Physics Letters **79** 3917 (2001)

Chapter 7

[1] US patent: Light Emitting Diode with Polarized Light Emission (under filling)

Bibliography

07/2006 ~ 06/2010 : PhD candidate in "Advanced Materials in Micro- & Nano-Systems" Program, Singapore-MIT Alliance.

09/2003 ~ 06/2006 : M. Sc. In physics, Wuhan University, China

09/1999 ~ 06/2003 : B. Sc. In physics, Wuhan University, China

Appendices

Publication List

Journal Publications

1. **L. Zhang**, J. H. Teng, S. J. Chua and E. A. Fitzgerald "Linearly polarized light emission from InGaN light emitting diode with subwavelength metallic nano-grating", ***Appl. Phys. Lett***. 95, 261110, 2009

2. **L. Zhang**, M. Q. Xin, J. H. Teng, and S. J. Chua, "Photonic band structure of nanoporous anodized aluminum oxide with radius-to-period ratio modulation," ***Comput. Mater. Sci***., vol. 49, no. 1, S153-S156, July 2010.

3. **L. Zhang**, J. H. Teng, S. J. Chua and E. A. Fitzgerald "Design and fabrication of subwavelength nanogratings based light-emitting diodes" ***Applied Physics A***. vol 103, no.3, 827-830, 2011

4. M. Xin, **L. Zhang**, C. E. Png, J. H. Teng and A. J. Danner, "Asymmetric open cavities for beam steering and switching from line-defect photonic crystals," ***J. Opt. Soc. Am. B.*** **27**, 1153-1157 (2010)

Patent

1.US patent: Light Emitting Diode with Polarized Light Emission

Inventors: 1. Teng Jinghua 2. Chua Soo Jin **3. Zhang Liang** 4. Deng Liyuan

ETPL Ref: IMR/Z/06310

IMRE Ref: 201021

Conference Publications

1. **L. Zhang**, Teng J.H., Ang N., Chew A.B. and Chua, S.J. "Fabrication of Tunable Duty Cycle Metal Wire Nanograting by Oblique Sputtering" ***IEEE PhotonicsGlobal@Singapore*****,** IPGC 2008 pp.1-4

2. **L. Zhang**, J. H. Teng, H. Tanoto, S. Y. Yew, L. Y. Deng and S. J. Chua "Terahertz wire-grid polarizer by nanoimprinting lithography on high resistivity silicon substrate" ***IRMMW-THz,*** Sept. 2010***,*** pp.1-2

Conferences presentations and Awards

1. **L. Zhang,** J. H. Teng, S. J. Chua and E. A. Fitzgerald "Linearly polarized InGaN LED by subwavelength metallic nanograting," **META'10** (2nd International Conference on Metamaterials, Photonic Crystals and Plasmonics)**,** Cairo, Egypt, Feb. 22 - 25, 2010. **(Oral Presentation)**
2. **L. Zhang,** J. H. Teng, S. J. Chua and E. A. Fitzgerald "Sub-50nm Ultra-thin-wall Honeycomb Photonic Crystal ----- towards next generation III-V/Si integration" **ICMAT 2009**, Singapore, June 28 –July 3, 2009. **(Oral Presentation)**

3. **L. Zhang,** K. H. Dai, J. H. Teng, S. J. Chua **"**Photonic Band Structure of Anodized Aluminum Oxide with Tunable Hole Size**" ICMAT 2009** Symposium Q Computational Materials Design at All Scales: From Theory to Application， Singapore, June 28 –July 3, 2009. **(Poster Presentation)**

4. **L. Zhang,** J. H. Teng, and S. J. Chua "Polarized Light Emission from InGaN LEDs,"**4th MRS-S** Conference on Advanced Materials, 17 – 19 March, 2010**, (Poster Presentation)**

5. **L. Zhang,** J. H. Teng, S. J. Chua and E. A. Fitzgerald "Linearly polarized InGaN LED by subwavelength metallic nanograting," **SMA Symposium 2010,** AMM&NS technical session, 19 January 2010 **(Oral Presentation)**

6. **IEEE Distinguished Student Talk 2010** “Polarized light emission from InGaN LED with subwavelength metallic nanograting,” presented at March 11, 2010 **(Oral Presentation)**

7. **L. Zhang,** J. H. Teng, S. J. Chua and E. A. Fitzgerald “Linearly polarized light emission from InGaN LED with subwavelength metallic nanograting,” January 22, 2010**. 1st place** of IEEE photonics **Best Student Paper Awards**

8. K.H. Dai, C.B. Tay, **L. Zhang**, C.B. Soh, S. J. Chua, L. S. Wang, D.X.Huang, “Enhanced Light Extraction from GaN-based Light Emitting Diodes” with ZnO Nanorods on NiO/ITO Contact,” ” **ICMAT 2009**, Singapore, June 28 –July 3 **Best Poster Awards**